HAL open science

Multi-transition solar cells with localised states

Pierre Rale

To cite this version:

Pierre Rale. Multi-transition solar cells with localised states. Physics [physics]. Université Pierre et Marie Curie - Paris VI, 2015. English. NNT : 2015PA066541 . tel-01322448

HAL Id: tel-01322448

https://theses.hal.science/tel-01322448v1

Submitted on 6 Jul 2017

HAL is a multi-disciplinary open access archive for the deposit and dissemination of scientific research documents, whether they are published or not. The documents may come from teaching and research institutions in France or abroad, or from public or private research centers.

L'archive ouverte pluridisciplinaire **HAL**, est destinée au dépôt et à la diffusion de documents scientifiques de niveau recherche, publiés ou non, émanant des établissements d'enseignement et de recherche français ou étrangers, des laboratoires publics ou privés.

École Doctorale Physique et Chimie des Matériaux

Thèse de doctorat

Discipline : physique des matériaux

Présentée par Pierre Rale

Multi-transition solar cells with localised states

Mme Hélène Carrère	INSA Toulouse	Rapporteur
M. Ludovic Escoubas	IM2NP	Rapporteur
M. Abhay Shukla	UPMC	Examinateur
M. Olivier Durand	INSA Rennes	Examinateur
M. Yoshitaka Okada	Université de Tokyo	Examinateur
M. Jean-François Guillemoles	CNRS	Directeur de thèse
M. Laurent Lombez	CNRS	Encadrant

Acknowledgement

Je tiens à remercier Jean-François Guillemoles en premier lieu pour avoir élaboré et dirigé ma thèse. Sa grande culture scientifique et sa clairvoyance auront été d'une grande aide pour avancer pendant ces trois années. Je le remercie pour les opportunités qu'il m'a offertes d'aller dans des conférences nationales et internationales présenter mon travail, mais également pour m'avoir permis d'aller passer 3 semaines au sein du laboratoire Rcast au Japon qui auront été pleines d'enseignements pour ma fin de thèse. Vient ensuite bien évidemment Laurent Lombez, mon encadrant de thèse, qui a suivi au quotidien mon évolution. Il a joué un rôle déterminant dans le déroulement de ma thèse, notamment en me permettant d'élargir mon champ d'étude aux cellules à bandes intermédiaires au moment où mon sujet initial était à l'arrêt. Il a été mon référent scientifique et un soutien quotidien primordial. Son humour, son dévouement et sa compétence en font un encadrant exceptionnel. Les « bobbys » qui me succèderont auront beaucoup de chance de travailler avec lui. Je tiens également à remercier Daniel Lincot qui m'a accueilli dans son laboratoire. Son enthousiasme sans faille donne espoir même aux plus pessimistes quant à l'avènement, un jour, du bon sens et de l'utilisation massive des énergies renouvelables. Discuter avec lui a toujours été un plaisir, rare, mais véritable. Merci également à Yves Schlumberger, directeur adjoint du laboratoire, et à son successeur Matthieu Versavel, qui représentent l'autorité EDF au sein du laboratoire.

Je remercie également tous les membres de l'ANR Menhirs avec qui j'ai étroitement collaboré pendant ces trois années. En commençant par Olivier Durand, coordinateur de l'ANR Menhirs, qui par son enthousiasme et sa compétence scientifique a été un élément clef dans la bonne conduite du projet. Un grand merci à Eric Tea, Mister Tea pour les intimes et être hybride FOTON/IRDEP, pour sa sagesse ancestrale et tous les bons moments passés

ensemble. Merci à Samy Almosni, mon alter ego au sein du laboratoire FOTON, avec qui la collaboration aura été très bonne tout au long de ces trois années. Merci également à Charles Cornet, Laurent Pedesseau et toute l'équipe du laboratoire FOTON grâce à qui j'ai pu avoir des échantillons à l'état de l'art et des discussions très enrichissantes. Les laboratoires INL et CEMES ont également activement participé à ce projet et je remercie toutes les personnes impliquées pour leur travail au sein du projet.

Merci au laboratoire RCAST au Japon pour les trois semaines passées chez eux. Merci à son directeur, Professeur Okada, pour m'avoir accueilli, merci à Ahsan-San et Tamaki-San pour m'avoir consacré du temps et m'avoir beaucoup aidé pendant ces trois semaines.

Venons-en maintenant à l'Irdep. Evoluer au sein de l'Irdep pendant trois ans a été un vrai plaisir, une chance et m'a donné l'opportunité de rencontrer des gens exceptionnels. Je commencerai par remercier Tarik Sidali, sans qui je n'aurais sans doute pas fait cette thèse, ni même passé autant de bon temps avec une clope et un café. Son aide précieuse lors des recuits de GaAsPN a également été déterminante. Dans la filière recuit, merci à Grégory Savidan et à Aurélien Duchatelet qui m'ont également aidé avec ces fours parfois capricieux. Un grand merci à Benoît Behaghel - je l'ai mis dans l'Irdep même si je suis le seul à savoir qu'il y est affilié… - mon binôme sur les échantillons à boîte quantiques. Toutes les heures de discussions passées à s'écharper sur… tout et n'importe quoi n'auront pas servi à rien ! Je suis sûr que ces passes d'armes continueront au LPN et je m'en réjouis d'avance ! Merci aussi pour toutes les heures passées à préparer les échantillons ! Et pour notre prochaine destination faudra que tu trouves un endroit sympathique hein ! Merci à toute l'équipe caractérisation. Un grand merci à Jean Rodière, mon PhD buddy, avec qui j'ai passé des moments mémorables. Et il n'y a pas que les pavés de Strasbourg qui s'en souviendront ! Merci à François Gibelli, l'homme d'état rebelle, pour son exigence intellectuelle, sa gentillesse et toutes les discussions, scientifiques ou non, que nous avons pu avoir. Merci Myriam pour ta bonne humeur, tes idées/conseils toujours intéressants, les répètes de présentations

à l'arrache et pour toute l'aide que tu as pu m'apporter. Merci à Gilbert HAAAGGEE, l'homme qui parlait 15 langues et poussait de la fonte… mais pas que ! Merci à Daniel Ory pour ses blagues légères. Sans oublier évidemment Amaury (ou momo, paraîtrait que c'est son nouveau prénom) Delamarre, qui m'a accueilli à l'Irdep, au Japon et qui a développé le HI. Sans toi une bonne partie des résultats de ma thèse n'auraient pas existé !

Merci à Fred qui m'a toujours été d'un grand soutien. En fière représentante franco-italienne, elle comprend l'importance d'une bonne plainte, ce qui en a fait une interlocutrice privilégiée pour moi. Mais c'est surtout sa bonne humeur et son humour qui en font une collègue et amie précieuse. Merci à Johnny Clatal pour son humour constant. Il est également un grand puit de sciences à ses heures perdues. Merci à Amélie, « la grosse », pour m'avoir supporté pendant la rédaction. Merci à Marie Jubault pour ses connaissances. Merci à Sebastien Juttal pour m'avoir laissé gagner pendant presque trois au Jokari. T'es vraiment mauvais Jack ! Merci à Serena Gallanti pour avoir failli me tuer à deux reprises en Azerbaïdjan. Merci à Nicolas Loones pour son cuissard et ses conseils sportifs de premier ordre. Merci à Nathanaëlle pour m'avoir fait découvrir le karaoké japonais et pour ses conseils toujours avisés. Merci à Sebastien Delbos, mon « tuteur », pour sa présence et ses conseils bien sentis. Ses qualités de tuteur les plus remarquables sont néanmoins plus liées à sa personnalité, merci pour ta bonne humeur et ton esprit. Merci à Hugo Levard pour m'avoir fait découvrir la face cachée des catas. Merci à Julien Vidal pour son cynisme toujours plus cinglant, acide et drôle. Et pour ses guides des lieux de perdition. Merci Torben pour tes adresses de currywurst parisiennes et Jorge pour ses empanadas maison. Merci à tous les doctorants contemporain à ma thèse pour leur solidarité. Merci aux koalas qui, même s'ils sont drus, sont très mignons.

Un grand merci à Claire Vialette, véritable patronne de l'ombre du laboratoire et toujours disposée à aider les pauvres thésards perdus, et à Mireille Owona qui par son sourire et ses commérages pimentent la vie du laboratoire. Et merci à tout le laboratoire pour ces bons moments passés ensemble.

Merci évidemment à toute ma famille pour leur soutien, je n'ai pas été très facile pendant cette période mais paraît que ça s'arrange après… Merci à ma mère et ma sœur Marie pour l'organisation du buffet. Et à mon autre sœur, Elise, pour m'avoir proposé de relire ma thèse.

Enfin, last but not least, je remercie la personne morale du bâtiment F pour son ambiance légère mondialement reconnue, sa distinction sans égal et tous les bons moments passés en son sein. Et une petite pensée pour toutes ces mouches…

Introduction

Introduction 11
1 Multi-transition solar cells 15
1.1 Semiconductor luminescence 15
1.2 Current-voltage characteristic and Shockley-Queisser limit 18
1.3 Third generation systems 22
1.3.1 Multijunction solar cells 23
1.3.2 Intermediate band solar cells 27
2 Experimental setups and methods 35
2.1 Classical solar cell characterisations 36
2.1.1 Quantum efficiency measurements 36
2.1.2 J-V characteristics 37
2.2 Spectrophotometry 40
2.3 Photoluminescence 42
2.3.1 Confocal microscope 42
2.3.2 Hyperspectral Imager 47
3 Dilute nitride for multi-transitions photovoltaic systems 51
3.1 Dilute nitride alloys 52
3.1.1 Dilute nitride III-V alloy for multi-junction solar cells 52
3.1.2 Band anti-crossing theory of GaAsPN 54
3.1.3 Samples description 56
3.2 Numerical simulations 59

3.2.1 GaAsPN parameters 60
3.2.2 Ideal case 60
3.2.3 The μτ product and thickness 61
3.2.4 Electron affinity 63
3.2.5 Doping 64
3.3 Optoelectrical characterisation of the GaAsPN top cell 69
3.3.1 Electrical characterisations 69
3.3.2 Optical characterisations 75
3.4 Discussions 85
3.4.1 Spatial heterogeneity 86
3.4.2 Low collection efficiency 87
3.4.3 Annealing effect 92
3.4.4 Luminescence properties and statistical study 93
3.4.5 Open-circuit voltage 96
3.4.6 Analyse of the best cell 97
3.4.7 Conclusion 99
3.5 GaAsPN for intermediate band solar cells 99
3.6 Conclusion 104
4 Quantum confined heterostructures for multi-transitions photovoltaic systems 105
4.1 Experimental evidence of IB effect 106
4.1.1 Current –voltage measurements 106
4.1.2 Two photon subband gap photocurrent 107
4.1.3 Luminescence based characterisations 108
4.2 Developed Photoluminescence-based method 110

4.2.1 Two-photons absorption (TS-TPA) with PL 110

4.2.2 Absolute calibration, Δ μ determination and voltage preservation 111

4.3 Quantum wells-based heterostructures 111

4.3.1 Sample description 111

4.3.2 PL measurements 113

4.3.3 Two-steps two-photons absorption 113

4.3.4 Hyperspectral measurements 116

4.3.5 Discussion 117

4.3.6 Conclusions 117

4.4 Quantum dots based heterostructures 118

4.4.1 Sample description 118

4.4.2 Optical management structure 120

4.4.3 Particularities of QD-based IBSC 124

4.4.4 PL measurements 129

4.4.5 Two-steps two-photon absorption 132

4.4.6 Hyperspectral measurements 136

4.5 Conclusions 140

Conclusion 141

Bibliography 144

Introduction

Solar energy is a formidable hope for society to reach unlimited, low-cost and renewable energy sources. Every day this is more than 1 times the world energy consumption that hits the earth surface. Converting it with high efficiency and reasonable cost is a crucial challenge for the human society. Solar photovoltaics (PV) growth is spectacular (see Figure 1.3.1-2) with a cumulative capacity increasing about 47% per year since 2001, but accounts only for approximately 0.85% of global electricity production in 2013 and approximately 139 gigawatts of installed peak capacity [1]. It is the most widely deployed solar electric technology in the world today and its cost is constantly falling (cf. Figure 1.3.1-1) resulting in an installation acceleration always underestimated over the years. In France, which is not the most sunny country in the world, scenario of 100% renewable energy consumption, including a large contribution of PV, has been presented [2]. Indeed, PV electricity has reached 105€/MWh [3] and is now cheaper than nuclear electricity (109€/MWh for EPR in London [4]). In sunnier countries, including USA, this cost goes down to 50€//MWh [5], [6].

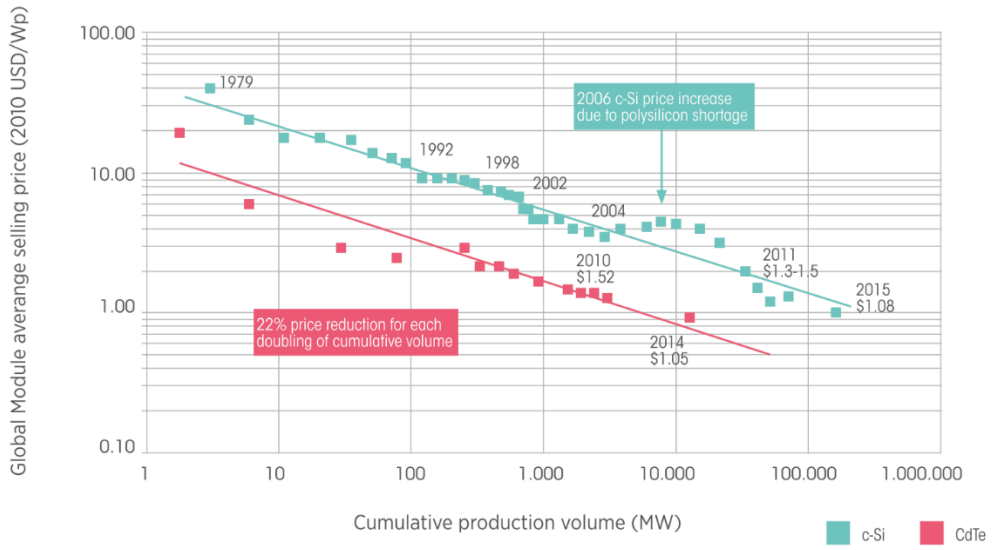

Figure 1.3.1-1: Global PV module learning curve for c-Si and CdTe modules from 1979 to 2015 [7].

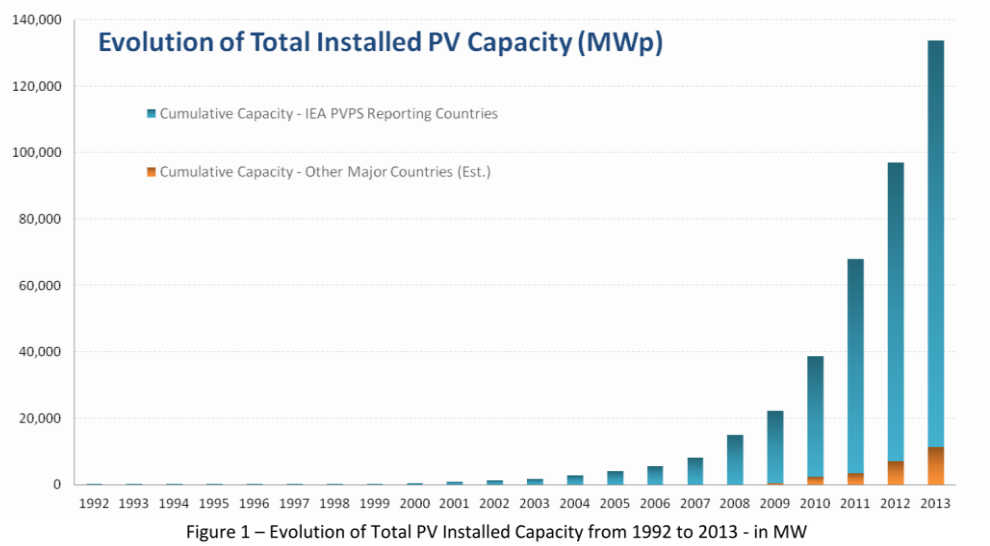

Figure 1.3.1-2: Evolution of the total installed PV capacity in the world (MWp) [8].

The PV systems efficiency are however still currently low, 25.6% for the Silicon based solar cell record and 22.9% for a module under AM1.5 spectrum [9]. A technology breakthrough is still needed and awaited to promote this energy source worldwide. R&D community is working in this sense with the emergence of new solar cell concepts, as for instance multi-junction solar cells that reaches nowadays 46% efficiency with a theoretical limit of 87% [10]. This technology still suffers from high fabrication costs and efforts are made to reduce them, for instance in substituting the expensive substrate used today with silicon ones. However difficulties remains to find suitable material to use in association with silicon subcell due to the lack of semiconductor lattice matched with it. Highly mismatched alloys (HMAs) have been investigated as a possibility to tune the lattice constant in the same time as the band gap energy by introducing strongly localised states in the energy gap. Such semiconductors are however hard to optimise for PV applications because their growth are thermodynamically metastable. This ability to introduce localised states exists also in quantum confined systems, such as quantum dots or quantum wells heterostructures. These structures can therefore also be used for band gap energy tuning purposes [11]–[13].

Since two decades and the introduction of intermediate band solar cells by Pr Luque and Marti, subband gap localised states are also explored for this alternative multi-transition solar cell concept. This new concept, partially introduced in [14], [15], exhibits a theoretical efficiency limit of 63% [16] in only one material, allowing cost benefices. Up to days, no clear experimental proofs of such device has been demonstrated yet, mostly because of the difficulty of characterising such a device.

The work in this thesis focuses on two localised states semiconductor systems.

In the first chapter, we study the fundamental limits of classical, multi-junction and intermediate band solar cells. To do so we first focus on the luminescence of solar cell that we will use to demonstrate the Shockley-Queisser limit in the detailed-balanced principle. Fundamental electrical properties of solar cells such as the open-circuit voltage or short-circuit current will also be apprehend via the solar cell luminescence. Then, the multi-transitions concepts, multi-junction and intermediate band solar cells, will be analysed through the detailed balance principle, exhibiting the mechanisms behind these concepts and their theoretical thermodynamic efficiency limits.

The second chapter will dedicated the experimental technics used during this thesis. The diversity of the sample studied, as well as their complexity made us use a wide range of characterisation methods. In addition to standard electrical (J-V characteristics, EQE) or optical (absorbance spectroscopy, reflectometry) measurements, we will detail several characterisation methods based on steady-state or time-resolved photoluminescence. A special attention will be given to the hyperspectral imager. This original tool gives access to spatial variation of the absolute value of chemical potential in the sample.

Later on, chapter 3 will be devoted to the study of GaAsPN. This nitrogen based HMA (highly mismatched alloy) will be first analysed in a tandem solar cell top cell perspective. After a presentation of the particular band structure of this alloy, we will present the results of numerical simulations performed with the softwares

SCAPS and Silvaco. Then, a wide optical and electrical study of a large set of absorbers and p-i-n junction is shown. Carrier dynamics and recombination mechanisms will be studied by photoluminescence measurement and correlations with electrical performances will be established. Finally, we will probe the IBSC potential of this alloy by dual-beam EQE measurements.

Eventually, chapter 4 will concern the quantum-confined based structure for IBSC. We will first discuss about the IBSCs' characterisation method. A specific photoluminescence based characterisation method is then presented subsequently, probing the two key IBSC mechanisms: the two-step two-photon absorption (TS-TPA) and the voltage preservation. This result is important and will be discussed widely. Perspectives of this work will be given.

Chapter 1

Multi-transition solar cells

In this chapter, we deal with the physics of multi-junction solar cells. We will first introduce the semiconductor luminescence and show that this quantity can be related to the open-circuit voltage of a solar cell. It will also be of interest in the second part, where the detailed balance principle for a single transition solar cell will be presented. This model, introduced by Shockley and Queisser in 1961, defines the thermodynamic limits of the standard solar cells [17]. Finally, the same model will be applied to the two multi-transition systems studied in this thesis. Considerations about the specific difficulties encountered with those systems will also be discussed.

1.1 Semiconductor luminescence

While being in thermodynamic equilibrium, any body at temperature T emits photons following the Kichorff's law. A semiconductor brought out of equilibrium, for instance with a light or an electrical bias, has an excess carriers concentration that results in spontaneous radiative recombination. This radiative recombination is the physical phenomenon at the origin of luminescence. It occur when an electron at an energy ε_2 recombines radiatively with a hole at energy ε_1. We note E the energy of the transition.

$$dr_{spont}(E) = |M^2| D_{12} \frac{c_0}{n} D_\gamma(E)(1 - f(\varepsilon_1))f(\varepsilon_2) \qquad (1.1\text{-}1.)$$

where $|M^2|$ is a matrix element that reflects the coupling between initial and final states. The f(ε) is a Fermi function that accounts for the carrier occupation of the considered states. D_{12} and D_γ are the combined density of electronic states between which transition occur and the density of states for photons in solid angle Ω respectively. The latter is expressed:

$$D_\gamma(E) = \frac{\Omega n^3 E^2}{4\pi^3 \hbar^3 c_0^3} \qquad (1.1\text{-}2.)$$

As the emissivity equals the absorptivity according to Kirchhoff's law (and verified even under illumination [18], [19]) the spontaneous radiation rate of such a transition is expressed as [20], [21]:

$$dr_{spont}(E) = \alpha_{12}(E) D_\gamma(E) \frac{c_0}{n} \frac{(1 - f(\varepsilon_1))f(\varepsilon_2)}{f(\varepsilon_1) - f(\varepsilon_2)} \qquad (1.1\text{-}3.)$$

with $\alpha_{12}(E)$ being the absorption coefficient between the two states, c_0 the light celerity, and n the medium refractive index. The two Fermi distributions, $f(\varepsilon_1)$ for the states at energy ε_1 with a quasi-Fermi energy E_{FV} and $f(\varepsilon_2)$ for the states at energy ε_2 with a Fermi energy E_{FC}, are:

$$f(\varepsilon_{1,2}) = \frac{1}{exp\left(\frac{\varepsilon_{1,2} - \varepsilon_{FV}}{kT}\right) + 1} \qquad (1.1\text{-}4)$$

If we replace $f(\varepsilon_{1,2})$ in Eq. (1.1-3.) and integrate over the density of states, we obtain the global radiative transition rate [22]:

$$r_{spont}(E) = \alpha(E) D_\gamma(E) \frac{c_0}{n} \left[\exp\left(\frac{E - \Delta\mu}{kT}\right) - 1\right]^{-1} \qquad (1.1\text{-}5.)$$

where α(E) is the absorption coefficient of the material, and Δμ the chemical potential of the radiation. This relation accounts for all the radiative transitions emitting a photon at the energy E regardless of the initial states of the electron-hole pair. This is a generalisation of the Planck's and Kirchhoff's laws taking into account two separate carrier populations. From this expression and by using the continuity equations, one can determine the expression of the experimentally measured quantity, i.e. the luminescence flux, $\Phi(E,r,\theta)$, at the material surface:

$$\Phi(E,r,\theta) = A(E,r,\theta)\frac{cos(\theta)}{4\pi^3\hbar^3c_0^2}E^2\left[\exp\left(\frac{E-\Delta\mu}{kT}\right)-1\right]^{-1} \qquad (1.1\text{-}6.)$$

Where the absorptivity A(E,r,θ) is the probability for a photon of energy E, located at the surface position r and viewed under an incident angle θ, to be absorbed. The cos (θ) accounts for the fact that the emission at the surface follows the Lambert's law [23], [24].

At high energies, i.e. E-Δμ > kT, we can approximate the Bose-Einstein distribution by a Maxwell-Boltzmann distribution:

$$\Phi(E) = K(\theta,E,r)A(E)\Phi_{bb}(E,T)\exp\left(\frac{\Delta\mu}{kT_c}\right) \qquad (1.1\text{-}7.)$$

where Φ_{bb} is the emission of a black body at temperature T_c, A(E,T) the absorption by the sample and K a calibration constant depending on the geometrical parameters of the measurement. As Δμ=qV [23], V being the voltage at the cell terminal, this relation permits to probe optically this key parameter. This relation has been widely discussed and verified for various types of absorber: Silicon [25], GaAs [26], [27], CIGS [28] and even for dye solar cells [29]. As this quantity is fundamental to study the multi-transition systems, this relation will be used widely in this thesis, in particular in Chapter 4.

In summary, the luminescence of solar cell is a fundamental mechanism, from which the electrical voltage of the cell can be measured. Besides, as the current in

the solar cell is related to the absorbed photon flux, the "optical" J-V characteristic can plotted with the sole knowledge of the luminescence and the incident flux [30]. The next section introduces the detailed balance theory leading to the Shockley-Queisser limit. Relations between the electrical properties and the luminescence will be explained.

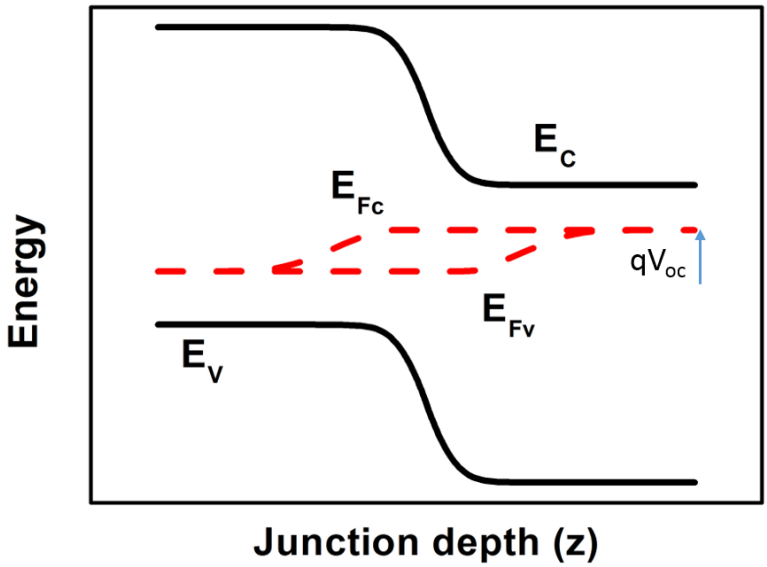

Figure 1.3.1-1: Band diagram of a pn junction under illumination at V_{oc}. E_c, E_v, E_{Fc} and E_{Fv} are the conduction band, the valence band, the quasi-Fermi levels for holes and electrons respectively.

1.2 Current-voltage characteristic and Shockley-Queisser limit

Solar cells have emerged thanks to the p-n junction. This technology has for long been the only one exhibiting photovoltaics results. Even if this technology is now well-handled, its efficiency limit is quite low. In 1961, Shockley and Queisser proposed a model to determine this technology efficiency limit [17]. This model takes into account the absorption and the radiative transitions for the electron-holes pairs. With this consideration, the current through the diode is equal to the difference between the absorption and the radiative recombination.

$$J(V) = q\left(\dot{N}_{abs} - \dot{N}_{em}(V)\right) \qquad (1.2\text{-}1.)$$

where J is the electric current density in mA.cm^{-2}, $\dot{N}_{em}(V)$ and $\dot{N}_{abs}$ the emitted and absorbed photon current density respectively.

For a semiconductor at temperature T_c under an applied voltage V, the emitted photon flux is defined as:

$$\dot{N}_{em}(V) = \frac{np}{n_i^2}\dot{N}_0 = exp\left(\frac{qV}{kT_c}\right)\dot{N}_0 \qquad (1.2\text{-}2.)$$

where n, p and n_i holds for the electrons, holes and intrinsic carrier densities respectively. The photon flux emitted at equilibrium, $\dot{N}_0$, is given by the Planck's law, for a black body at temperature T_c:

$$\dot{N}_0 = \frac{1}{4\pi^2\hbar^3c^2}\int_{E_G}^{\infty}\frac{E^2dE}{exp\left(\frac{E}{kT_c}\right)-1} \qquad (1.2\text{-}3.)$$

Concerning the absorbed photon flux, two sources irradiates the sample: the Sun and the thermal radiance of the ambient environment. According to the detailed balance, the ambient photon flux is equal to $\dot{N}_0$. As for the Sun, if we consider the sun emits a black body spectrum at the temperature T_s, the photon flux incident on the cell per unit area, unit solid angle and unit photon energy is expressed as:

$$dN_{ph} = \frac{E^2}{4\pi^3\hbar^3c^2}\left(\frac{1}{exp\left(\frac{E}{kT_s}\right)-1}\right)cos\theta sin\theta d\theta d\varphi dE \qquad (1.2\text{-}4.)$$

where E is the photon energy, k the Boltzmann's constant, T_s the Sun temperature, θ the incident angle and φ the azimuthal angle. Once integrated over angles and energy, and assuming an absorptivity of 1 over the band gap energy and zero below, the absorbed photon current density is given by Planck's Law:

$$\dot{N}_{abs,sun} = \frac{1}{4\pi^2\hbar^3c^2}\int_{E_G}^{\infty}\left(\frac{f}{exp\left(\frac{E}{kT_s}\right)-1}\right)E^2dE \qquad (1.2\text{-}5.)$$

where f is a geometrical factor that accounts for the solid angle subtending the Sun, given by $f = sin^2(\theta_s)$ for an incident light inside a cone of semi-angle θ_s.

Combining Eq (1.1-4), Eq. (1.1-5.) and Eq. (1.1-7.). we obtain:

$$J(V) = \dot{N}_{abs,sun} - \dot{N}_0\left(exp\left(\frac{qV}{kt_c}\right)-1\right) \qquad (1.2\text{-}6.)$$

This expression is the current-voltage characteristic for an ideal diode with

$J_{sc} = q\dot{N}_{abs,sun}$ and $J_0 = q\dot{N}_0$

Finally, the power conversion efficiency is expressed as

$$\eta = \frac{V\,J(V)}{\dot{N}_{sun}} \qquad (1.2\text{-}7.)$$

Radiative recombination is affecting both short-circuit current density and open-circuit voltage of the device. Neglecting it and assuming that all absorbed lead to a collected carriers pair, maximal efficiency reaches 44% for a blackbody spectrum at 6000K. Radiative recombinations are nonetheless unavoidable and even needed since the emissivity equals the absorptivity according to the detailed balance principle. For a cell at 300K, the efficiency limit given by the Shockley-Queisser model under AM1.5 is 31% for a band gap E_G=1.4eV, while under maximum concentration this limit reaches 41% for a 1.1eV band gap. It is important to note that $\dot{N}_0$ and $\dot{N}_{abs,sun}$ are two quantities depending on the band gap energy, so does the power conversion efficiency. Indeed, it appears that two important processes limit the conversion efficiency: (i) the non-absorption where no photon can be absorbed below the band gap and (ii) the thermalisation where photons with energy higher than the band gap will create electron-hole pairs that eventually will lose

their kinetic energy by heating the lattice. The ratio of the different mechanisms as a function of the bandgap is illustrated in Figure 1.3.1-1. And one can see that the maximum conversion efficiency is obtained for E_g around 1.4 eV.

There exists however different ways to convert sunlight into electrical work that may be more efficient. Several concepts have arisen in order to overcome this low efficiency, all gathered under the third generation solar cell's label. They aim at limiting the two main losses appearing in single junction cell.

In the case where non-radiative recombinations occur, this model still holds, completed with the radiative efficiency of the cell, defined as [31]:

$$u\,(E) = \frac{\dot{N}_{em} - \dot{N}_0}{\dot{N}_{abs}} = \frac{J_0\left(exp\left(\frac{qV_{oc}}{kT_c}\right) - 1\right)}{J_{sc}} \qquad (1.2\text{-}8.)$$

From this equation, we can expressed the open circuit voltage

$$V_{oc} = \frac{kT_c}{q} ln\left[\frac{u(E)\ J_{sc}}{J_0} + 1\right] \qquad (1.2\text{-}9.)$$

The above expression shows that the V_{oc} is linked to the material quality. This will be important in the third chapter of this thesis, where we will deal with a dilute nitride alloy that suffers from low material quality.

In the Shockley-Queisser (SQ) model, the radiative efficiency, u, equals 1 and the so-called Shockley-Queisser limit represents the maximal efficiency achievable for a simple p-n junction solar cell.

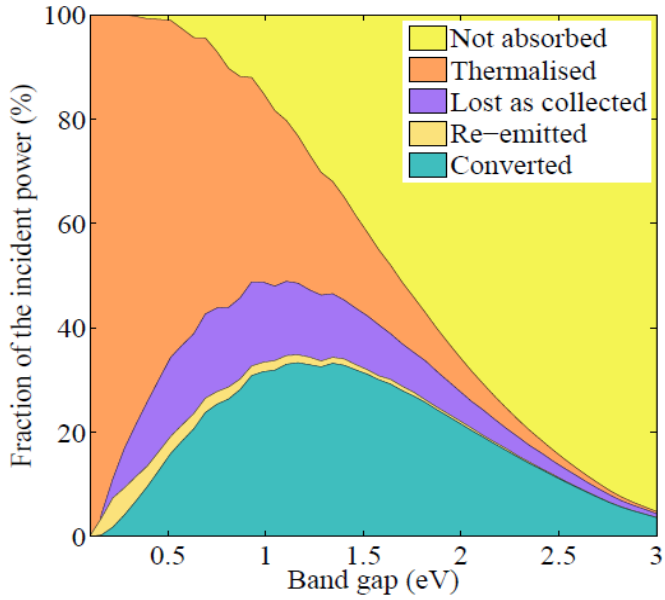

Figure 1.3.1-1: Detail of the losses happening in a solar cell as a function of the band gap energy. It appears that the maximal efficiency is reached for E_G= 1.4eV. From [32].

1.3 Third generation systems

Nowadays several possibilities are explored in order to overcome the Schockley-Queisser limit. Among them we can distinguish different types of solutions: spectral modelling of light (up and down-conversion), high carrier density systems (hot-carrier and multiple-exciton generation) and multi-transition systems (multi-junction and Intermediate band devices).

A simple way to understand the p-n junction's limit is to consider the inherent trade-off between open-circuit voltage and short-circuit. This situation is well illustrated by Figure 1.3.1-1, which depicts the spectral efficiency of photovoltaic conversion and points out that the main losses are due to non-absorption, that affects the short-circuit current, and thermalisation processes, that is a loss of potential energy directly linked to the open-circuit voltage. As these two processes are opposite to each other as respect to the band gap energy, a trade-off has to be made. The optimised trade-off is met for a band gap energy of 1.4eV for the AM1.5 spectrum. Now if we consider that several transitions occur in the same device, each transition energy will convert only a part of the solar spectrum, making non-

absorption and thermalisation losses decrease. Two concepts using multi-transition process exists nowadays: the multijunction solar cells and the intermediate band solar cells. These concepts will be detailed below.

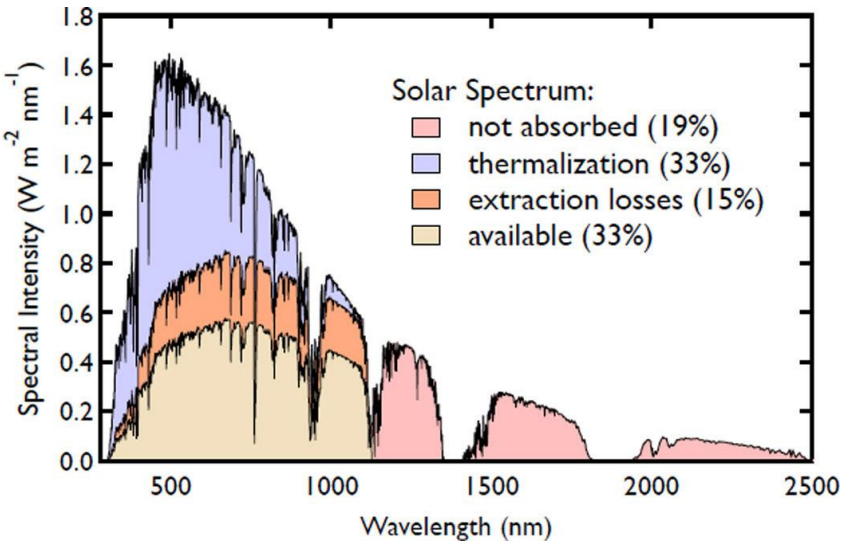

Figure 1.3.1-1: Spectral conversion efficiency and losses in the photovoltaic process for a Silicon based p-n junction.

1.3.1 Multijunction solar cells

This is the oldest and most mature third generation solar cell concept. It has been originally developed for extra-terrestrial applications, especially for satellite power supply. Up to now, multijunction solar cells are the only third generation concept that have passed the Schockley-Queisser limit, and exhibited efficiencies up to 46% for four-junction solar cells and 44.4% for three-junctions [9]. As for the modules, the record efficiency is 36.7% [9].

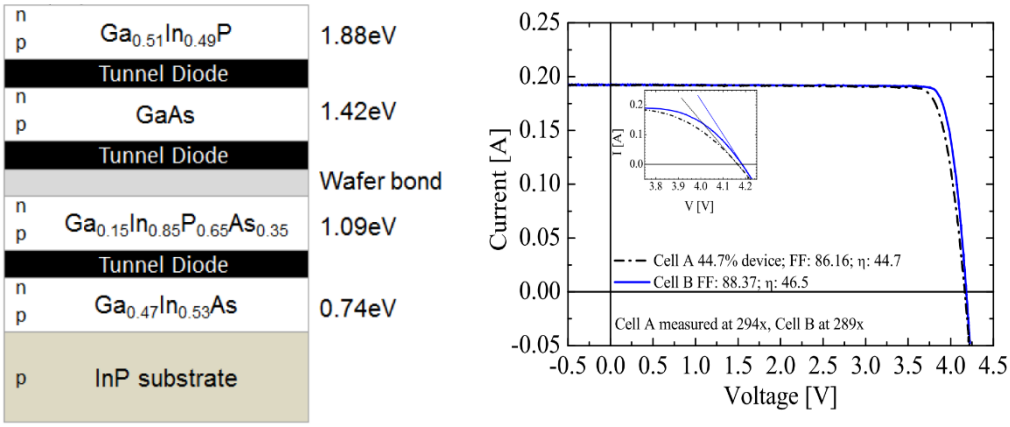

(a) (b)

Figure 1.3.1-1: Structure of the record four-junction solar cell (a) and its corresponding J-V curve, measured under 289 suns (b). From [33].

The basic principle of multijunction solar cells is depicted Figure 1.3.1-2. We consider here the case of two subcells for simplicity. The top cell absorbs the high energy part of the solar spectrum, whereas the bottom cell absorbs the rest. The two cells are working in series, meaning that the total current of the device equals the lower current of the two subcells whereas its voltage equals the sum of the two subcells' voltage. To avoid non collected absorption and reach an optimised efficiency the two subcells should hence generate the same current. This condition is called current-matching and is a fundamental principle of tandem solar cell. To fulfil this condition, we can vary two parameters: the band gap energies and thicknesses of the two subcells. In our case, since we assume full absorption in the two subcells, we can only consider the band gap energies. The serial connection is ensured by the tunnel junction. Its role is to allow recombination between electrons and holes at the interface between the two subcells (cf. Figure 1.3.1-2.). Without the tunnel junction, the two diodes would just work as one with the lower band gap energy. Of course, the tunnel junction should have a large band gap energy, which insures non parasitic absorption and surface passivation, and should be very thin in order to allow for the carriers to tunnel through (typically few ten nanometres).

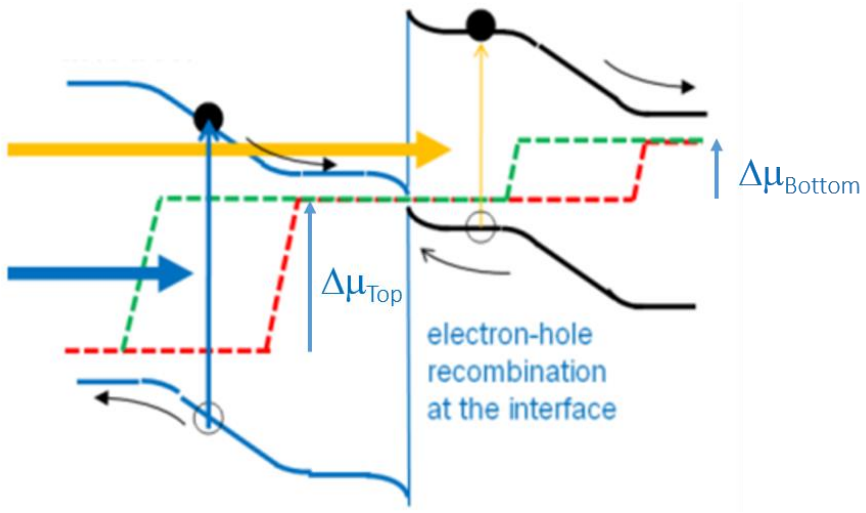

Figure 1.3.1-2: Energy band diagram for a tandem cell. The role of the tunnel junction in the serial connection between the two subcells is outlined here. From [34].

Efficiency limit calculation

Here we apply the same method as presented Sec.1.1 adding the specific behaviour a tandem solar cell [10], [35]–[37]. We assume that both subcells are thick enough to fulfil the total absorption condition above their band gap energies. The bottom cell absorbs only between E_{G_1} and E_{G_2}. The current is not anymore related to the total absorption in the device but equals the lower subcells' absorption. An infinite carrier mobility is supposed, i.e. the Δμ is uniform within the materials' volume. In that case, as seen previously, the subcells' voltage $qV_{subcell}=\Delta\mu_{subcell}$ and $qV=\Delta\mu_1+\Delta\mu_2$. Finally, we neglect photon recycling.

Therefore, Eq.(1.2-1.) becomes:

$$J = q\left(\min(\dot{N}_{abs_{top}}, \dot{N}_{abs_{bottom}}) - \dot{N}_{em}(V)\right) \qquad (1.3\text{-}1.)$$

with

$$\dot{N}_{abs_{top}} = \frac{f}{4\pi^2\hbar^3c^2}\int_{E_{G_2}}^{\infty}\frac{E^2dE}{exp\left(\frac{E}{kT_s}\right)-1} \qquad (1.3\text{-}2.)$$

$$\dot{N}_{abs_{bottom}} = \frac{f}{4\pi^2\hbar^3c^2}\int_{E_{G_1}}^{E_{G_2}}\frac{E^2dE}{exp\left(\frac{E}{kT_s}\right)-1} \qquad (1.3\text{-}3.)$$

Whereas the emitted photon flux is expressed as:

$$\dot{N}_{em}(V=\mu_1+\mu_2) = \frac{1}{4\pi^2\hbar^3c^2}\left[\int_{E_{G_1}}^{\infty}\frac{E^2dE}{exp\left(\frac{E-\Delta\mu_1}{kT_C}\right)-1} + \int_{E_{G_2}}^{\infty}\frac{E^2dE}{exp\left(\frac{E-\Delta\mu_2}{kT_C}\right)-1}\right] \qquad (1.3\text{-}4.)$$

Maximum efficiency for a two junction tandem solar cell is found to be 45.3% efficiency for E_1=0.94eV and E_2=1.61eV for AM1.5 spectrum [10]. The dependence of a two-junction solar cell efficiency on the band gap energies depicted on Figure 1.3.1-3(a). If more junctions are added, the efficiency will increase up to 87% for an infinite number of junctions [35] (cf. Figure 1.3.1-3 (b)).

This technology is therefore very interesting, but suffers from expensive fabrication methods, especially because of the need of two substrates for the record four-junction solar cell for instance. From this point of view, the intermediate band solar cell is more promising.

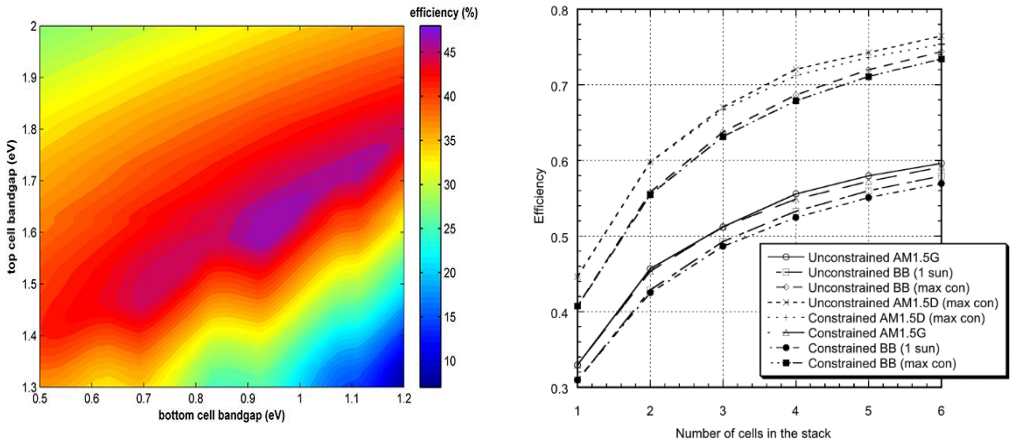

(a) (b)

Figure 1.3.1-3: (a) Mapping of the conversion efficiency for a two-junction solar cell as a function of the band gap energies of the two subcells. From [38]. (b) Evolution of the thermodynamic efficiency of multijunction solar cells as a function of the number of junctions. From [10].

1.3.2 Intermediate band solar cells

In an intermediate band solar cell (IBSC), all the transitions are occurring in the same material. The idea is to insert one or a few band levels in the middle of the bandgap energy E_G of the host material. Three strategies have been investigated: quantum-confined heterostructures (quantum dots and quantum wells), highly mismatched alloys, and addition of impurities. The IBSC principle is depicted in Figure 1.3.2-1. In addition to the classical transition from the valence band to the conduction band of energy E_G, two transitions occur through the intermediate band, of energy E_I and E_H, giving rise to only one electron-hole pair. Electrically this device is equivalent to a two junction tandem solar cell in parallel to the host material diode (cf. Figure 1.3.2-2(a)). From this equivalent electrical scheme we can derived the following set of equation:

$$J_2 = J_3 \tag{1.3-5.}$$

$$J = J_1 + J_{2,3} \tag{1.3-6.}$$

$$qV = \Delta\mu = \Delta\mu_1 = \Delta\mu_2 + \Delta\mu_3 \tag{1.3-7.}$$

Figure 1.3.2-2 displays the J-V characteristics for an ideal IBSC. Compared to the host material, the IBSC exhibits a higher J_{sc}, as expected from the above equations, but a slightly lower V_{oc}. This is because of the additional radiative recombination.

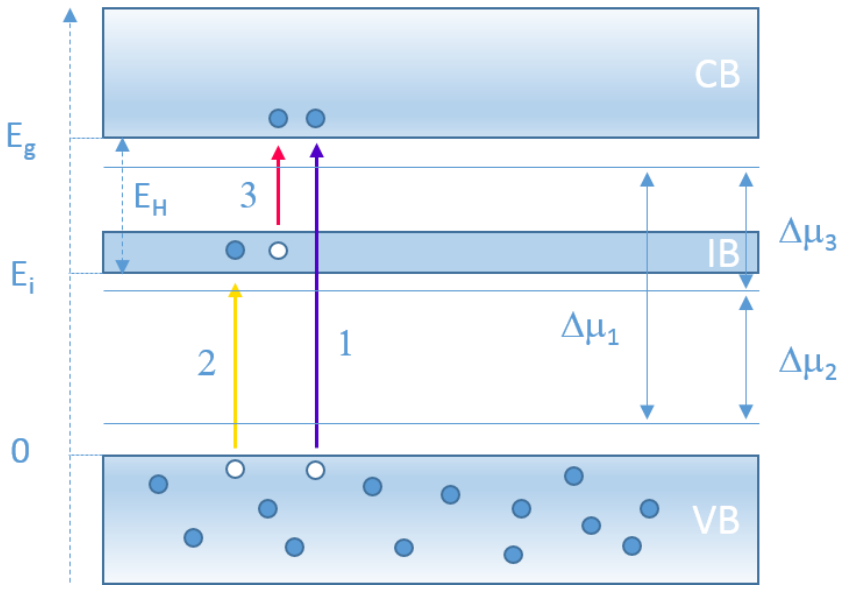

Figure 1.3.2-1: Scheme of the Intermediate band solar cell working. The three transitions involved in the IBSC concept are depicted, with their associated Δμ.

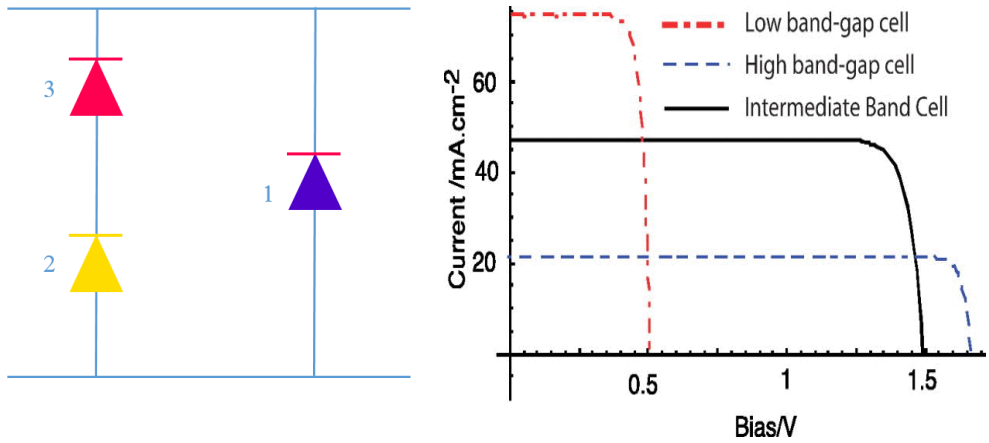

Figure 1.3.2-2: (a) Equivalent electrical circuit of an IBSC. The two transitions implying the IB represented by two diodes in serial connection, in parallel with the diode of the host material transition. (b) J-V curve of an ideal IBSC compared with the high (low) band gap cell. From [39].

1.3.2.1 Thermodynamic limit of IBSC

We want now to determine the efficiency limit of the IBSC. The assumptions made in Sec.1.2 are still applicable here. In addition, specific assumptions are made: no absorption overlap exists, meaning an optimised absorption of the solar spectrum: if assume $E_H < E_I$ and E the photon energy, if $E < E_H$ no absorption occurs, for $E_H < E < E_I$ the photon is absorbed from the IB to the CB, for $E_I < E < E_G$ photons are absorbed by the IB and if $E > E_G$ absorption is made by the host material.

Following the equivalent electrical scheme, we write the devices' total current as:

$$J = q\left(\min\left(\dot{N}_{abs_{VI}}, \dot{N}_{abs_{IC}}\right) + \dot{N}_{abs_{VC}} - \dot{N}_{em}(V)\right) \qquad (1.3\text{-}8.)$$

with

$$\dot{N}_{abs_{VC}} = \frac{f}{4\pi^2\hbar^3c^2}\int_{E_G}^{\infty}\frac{E^2dE}{exp\left(\frac{E}{kT_s}\right)-1} \tag{1.3-9.}$$

$$\dot{N}_{abs_{VI}} = \frac{f}{4\pi^2\hbar^3c^2}\int_{E_I}^{E_G}\frac{E^2dE}{exp\left(\frac{E}{kT_s}\right)-1} \tag{1.3-10.}$$

$$\dot{N}_{abs_{IC}} = \frac{f}{4\pi^2\hbar^3c^2}\int_{E_H}^{E_I}\frac{E^2dE}{exp\left(\frac{E}{kT_s}\right)-1} \tag{1.3-11.}$$

and (1.3-12.)

$$\dot{N}_{em}(V=\mu_{CV}) = \frac{1}{4\pi^2\hbar^3c^2}\left[\int_{E_H}^{\infty}\frac{E^2dE}{exp\left(\frac{E-\Delta\mu_{IC}}{kT_C}\right)-1} + \int_{E_I}^{\infty}\frac{E^2dE}{exp\left(\frac{E-\Delta\mu_{VI}}{kT_C}\right)-1} + \int_{E_G}^{\infty}\frac{E^2dE}{exp\left(\frac{E-\Delta\mu_{CV}}{kT_C}\right)-1}\right]$$

The limit efficiency of such a device is calculated at 49% for AM1.5 [40], and reaches 63.2% for a black body radiation at 6000K under maximal concentration. With the same approach, the efficiency of a two intermediate bands solar cell has been evaluated at 71.7% by Brown et al [41]. Lee and Honsberg have even calculated the theoretical limit of tandem solar cell composed of two IBSCs, reaching 73.4% [42].

1.3.2.2 Practical limit of IBSCs' efficiency

Absorption coefficient overlapping

We saw that, for a maximum efficiency, each transition should absorb only the spectral part that correspond to its energy. In the case of tandem solar cells, this is quite easy to do in practice: we should only have sufficient absorber thickness for each junction. For the IBSC on the other hand, as all the transitions occur in the same material, is much more challenging. Lin and Philips have proposed a specific design to tackle the latter quantity this issue [43]. Concerning the transition between the valence band (VB) and the conduction band (CB), this problem can be treated by adding a layer of host material only on the top of the device. Therefore all the photons of energy higher than E_G will be absorbed before the IB material, avoiding those photons to be involved in the two other transitions. As for the two remaining transitions, the idea would be to create an energy gradient in the IB, while allowing conduction in it. This idea is depicted Figure 1.3.2-3.

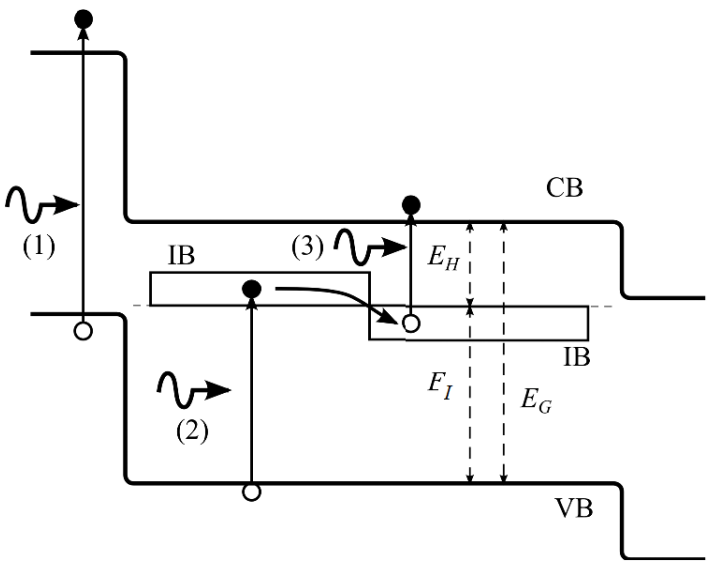

Figure 1.3.2-3: Specific design limiting the absorption coefficient overlap. This figure has been adapted from [44].

This way all the photons would be absorbed by the most fitted transition.

Dependence on the intermediate band carrier population

As said previously, the two transitions involving the intermediate band are working as tandem cell. The efficiency of this cell will therefore depend on the current matching between these two diodes. In this case nonetheless, this current matching condition will not only be up to the combination of the two band gap energies or thicknesses. As the intermediate band has by definition a finite density of states, both absorption from and towards this IB will depend on the carrier population in it.

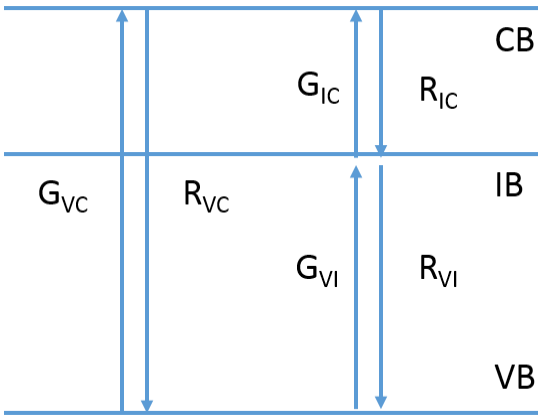

Figure 1.3.2-4: Schematic of an IBSC represented with the different generation an recombination rates.

$$\frac{dn_I}{dt} = G_{VI} + R_{CI} - G_{IC} - R_{IV} + R_{th_{CI}} - R_{nr_{IV}} \qquad (1.3\text{-}13.)$$

We can see that the IBSC design is a fragile balance between the different relaxation times, absorption coefficient and band gap energies association. All those quantities are defined for a given temperature and at a given carrier injection level. Optimisation of an IBSC is hence very complex and must be carefully thought. Having significant density of states in the intermediate band is also crucial here, because in addition to allow a significant current density, it decreases the dependence on the carrier population in the IB.

In conclusion, we have seen that the luminescence is directly related to the open-circuit voltage of a cell, and therefore to the material quality. Combined with the knowledge of the incident photon flux and the absorptivity of the sample, linked to the short circuit current, we can perform an all optical J-V measurement. This is particularly interesting for third generation solar cells that barely exist in complete form up to day. Furthermore, multi-transition solar cells are exhibiting high conversion efficiencies with 63% for IBSC and 46% for a two-junction solar cell. Those conversion efficiencies are however strongly dependent on the behaviour of each transitions. We understand that in order to characterise multi-transition devices, we need to study all the radiations separately. In this perspective, luminescence based characterisations are a powerful and versatile tool.

Chapter 2

Experimental setups and methods

In this thesis, we will focus on the characterization of several type of solar cells. The variety of these solar cells, of their physics and their specific problematics will lead us to use a large spectrum of characterisation methods. In this chapter, we will present those methods and the associated experimental setups.

First we will introduce the classical tools for opto-electrical characterisation of solar cells: current-voltage characteristics, quantum efficiency and absorption measurement.

The largest part of this chapter will then be dedicated to the photoluminescence (PL) and its intensity, spatial and spectral properties. A classical homemade confocal microscope is first described. The versatility of this setup allows us to use it for several analysis that we will detail: PL measurement, time-resolved photoluminescence (TRPL), photoluminescence excitation (PL-E) and local EQE measurements.

We will then introduce an original and powerful experimental tool, the hyperspectral imager that records spectrally resolved luminescence images with an absolute measurement of the emitted photon flux. The absolute calibration of this setup will be detailed.

2.1 Classical solar cell characterisations

Standard characterisation setups dedicated to solar cells are used to investigate the samples. We can distinguish two main characterisations: EQE and J-V characteristic measurements.

2.1.1 Quantum efficiency measurements

External and internal quantum efficiencies (EQE and IQE) measurements are key characterisations of solar cells. Those quantities are defined as follow:

$$EQE(\lambda) = \frac{I(\lambda)}{N(\lambda)} \tag{2.1-1.}$$

$$IQE(\lambda) = \frac{I(\lambda)}{N(\lambda) * A(\lambda)} \tag{2.1-2.}$$

I(λ) is the recorded current, N(λ) is the total number of incident photons and A(λ) the absorption in the sample. In other words, EQE (λ) gives the ratio of collected carriers on incident photons per wavelength. With the IQE measurement we free ourselves of optical losses, making this characterisation very interesting in view of investigating the recombination mechanisms and the carrier transport properties. These physical quantities are crucial for the development of a new material and will be used in the Chapter 3, dedicated to the GaAsPN solar cell. EQE measurements will also be used as an approximation for the absorption, under specific conditions.

EQE are measured by an Oriel IQE200 from Newport. This setup allows us to work in the 300-2500nm range. A Xenon Lamp is used for the excitation, and the selection of the wavelength is made by a monochromator. The calibration of the incident power is done by two detectors, one made in silicon for the 400-1100nm range, and one made in Germanium for the 1100-2500 nm range. In addition, we can use an integrating sphere to record scattered and specular reflection. With this

reflectometry measurement, assuming that the transmission is null, we can calculate the internal quantum efficiency:

$$IQE(\lambda) = \frac{EQE(\lambda)}{1 - \left(R_{scattered}(\lambda) + R_{specular}(\lambda)\right)} \qquad (2.1\text{-}3.)$$

Local EQE

External quantum efficiency gives macroscopic measurements of a solar cell's performances. But, if the sample is not homogeneous, a local EQE can be more instructive. This can be the case in complex alloy, for which clusters and composition fluctuation can appear [45], or in a quantum confined heterostructures where a spatial inhomogeneity of the quantum structure dimensions can be observed. This experiment can be performed by a white light source (lamp or supercontinuum laser) coupled with a microscope.

2.1.2 J-V characteristics

Electrical J-V measurement is the ultimate performance test for solar cells. The cells efficiencies are determined by a Oriel Sol3A solar simulator manufactured by Newport. It is an AAA solar simulator. This rate designates the spatial homogeneity, spectral and intensity specifications. We used a Keithley 2635B sourcemetre to acquire the electrical signal and a chiller to maintain the sample temperature at 25°C.

The J-V characteristics determined in optical considerations only (cf. Sec. 1.2) are an ideal case. From the absorber to the terminal, the carrier encounter several loss sources that have to be considered. We will now make the parallel with the first chapter where we used a pure optical model.

As we deal here with classical electrical model, we include resistances in the electrical equivalent circuit for the solar cell, following the schematic in Figure 2.1.2-1.

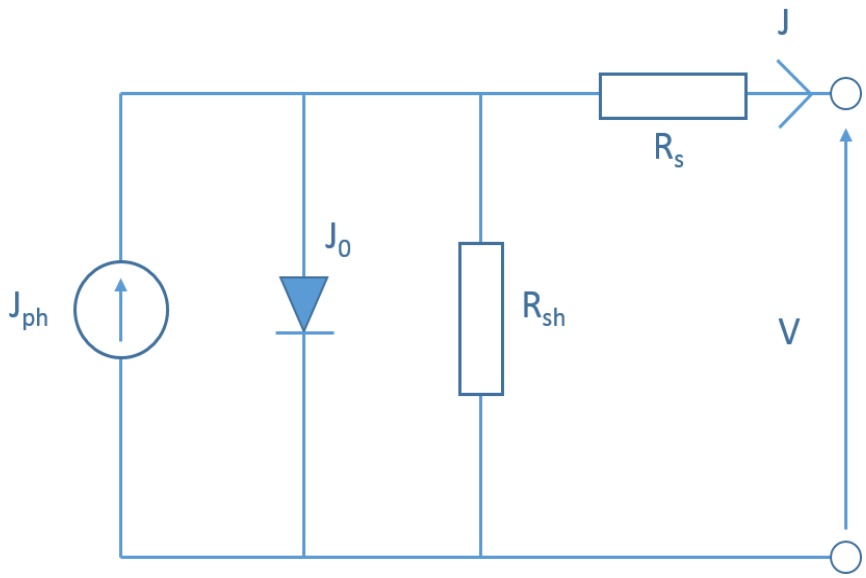

Figure 2.1.2-1: Equivalent electrical circuit of a solar cell for a one diode model. J_{ph} and J_0 are the photocurrent and the saturation current, while R_s and R_{sh} are the series and shunt resistances respectively.

In dark conditions, the current-voltage characteristic is expressed by the following relation supposing a one-diode model [19]:

$$J_{dark}(V) = J_0 \exp\left[\left(\frac{q(V - R_s J)}{nkT}\right) - 1\right] - \frac{V - R_s J}{R_{sh}} \qquad (2.1\text{-}4.)$$

Where J_0 is the saturation current, R_s the series resistance and R_{sh} the shunt resistance.

If we assume only radiative recombinations,

$$J_0 = J_0{}^{rad} = \int_{E_g}^{\infty} EQE(E)\Phi_{BB}(E, T = 300K)dE \qquad (2.1\text{-}5.)$$

Under illumination, a minority carriers current $J_{photocurrent}$ arises in the opposite direction to J_{dark} such as the complete current expression is:

$$J(V) = J_{dark}(V) - J_{photocurrent}(V) \qquad (2.1\text{-}6.)$$

The photocurrent is a general term that includes the voltage dependence of the photogenerated current $q\dot{N}_{abs,sun}$. The voltage dependence, called the carrier collection efficiency, will be used in chapter 3 and is expressed by:

$$\rho(V) = \frac{J_{photocurrent}(V)}{q\dot{N}_{abs,sun}} \qquad (2.1\text{-}7.)$$

In most cases, there is no problem of collection at V=0V and $q\dot{N}_{abs,sun} = J_{sc}$, so this relation is often expressed in function of J_{sc}, instead of the photogenerated current. J_{sc} is the short-circuit current:

$$J_{sc} = \int_{E_g}^{\infty} EQE(E)\Phi_{sun}(E)dE \qquad (2.1\text{-}8.)$$

This value is important because it defines the current of the diode at the beginning of the power production area. Its theoretical limit, when no collection losses are exhibited by the solar cell at 0V, is: $J_{sc,max} = q\dot{N}_{abs,sun}$. The end of this region is given by the open circuit voltage V_{oc}. The open-circuit voltage is found by solving Eq. (2.1-6.) with $J(V_{oc})=0$:

$$V_{oc} = nkT\left[ln\left(\frac{J_{photocurrent}(V_{oc})}{J_0}\right) + 1\right] \qquad (2.1\text{-}9.)$$

The theoretical maximum of the open circuit voltage is reached when only radiative recombinations and no collection losses are present in the cell:

$$V_{oc}{}^{rad} = kT\left[ln\left(\frac{q\dot{N}_{abs,sun}}{J_0{}^{rad}}\right) + 1\right] \qquad (2.1\text{-}10.)$$

This value will be compared to the obtained V_{oc} in Chapter 3. Rau et al have also demonstrated that the difference between those two values are linked to the external quantum efficiency of LEDs [46].

2.2 Spectrophotometry

Optical characterisations, such as reflexion, transmission or absorption of solar cell material are primordial. Absorption loss is the first phenomenon to consider in a solar cell. There are multiple characterisation methods to get to the absorption: direct, such as spectrophotometer, ellipsometry measurements or indirect, for instance with PL intensity using the generalised Planck's law. A spectrophotometer uses a calibrated light source that pass through a grating which transmits a thin spectral interval. The light is then guided to the sample that is placed at the front (back) of an integrating sphere where the transmitted (reflected) light will be measured. By its lambertian inner surface, the integrating allow the light to be indefinitely reflected until it reaches the detector. The light intensity is compared with a reference beam, and the transmission (respect. the reflexion) is calculated. From these measurements we can extract the absorption coefficient of the sample. This value is a key parameter. Indeed, it governs the absorber thickness needed to absorb the excitation light. Therefore, it is a necessary value in numerical simulation and solar cell structure design. Figure 2.1.2-1 describes the spectrophotometer design. Its spectral resolution goes down to 0.05nm, depending on the experimental parameters.

I_0 is the incident light intensity, I_R the reflected light intensity and I_T the transmitted one. In the simplest configuration, with only one material, we can deduct from the Beer-Lambert's law the absorption coefficient of the sample:

$$I_T = I_0(1 - R)e^{-\alpha e} \qquad (2.2\text{-}1.)$$

For complex samples with different layers, one has to take into account the possible reflexion at each interfaces, and also the potential interferential patterns. Hypothesises taken for our samples will be detailed in the corresponding sections.

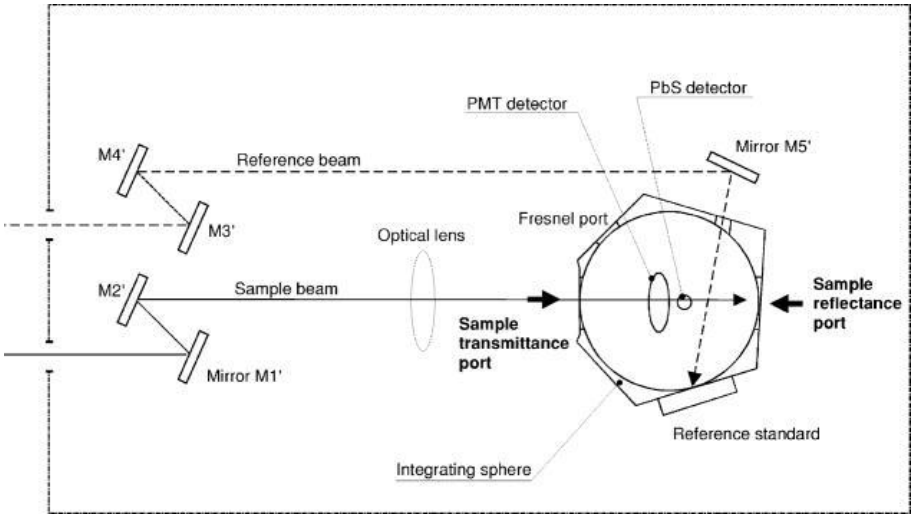

(a)

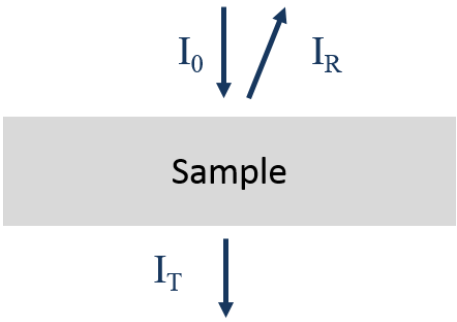

(b)

Figure 2.1.2-1: (a) Sketch of the lambda 900 spectrophotometre. (b) Sample considered and physical values of interest.

2.3 Photoluminescence

In this section, we will describe the different techniques based on PL used in this thesis. Several systems and setups exist, whether we are interested in the intensity, spectral or spatial properties of the luminescence. Based on the luminescence of the solar cell introduced in the previous chapter, we will explain how, from this PL signal, we can extract the desired physical quantities for each experimental setup.

2.3.1 Confocal microscope

The system used in this work is a homemade classical confocal microscope featured Figure 2.3.1-1 that allows the different experimental characterization technics described below. Here the pinholes, responsible for the "confocal" mode, are replaced by optical fiber of diameter between 6 and 60µm depending on the application. In this range of diameter, the confocal mode is guaranteed. Its theory is widely exposed in literature [47]–[50].

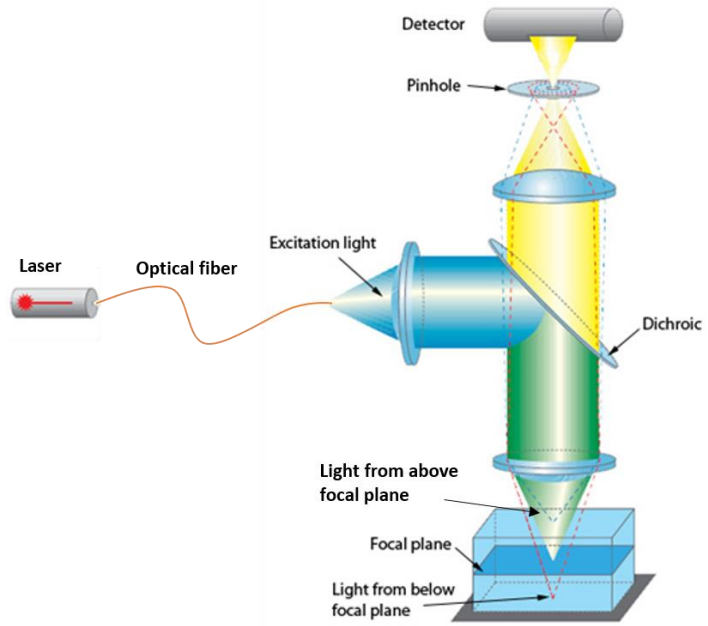

Figure 2.3.1-1 : Sketch of the confocal microscope. The role of the pinholes on the axial resolution is outlined here. From [51]

The main specifications for this setup are the excellent lateral and axial resolutions, given by [47]:

$$\Delta x = \frac{0.42\ \lambda_{exc}}{NA} \tag{2.3-1.}$$

$$\Delta z = \frac{1.4 n \lambda_{exc}}{NA^2} \tag{2.3-2.}$$

Where NA is the numerical aperture of the system, λ_{exc} the excitation wavelength, and n the refraction index of the analysed material. This homemade microscope is particularly versatile and will support all the setups described in the following.

2.3.1.1 Photoluminescence spectra measurements

As demonstrated previously, luminescence is a powerful tool to estimate the performances of the solar cells such as the absorbance, the open-circuit voltage or the photocurrent. Crystalline orientation can even be probed when combined with polarisation analysis [52]–[54].

For the simple PL spectra measurement, a laser excitation is coupled into the injection optical fibre. The laser beam is then collimated using a lens chosen to adapt the spot diameter with the objective pupil. The laser is then directed towards a beamsplitter where it is reflected to the sample. The generated luminescence is collected by the objective, get through the beamsplitter and is coupled into the collection optical fibre. A spectrometer from Princeton Instruments records the luminescence spectra with a spectral resolution down to 0,14nm with a 1200g/mm grating at 450nm [55].

All the PL spectra are spectrally corrected. The spectral calibration aims to determine the spectral response of the system. We use a calibrated lamp coupled in an integrating sphere, which is a sphere with inner surface close to a lambertian reflector. The light is reflected numerous times before escaping the sphere. The output is therefore a lighting surface with several homogeneous properties:

intensity, radiance, spectrum and angular distribution. All the spectral modification observed is induced by the optical system. This spectrum is designated as *Reference spectrum (x, y, λ)*, and the *Recorded spectrum (x, y, λ)* is the acquisition made by the spectrometer, with:

$$R(\lambda) = \frac{Recorded\ spectrum\ (\lambda)}{Reference\ spectrum\ (\lambda)} \qquad (2.3\text{-}3.)$$

Each acquisition will be corrected by the system response:

$$Corrected\ spectrum(\lambda) = \frac{Recorded\ spectrum\ (\lambda)}{R(\lambda)} \qquad (2.3\text{-}4.)$$

2.3.1.2 Photoluminescence excitation

Photoluminescence excitation (PL-E) consists in recording the PL signal while varying the excitation wavelength. We will use this characterisation tool to apprehend the absorption in the layer of interest. Indeed a look to the generalised Planck's law shows that the only physical quantity that should change with the wavelength is the absorption. Also, as the luminescence is layer selective, we can access the absorbance of a particular layer in a stack. Finally, excitonic features can be accessed with PL-E measurements [56]. However, the variation of luminescence intensity obtained has to be corrected by the incident power, and quantitatively calibrated. The calibration can be done by normalizing with a known value of the absorption (typically at short wavelength the absorption is set to 1). In this thesis we are particularly interested in the resonant PL-E measurement. The complexity in this case consists in recording the luminescence without being disturbed by the laser reflexion. Pr. Heitz and his team have recorded the PL signal coming from excited states of quantum confined heterostructures and corrected this signal by the thermionic transition [57]. One can also use phonon replica for reconstruct the PL-E spectrum [58]. Another possibility to extinct the laser

reflexion is the use of two linear polarisers, one to control the polarisation of the incident laser and one orthogonally positioned to block the lasers' reflexion. As we work at room temperature, the luminescence induced by a linearly polarised laser does not keep this polarisation, and the PL signal will only be reduced. We chose this configuration for our experiments.

The experimental setup used to perform PL-E relies on the confocal microscope. The excitation source is a Fianium supercontinuum laser whose wavelength is selected using a Photon Etc Laser Line Tunable Filter. This laser works in the 450-2500nm range. The spectral resolution is 2 nm while the extinction ratio is higher than 10^5. The laser is coupled into an optical fibre connected to the confocal microscope. Here, because of the large range excitation wavelength, we use a 50:50 beamsplitter operating in the 350-1100nm range. The sample is then excited using a microscope objective (either reflective or apochromatic, both giving the same results). The two polarisers have an extinction ratio higher than 10^5.

A typical PL-E curve measured on a multiple quantum wells sample is depicted Figure 2.3.1-2. The corresponding EQE is plotted on the same axis. A good correlation is found between the two quantities, even in the quantum wells levels spectral region.

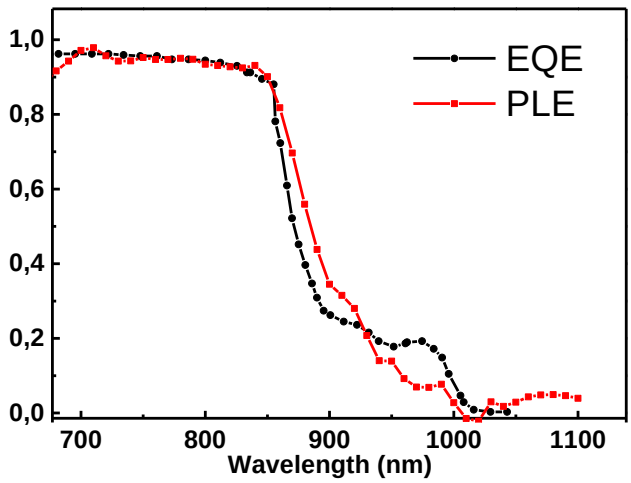

Figure 2.3.1-2: Comparison between PLE and EQE for a multi-quantum wells sample, introduced and detailed in chapter 4.

2.3.1.3 Time-resolved photoluminescence

Time-resolved photoluminescence (TRPL) is a useful technique to access the carrier dynamics. It consists in recording the PL as a function of time. There are four main technics for recording TRPL:

- Streak camera
- Time-correlated single photon counting
- Pump-probe
- Up-conversion

Streaks cameras are able to record the temporal evolution of the PL spectra. Their time resolutions are good, going down to 3 ps whereas the fastest luminescence decay characteristic times are around hundred ps. The conservation of the spectral information is another great advantage of the streak cameras.

Time-correlated single photon counting on the other hand is based on the detection of single photons of a light signal periodically induced by the supercontinuum laser described in the previous section. Based on the measurement of the detection time,

the reconstruction of the temporal evolution of this signal is made. The photons counted are not energetically discriminated and the spectral information is thus lost. By adding a monochromator, we can reconstruct the spectral information. The force of this technic is its very good sensitivity.

This is the technology we used for the TRPL measurements during this thesis. The pulsed source is the supercontinuum laser introduced in the previous section. The single photon counting detector used is an ultra-low noise silicon avalanche photodiode τ-SPAD from Picoquant. The overall temporal resolution of our system is 350ps.

2.3.2 Hyperspectral Imager

The hyperspectral imager (HI) is an original tool that records intensity, spectral and spatial properties of the luminescence in one acquisition. Moreover, this setup can be absolutely calibrated to measure the luminescence flux. This highly valuable property will be particularly used in this thesis.

2.3.2.1 Setup

The basic principle of the HI is to record images of PL at various detection wavelength, which all together form a cube. Hyperspectral Imagers are known, especially in the biology research field [59], [60], but only little known in the photovoltaics field [27], [28], [61]–[63]. Those systems can probably not be absolutely calibrated, or at least do not use this property. Our system has been developed by Photon etc, in collaboration with IRDEP during Dr. Delamarre 's thesis [64] for photovoltaics applications. It relies on volume Bragg gratings. A schematic of the whole setup is displayed Figure 2.3.2-1.

The sample is illuminated by a laser source through a microscopic objective, after a reflection by a beamsplitter. The luminescence is collected by the same objective. The hyperspectral image is formed by volume Bragg gratings and recorded by a CCD detector.

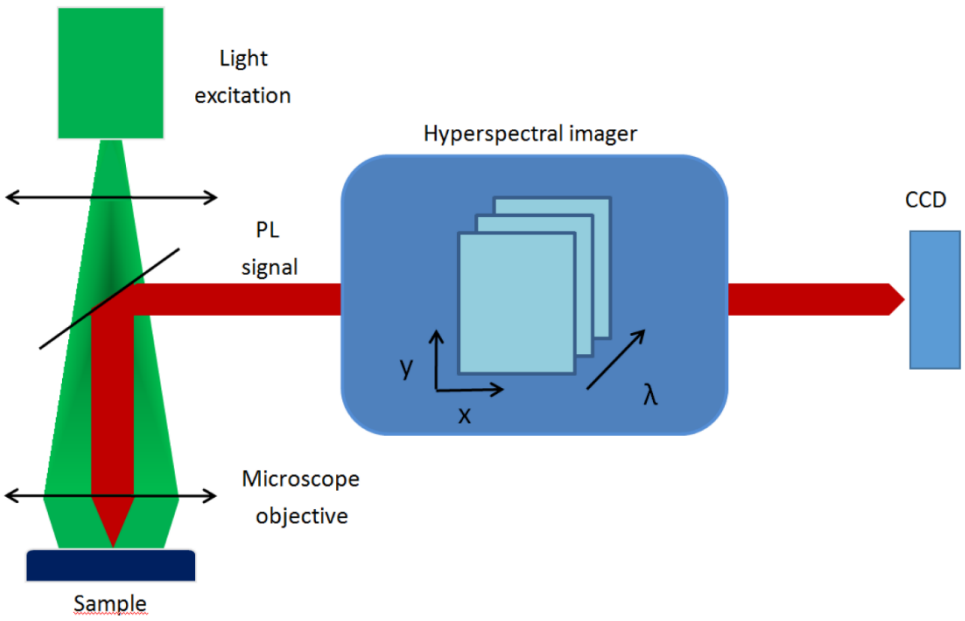

Figure 2.3.2-1: Principle of Hyperspectral imaging: experimental configuration for uniform sample excitation, a hyperspectral imager, and a CCD detection. An hypercube of data (x,y,λ,Intensity) is acquired with a CCD camera as explained in the text. At each spatial location, a luminescence spectrum with calibrated data is obtained. Conversely, maps of luminescence intensities for each wavelength can be extracted.

2.3.2.2 Device calibration

In order to accurately acquire the spectral, spatial, and intensity information of the luminescence, the HI has to be calibrated. This calibration method is decomposed in two steps: a spectral calibration and an absolute one.

This calibration is similar to the one detailed for the confocal microscope. This time, however, R(x, y, λ) applies to an image, and the calibration has to take into account the spatial information. So, the HI images the output surface of the integrating sphere. With such a surface, all the variations recorded on the camera will have been introduced by the optical system. This image is designated as *Reference image (x, y, λ)*, and the *Recorded image (x, y, λ)* is the acquisition made by the HI, with:

$$R(x, y, \lambda) = \frac{Recorded\ image\ (x, y, \lambda)}{Reference\ image\ (x, y, \lambda)} \tag{2.3-5.}$$

Each acquisition will be corrected by the system response:

$$Corrected\ cube(x, y, \lambda) = \frac{Recorded\ cube\ (x, y, \lambda)}{R(x, y, \lambda)} \tag{2.3-6.}$$

The second step, the absolute calibration, is then done to complete the calibration. This calibration will convert the intensity from counts to photons emitted per second, surface volume and energy interval. The whole procedure is detailed in [65]. Basically, the idea here is to record the output of an optical fibre coupled to a laser. Knowing the optical power at this output, measured with a powermeter, we can consequently determine the ratio of emitted light that is recorded, and then correct the acquired cubes.

Chapter 3

Dilute nitride for multi-transitions photovoltaic systems

Dilute nitride semiconductors has generated ongoing interest because of unique structural and opto-electronical properties. Indeed the addition of a small fraction of nitrogen in standard III-V semiconductors, as GaAs, implies a huge effect on the bandgap energy and the lattice parameter. By introducing several competing atoms among which one with high electronegativity (for instance Nitrogen or Oxygen) for a same crystalline site, one can tune the lattice constant, whereas the band gap energy tuning is due to the localisation of the electronic states. Those effects make dilute nitride very convenient in a large range of opto-electronical devices, such as lasers [66]–[69], communication devices [70], [71] and in multi-junction solar cells [72]–[74], where the control of band gap energy and the lattice parameter is crucial [75]–[77]. Therefore we find dilute nitride in several multi-junction solar cells systems, which are grown on Ge or GaAs substrate. These very expensive substrates make multi-junction solar cells uncompetitive compared to single junction Silicon solar cells. We want to take advantages of the dilute nitride to develop a tandem cell grown on a silicon substrate, hence benefiting of the excellent III-V semiconductor opto-electronical properties and of the silicon solar cells mature technology and competitiveness.

We will first introduce the specific optoelectronic behaviour of dilute nitride alloys, as well as the samples description that we investigated in this thesis.

Then we will present numerical simulations of typical GaAsPN-based solar cells and their opto-electrical characterizations. This part will show classical measurements such as J-V characteristics and EQE as well as other fundamental characterizations such as spectrally and time resolved photoluminescence.

Afterwards, we will discuss the results on specific points like the annealing effects, the collection issues, the material heterogeneity and the correlation between optical characterisations and cells parameters.

Finally, a perspective towards the use of such devices as Intermediate Band Solar Cells will be presented.

3.1 Dilute nitride alloys

This first section introduces general dilute nitride properties and the description of the investigated samples.

3.1.1 Dilute nitride III-V alloy for multi-junction solar cells

Nowadays, several MJSCs structures are taking advantage of the specific physics of dilute nitride. As we see Figure 3.1.1-1(a), we can find a dilute nitride alloy lattice-matched to any of the main substrate (GaAs, Ge, InP and Si). The specific behaviour and the versatility of dilute nitride semiconductors is demonstrated on this graph. Standard alloys are following the Vegard's law regarding the evolution of their lattice constant and bandgap energy. This law simply assumes the linearity of those physical values with the concentration of their elements. For example, let's focus on the $In_xGa_{1-x}As$ alloy. According to Vegard's law, its bandgap energy and lattice parameter, a, should follow:

$$E_{g,In_xGa_{1-x}As} = xE_{g,InAs} + (1-x)E_{g,GaAs} \qquad (3.1\text{-}1.)$$

$$a_{In_xGa_{1-x}As} = xa_{InAs} + (1-x)a_{GaAs} \qquad (3.1\text{-}2.)$$

This parametric evolution is displayed on the graph, but instead of being a straight line it is slightly curved. To be more accurate an additional term has to be considered for the bandgap energy equation and Eq.(3.1-1.) becomes:

$$E_{g,In_xGa_{1-x}As} = xE_{g,InAs} + (1-x)E_{g,GaAs} + bx(1-x) \qquad (3.1\text{-}3.)$$

b is called the bowing parameter. For standard alloys, this parameter is close to 0. But for highly mismatch alloys (HMA), among which belong dilute nitride alloys, it can reach giant values and modify completely the bandgap energy variation with the composition, as for GaPN. Thanks to this behaviour, GaAsPN can be lattice-matched on Si for a large range of bandgap energy (cf. Figure 3.1.1-1(a)).

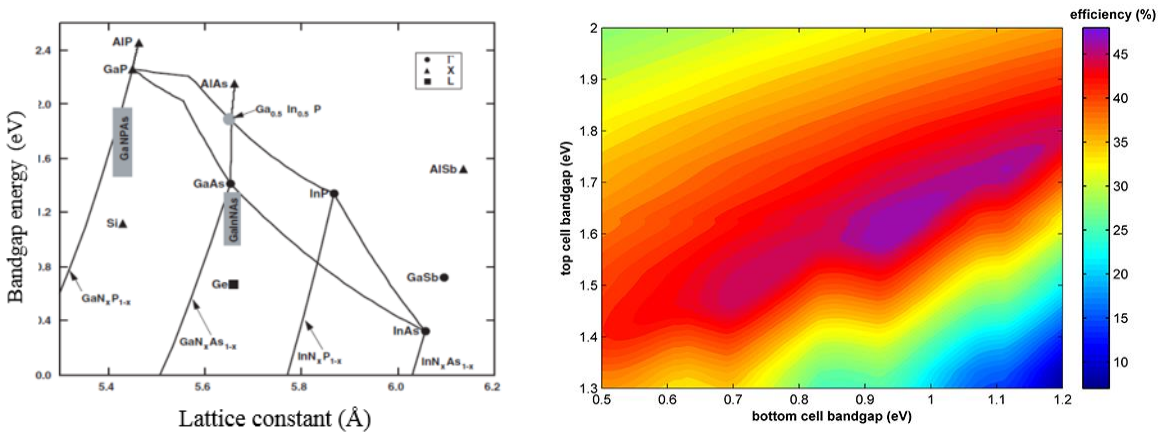

(a) (b)

Figure 3.1.1-1: (a) Bandgap energy of elemental and III-V compound semiconductors over lattice constants. From [78]. (b) Efficiency of tandem solar cell as a function of the two subcells band gap. From [38].

As there is no other elemental or standard III-V alloy lattice-matched on Si and as Si has an ideal bandgap energy for tandem solar cells (cf. Figure 3.1.1-1(b)), GaAsPN is a very interesting alloy to get a low-cost high efficiency tandem solar cell, with a potential efficiency of 45%. Calculation of tandem cells efficiencies has been widely studied under various hypothesis [10], [36], [37], [79], [80].

The next section will detail the origin of such a bowing parameter.

3.1.2 Band anti-crossing theory of GaAsPN

Interaction of N-related states with a conduction band minimum has been theoretically proposed. First studies are based on GaAsN materials and same explanations can be applied to other dilute nitride alloys. A model has been proposed by Pr Zunger's team that is based on pseudo-potential theory [81], [82]. Although this model offers a rigorous explanation, one can use a more empirical model proposed in 1999 by Pr Walukiewicz's group: the Band Anti Crossing (BAC) model. The latter relies on a strong coupling between the localized stated induced by Nitrogen inclusion with the conduction band [83], [84] . The BAC Hamiltonian using the perturbation theory is written:

$$H_{BAC} = \begin{pmatrix} E_M\,(k) & C_{NM}\sqrt{x} \\ C_{NM}\sqrt{x} & E_N \end{pmatrix} \qquad (3.1\text{-}4.)$$

where C_{NM} is a constant, which depends on the semiconductor, and x the mole fraction of substitutional N atoms. E_N is the energy of N-related states, and E_M (k) is the energy dispersion of the conduction band of the III – V host, all referenced to the top of the valence band of the III – V semiconductor host.

According to the BAC Hamiltonian, the interaction of N-related states with the conduction band states results in a splitting of the conduction band into two highly non-parabolic subbands, E_- (k) and E_+ (k), which follow Eq. (3.1-5.) :

$$E_{\pm}(k) = \frac{1}{2}\left[E_N + E_M(k) \pm \sqrt{[E_N - E_M(k)]^2 + 4C_{NM}x}\,\right] \qquad (3.1\text{-}5.)$$

The same interaction exists at the X and L points of the Brillouin zone, and can also be described by the BAC theory. One has just to take into account the dispersion of C_{NM}, since the conduction band states lose the s-like character with the A_1 symmetry. It is observed that the interaction between N-related states and conduction band states at the boundary of Brillouin zone still exists for dilute nitrides [85], [86]. Some experimental evidence of this interaction is provided by Seong, Mascarenhas, and Geisz using Raman scattering [86] and Perkins et al. using the electroreflectance technique [85]. It is found [87] that the C_{NM} (k) element can be expressed as:

$$C_{NM}(k) = \frac{C_{N\Gamma}}{[1 + (ak)^2]^2} \qquad (3.1\text{-}6.)$$

where a is the parameter of the order of lattice constant describing the spatial extent of the N localization wave function and $C_{N\Gamma}$ is the C_{NM} (k) for k=0 , which should be determined from measurements of the band anticrossing interaction in the conduction band at the Γ point. Experimentally, it is observed that C_{NM} (k) at the X point is about 3 times smaller than $C_{N\Gamma}$ [87].

As we said in the introduction, it is common to use the BAC model to any dilute nitrite allow. In the present study we wanted to estimate the influence of Nitrogen inclusion on the GaAsP band gap. Therefore, we have calculated the energy of the subbands taking the BAC parameters values in the literature [88]. Figure 3.1.2(a) shows the band gap evolution regarding the P content. Figure 3.1.2(b) displays the bandgap evolution of GaAsPN with the N content of 0.02 which is typically the value we have in our samples.

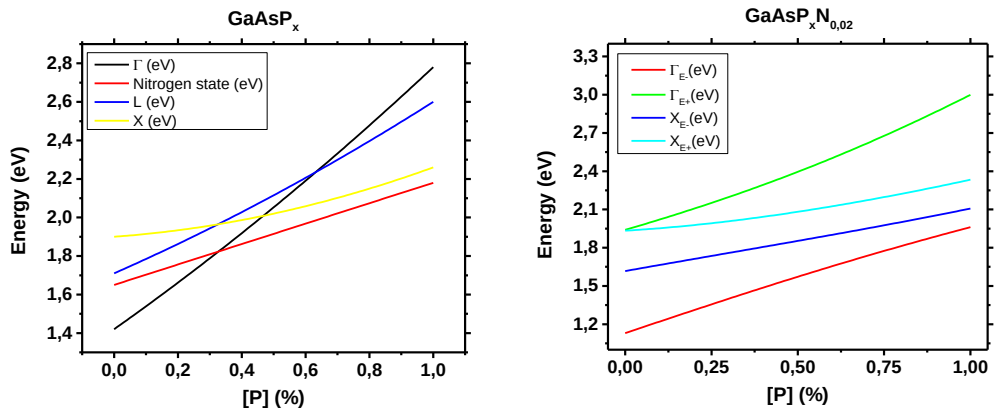

(a) (b)

Figure 3.1.2-1: Band structure of (a) $GaAsP_x$ and (b) $GaAsP_xN_{0.02}$ as a function of Phosphorous content.

3.1.3 Samples description

All the samples analysed in this chapter have been grown by molecular beam epitaxy (MBE) on n-doped GaP substrates at FOTON laboratory at the Institut National des Sciences Appliquées (INSA) in Rennes.

The samples are divided in three sorts:

- Absorbers: 1µm-thick GaAsPN absorber.
- Thick p-i-n diodes : 1µm-thick GaAsPN absorber
- Thin p-i-n diodes: 300nm-thick GaAsPN absorber

3.1.3.1 Absorbers

One absorber is presented in this section which reflects the optical properties of a typical GaAsPN layers grown in the p-i-n diodes: S1378.

The study of solely absorbers allows us to access the material properties without any electrical field, which modify carrier dynamics in complete diodes. In addition, we can measure the absorption profile of the GaAsPN material, which has been published only three times in literature, in the best of our knowledge [78], [89],

[90]. It also allows verifying a bandgap value around 1.7eV which is required in the perspective of the GaAsPN/Si tandem cell.

3.1.3.2 P-I-N diodes

Dilute nitride growth is challenging, with a high defect density and high background doping level, resulting in small minority carrier diffusion length [78], [91]. To overcome this handicap, a p-i-n structure is used. This arrangement is widely used to increase carrier collection in low transport properties material, as a-Si for example[92], with counterpart a lower Voc and fill factor [93]. Indeed, contrary to p-n junctions where the main mechanism of carrier transport is diffusion, it is ruled by drift in p-i-n junctions, i.e. an electric field assists the travel through the device. In the ideal case, this electric field is constant all over the i-layer and its value is:

$$E = \frac{V_{bi} - V}{e_i} \qquad (3.1\text{-}7.)$$

Where V_{bi} is the built-in voltage and e_i the i-layer thickness. Figure 3.2.2-1(a) displays the band structure of a p-i-n solar cell.

Among the cells grown in the MENHIRS project and studied here, two main structures were used: A and B (see Figure 3.1.3-1).

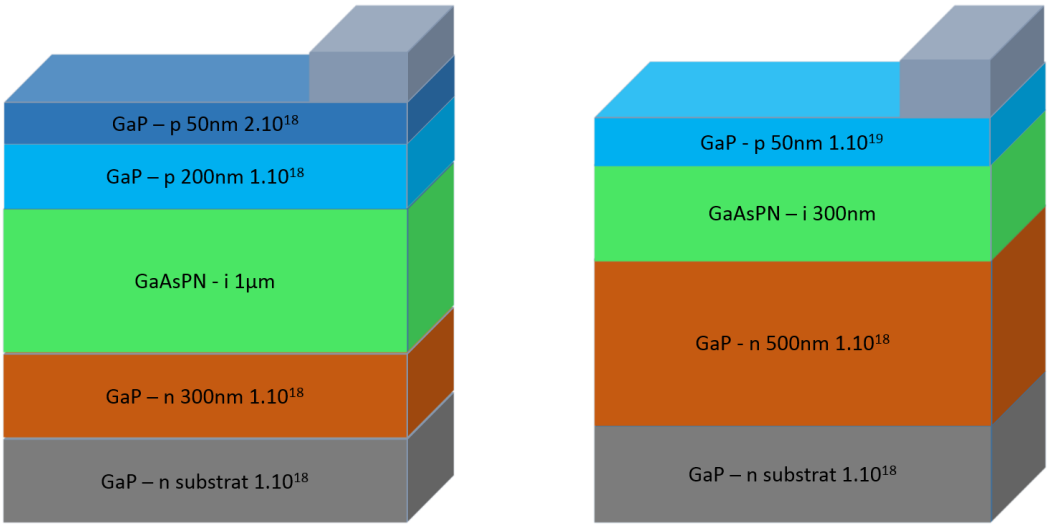

(a) (b)

Figure 3.1.3-1: (a) structure A. (b) Structure B.

Structure A has a 1µm-thick absorber allowing an almost total absorption according to numerical simulations (cf. Figure 3.2.2-1(d)). The window layer is 250nm thick of GaP p-doped at 2.10^{18} with Be dopant. We chose a high thickness to ensure a low sheet resistant layer. Only two samples following this structure are studied in the following, S1372 and S1486, with different annealing conditions.

Structure B is a 300nm thick absorber with higher doping value for the p and n layers. This structure was designed in order to optimise the carrier collection. Indeed, a higher doping value of the GaP p-doped layer at 1.10^{19} combined with a thinner absorber allows a higher electric field in the absorber. Besides, the n-doped GaP layer is thicker, providing a better passivation in respect to the substrate. Eleven wafers from this structure are analysed in this chapter. Table 3.1.3-1 reports all the samples details.

Wafer	structure	[N]	[As]	Annealing conditions
S1378	absorber			800° 1,5,10’
S1372	A			700° 1H; 730° 30’, 1H; 800° 1’, 5’, 10’,15’,30’
S1486	A	2		700° 30’; 800° 1’; 800° 5’-1; 800° 5’-2; 800° 10’; 850° 1’; 800° 5’ thinned 1,2
S1530	B	2		800° 5’
S1568	B	1		800° 5’
S1569	B	1		800° 5’
S1570	B	1		800° 5’
S1571	B	3		800° 5’
S1572	B	3		800° 5’
S1573	B	3		800° 5’
S1574	B	1		800° 5’
S1575	B	1		800° 5’
S1576	B	1		800° 5’
S1579	B	2		800° 5’

Table 3.1.3-1 Samples description including: name, type of structure, nitrogen percentage, annealing condition(s)

3.2 Numerical simulations

This second section will introduce numerical simulations of the p-i-n devices. This part is essential as it helps to understand the role of each layer. In this thesis, attention is given to the top cell.

3.2.1 GaAsPN parameters

The difficulty for simulating GaAsPN top junction is the lack of parameter values for this alloy in literature. Most of the parameters have hence been taken from Vegard's law between GaAsP and GaAsN alloy, much more investigated [88] and taking into account the effect of Nitrogen in GaAsN. For the GaP parameters, we have used the values on the website of Ioffe Institute [94]. Concerning the absorption coefficient, we have experimentally determined it (cf. Figure 3.3.2-3) and we will therefore use this measure in the following simulations.

3.2.2 Ideal case

First, we want to determine the maximum performances reachable with our structures. We have therefore simulated those structures without any defects or carrier collection problems, and taking into account the high reflexion on GaP surface, measured and presented Figure 3.3.2-1. Figure 3.2.2-1 sums up those simulations. In this ideal case, the structure A is more interesting because of the higher current generated.

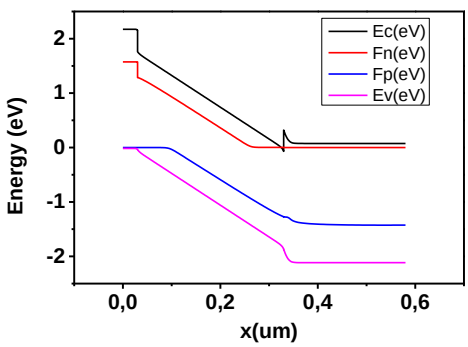

(a)

Structure	A	B
V_{oc} (V)	1.61	1.62
J_{sc} (mA.cm^{-2})	9.9	6.47
η (%)	13.5	9.1

(b)

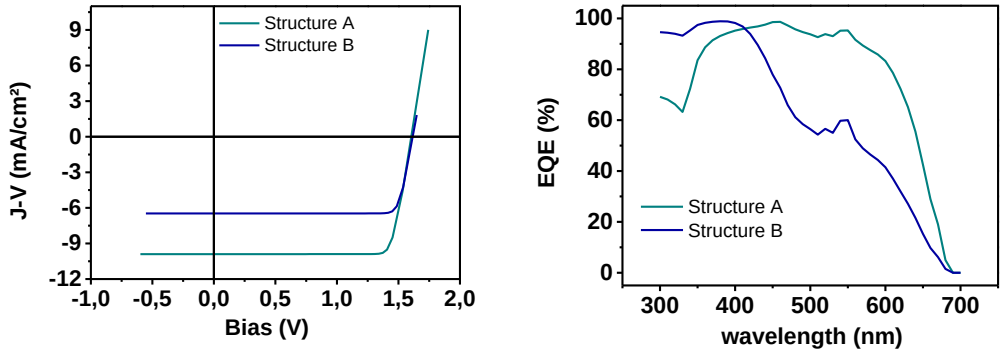

(c) (d)

Figure 3.2.2-1: (a) Band diagram of structure B. (b) Electrical performances for both structures. (c) J-V and (d) EQE associated.

The energy band diagram allows for us to identify some potential problems. For example, the potential barrier at the GaAsPN/GaP-n interface may pose a problem, depending on the electron affinity and the doping value of GaP-n (cf. Sec. 3.2.5).

The comparison of the EQE for the two structures is interesting. One can notice a global EQE lower for B structure because of the non-absorption of part of sun light, especially for the low-energy photons, but a higher value in the U.V range, revealing a loss of electrons generated in p-doped layer.

After having considered the ideal case, we will focus on determining the physical parameters playing a key role in the structure B.

3.2.3 The $\mu\tau$ product and thickness

As will be discussed in Sec. 3.4.2, the $\mu\tau$ product is the key parameter of carrier transport in pin diode, as it governs the drift length. In this section we present results obtained by varying the $\mu\tau$ product from $1.25.10^{-15}$ cm²/V to $1.25.10^{-1}$ cm²/V (cf. Figure 3.2.3-1). The J-V curves illustrate how the electrical performances are affected by a decrease of the $\mu\tau$ product. First the V_{oc} decreases,

followed by the FF revealing the first carrier collection problems, and finally the J_{sc}.

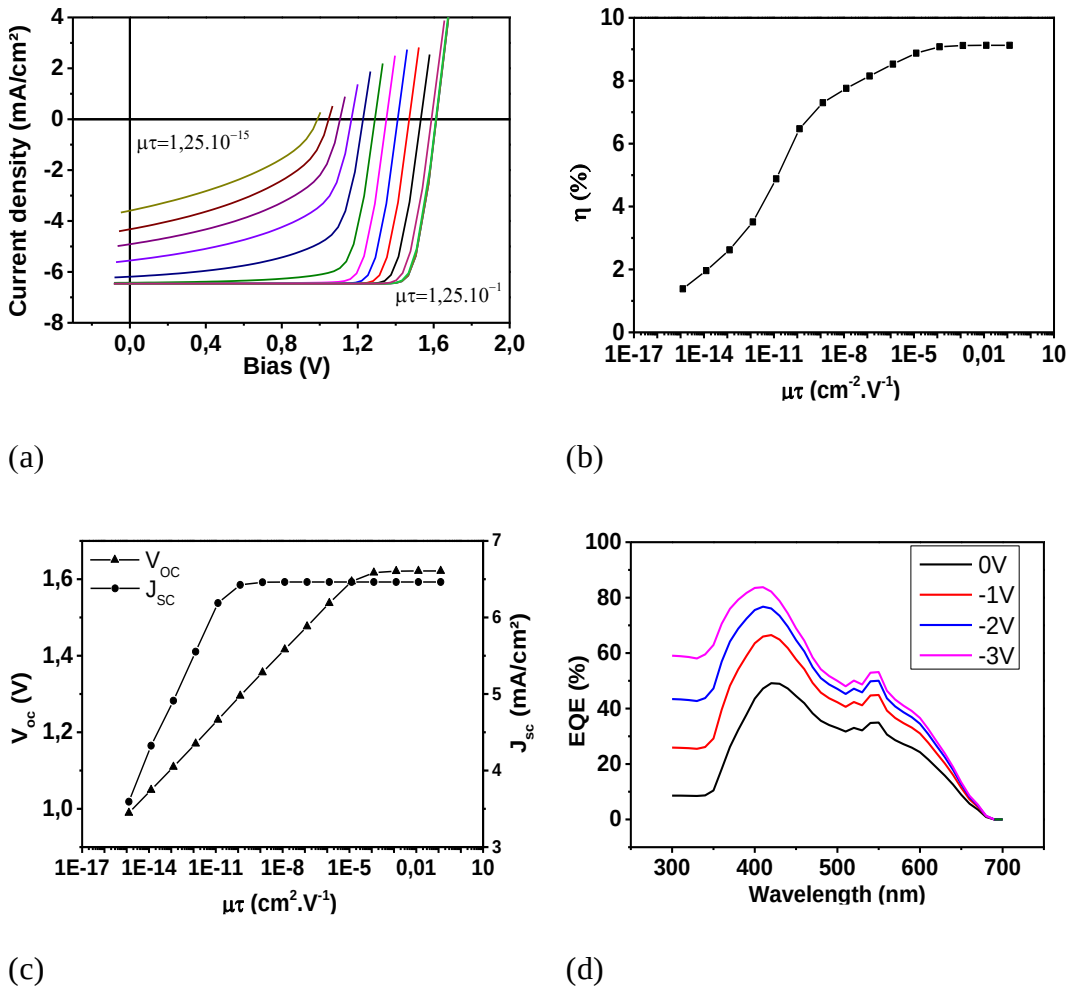

Figure 3.2.3-1: (a) J-V characteristics for each μτ products. (b) Efficiency, (c) J_{sc} and V_{oc} evolution as a function of μτ product. (d) EQE measurement with reverse biases from 0V to -3V for $\mu\tau=1.25.10^{-15}$ cm²/V.

The drift length determines the distance that a carrier can travel. Therefore, for each μτ product value, there is a limiting thickness beyond which the carrier collection efficiency will start decreasing. But a too thin absorber will induce losses by non-absorption (see Eq. (2.2-1.)). For an optimised solar cell design, one has to find a trade-off between the absorption and the carrier collection. In addition, as discussed in section 3.2.2, the higher the thickness is the lower the V_{oc} will be. In

the following simulations, we set this product at $1.25.10^{-5}$ cm²/V, allowing for the probed parameters to impact the collection efficiency.

3.2.4 Electron affinity

The electron affinity, χ, governs the band alignment of the structure at the interfaces. Therefore, recombination at interfaces and photocurrent barrier will depend directly on this value.

We present here the results of simulation with electron affinity varying from 3.8 to 4.4 eV. Defects have been inserted, especially at interfaces. Their exact nature is arbitrary, and is not of importance here. Their only goal is to create a possible recombination path at the interface, in order to apprehend the impact of the potential barrier. Results of simulation are summarised in Figure 3.2.4-1.

The energy band diagram is a very useful tool to interpret the results. By increasing χ, two effects are noted: a creation of a potential barrier and a decrease of the energy gradient across the absorber. The potential barrier does not seem to prevent the carrier collection up to 4.29 eV with our electronic parameters. Beyond this value, J_{sc} sinks dramatically. Besides Figure 3.2.4-1(b) displays the apparition of a kink for χ=4.29eV. As we will see Sect. 3.4.2, this kink is caused by the photocurrent barrier. The evolution of V_{oc} is different: it follows a parabola-like curve increasing from χ=3.8eV to 4.05eV and then decreases. Those degradations of V_{oc} are revealing the increase of recombinations at interfaces, due to the potential barriers (a small barrier also appears for χ, but is never high enough to decrease the current density).

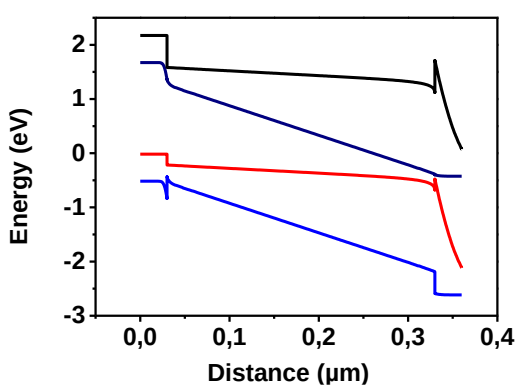

(a)

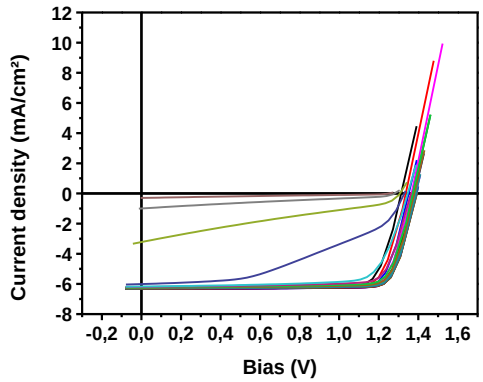

(b)

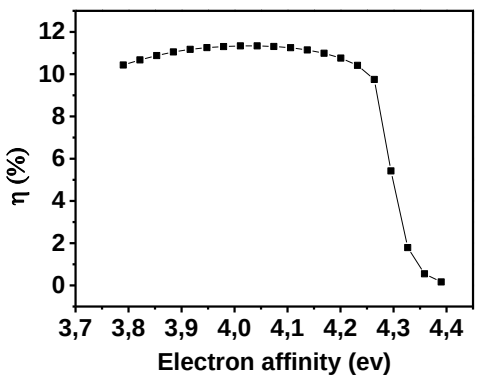

(b)

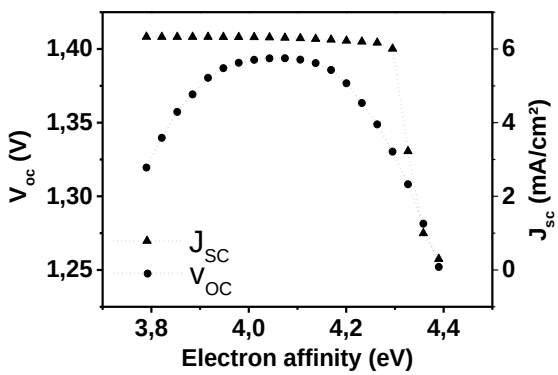

(c)

Figure 3.2.4-1: (a) Energy band diagram for and χ=4.39eV. The curve for χ= 3.8eV is down shifted for clarity. (b) J-V curves. Evolution of η (c) , V_{oc} and J_{sc} (d) with χ.

3.2.5 Doping

In this section, we will discuss on the influence of the doping value on the solar cell behaviour. Doping values of both GaP layers will be considered of course, but also the background doping of the GaAsPN intrinsic layer.

3.2.5.1 P and n doped layers

The influence of the p-doped layer has been investigated. The results are not shown here because it does not limit the efficiency in the range considered (N_a going from 5.10^{17} to 5.10^{19} cm^{-3} following a logarithmic law).

N_d value has on the other hand a huge impact on the performances. We investigate the same variation of N_d. Figure 3.2.5-1 (c) displays the band diagram for the two extreme values. The n-doping value has the same influence on the band diagram than χ: it changes V_{bi} and the thickness of the photocurrent barrier. For $N_d=5.10^{19}$, V_{bi} is high and the barrier is thin, allowing tunneling easily. On the other hand, for $N_d=5.10^{17}$, V_{bi} is decreased and the barrier is larger. The effect on the carrier collection is evidenced Figure 3.2.5-1 (a). J-V curves is affected for $N_d < 1.10^{19}$. At $N_d= 5.10^{18}$, a kink appears in the J-V characteristic revealing collection difficulties. For lower values, the photocurrent plateau is not reached and the discrepancy of J_{sc} is fast.

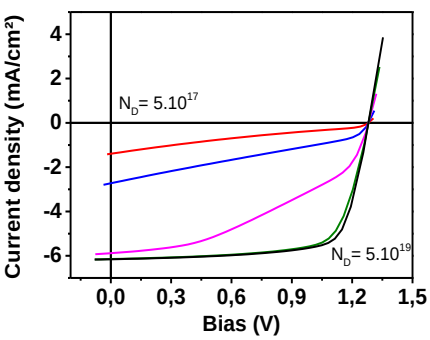

(a)

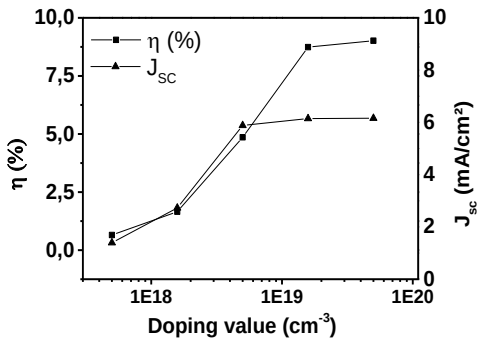

(b)

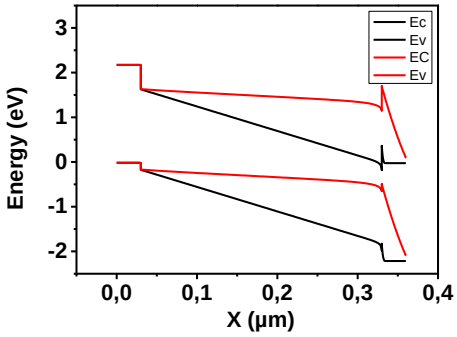

(c)

Figure 3.2.5-1: (a) J-V curves, (b) efficiency and (c) energy band diagram of the pin diode for a donor concentration of 5.10^{17} (red) to 5.10^{19} (black)

3.2.5.2 Background doping

The background doping is an essential parameter in a pin junction. At high background doping value, there is a bias threshold beyond which the i-layer will not be completely depleted, making the pin diode a not optimised pn junction. The system is then dominated by the diffusion, making the collection efficiency decrease. For this simulation, we expect that the background doping will affect the collection efficiency. To enhance this effect, we set the µτ product at $1.25.10^{-13}$ cm^2/V

N-doping

The n background doping is varied from 1.10^{10} to 1.10^{17} cm^{-3}. Results are shown on Figure 3.2.5-2. As expected, the background doping affects the energy band diagram (see Figure 3.2.5-2(a)). It transforms the pin junction in a p-n-n^+ junction. The electric field, located at the p-n interface, is no longer effective over the whole absorber region and the carrier dynamics is dominated by the diffusion. With the short diffusion length in GaAsPN this will degrade the collection efficiency. This is confirmed by the J-V characteristics: the J-V curves show mainly a decrease of

the current for $n_{background}$=1.10^{17} cm^{-3} from 5mA/cm² to 3.5mA/cm². The open-circuit voltage remains constant and the efficiency goes from 4.1% down to 2.8%.

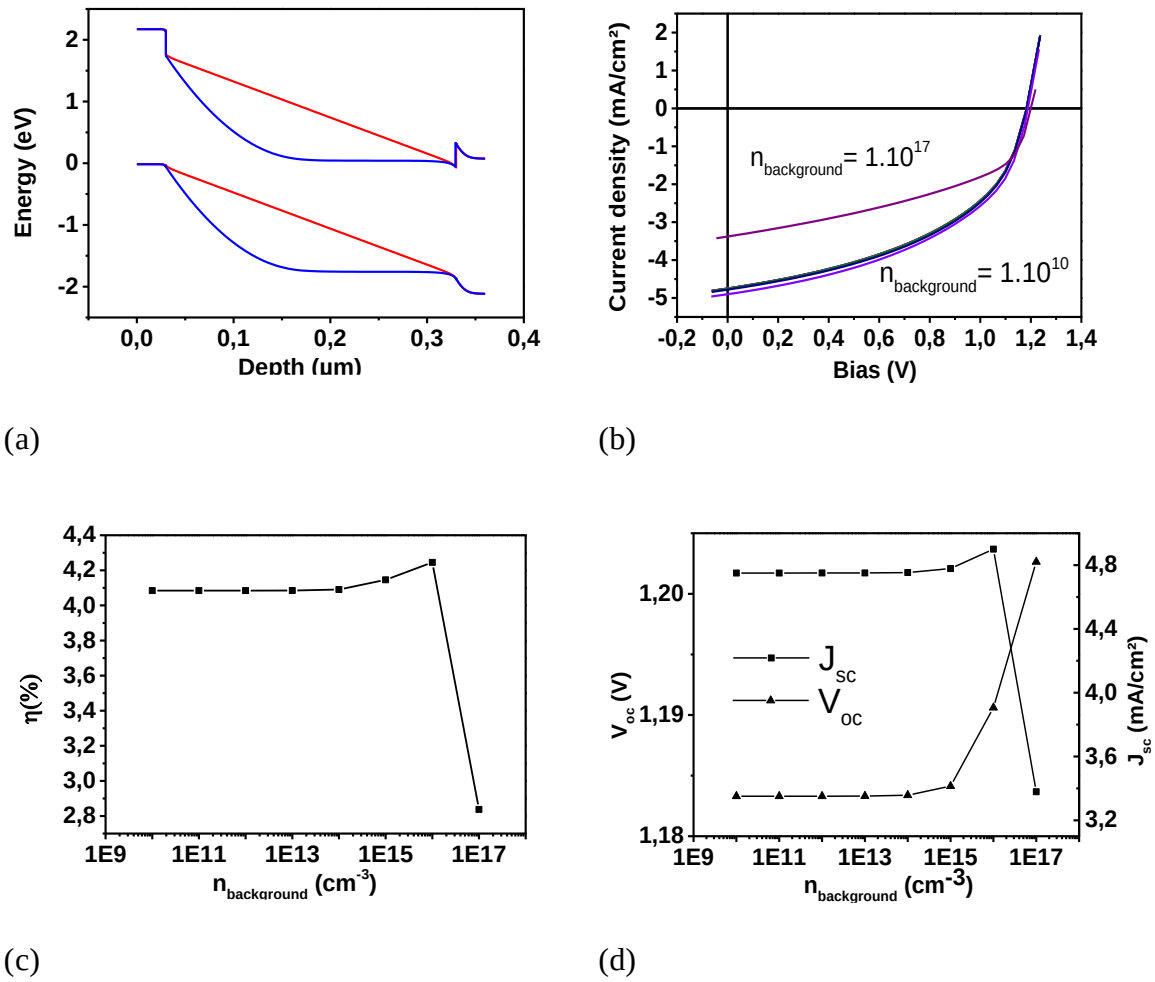

Figure 3.2.5-2: (a) Energy band diagram of the pin diode for a n background doping of 1.10^{10} cm^{-3} (red) and 1.10^{17} cm^{-3} (blue). (b) J-V curves. Evolution of η (c) , V_{oc} and J_{sc} (d) with $n_{background}$.

P-doping

The p background doping is varied from 1.10^{10} to 1.10^{17} cm^{-3}. This time we are dealing with a p^{+}-p-n junction, with an effective junction located at the p-n interface (cf. Figure 3.2.5-3(a)). We note that this case is less favourable than the n-

background doping. Two reasons can be given: more carriers are generated at the top of the device, and the fact that the minority carrier of electrons is set lower than the holes one. Hence, the electron generated at the p^+/p interface are without kinetic energy and are lost before the p/n junction, where they could be accelerated and collected. In the symmetric case, holes generated in the n-doped absorber, less carrier are concerned and as their mobility is higher, less are loss.

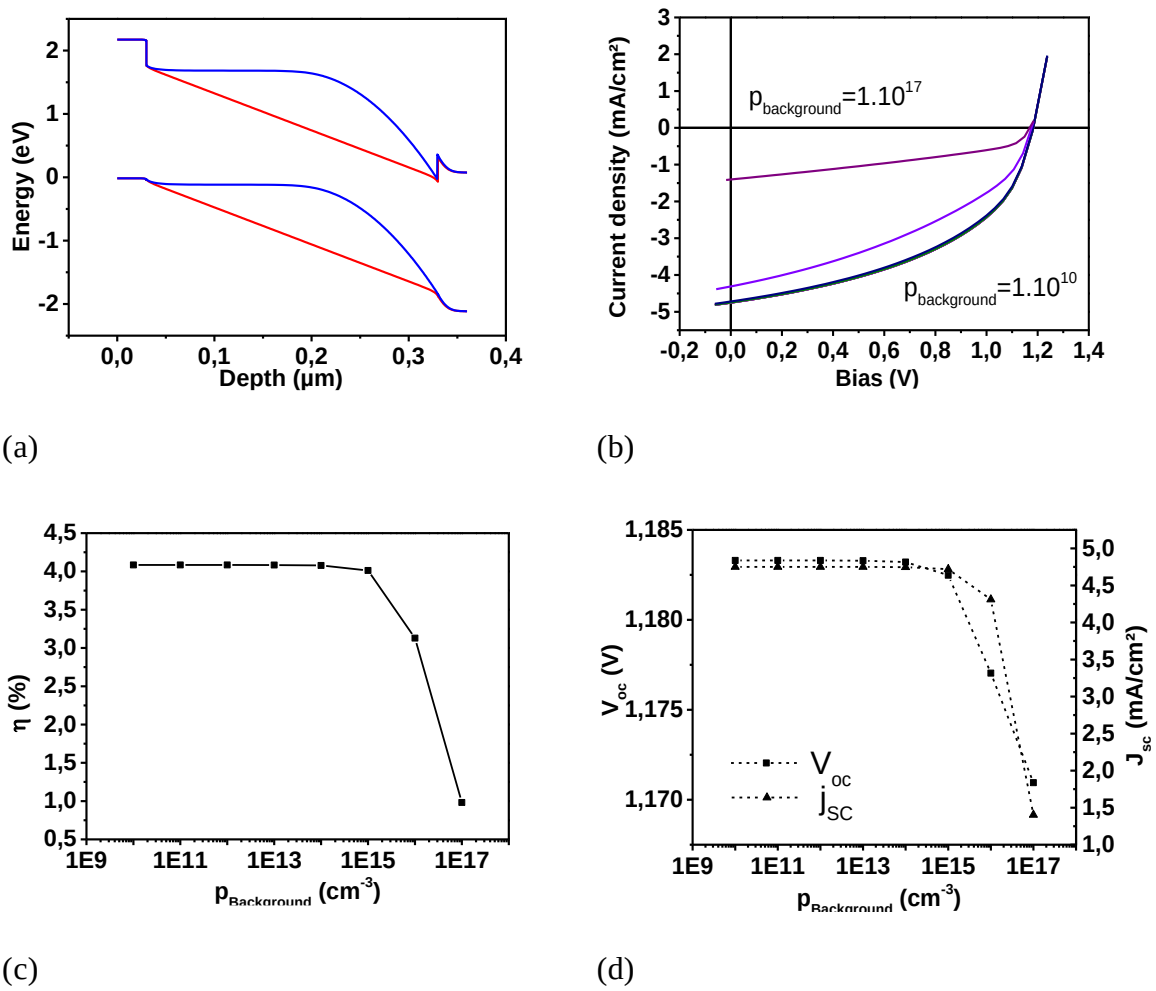

Figure 3.2.5-3: (a) Energy band diagram of the pin diode for a p background doping of 1.10^{10} cm^{-3} (red) and 1.10^{17} cm^{-3} (blue). (b) J-V curves. Evolution of η (c) , V_{oc} and J_{sc} (d) with $p_{background}$.

To summarise, we have seen that the doping value of the GaP-n layer is a critical value because of the potential barrier at the i/n interface. The background doping has also been studied. As it transforms the pin diode into a non-optimised p-n-n^+ or a p^+-p-n diode, the collection efficiency is a decreasing function of the background doping value. Furthermore, in the case of dilute nitride where the electrons mobility is lower than the holes one, a n-type background doping is preferable.

3.3 Optoelectrical characterisation of the GaAsPN top cell

This third section presents the characterisation made on key samples. We will first present the classical PV measurements on the p-i-n junction (I-V and EQE). Then, we will show results on optical characterization technics, mainly based on luminescence methods. This will help to understand the physics of the top cell. Discussions will follow in the next section.

3.3.1 Electrical characterisations

3.3.1.1 EQE measurements

EQE measurements have been performed on all the diodes presented here. Results are plotted in Figure 3.3.1-1.

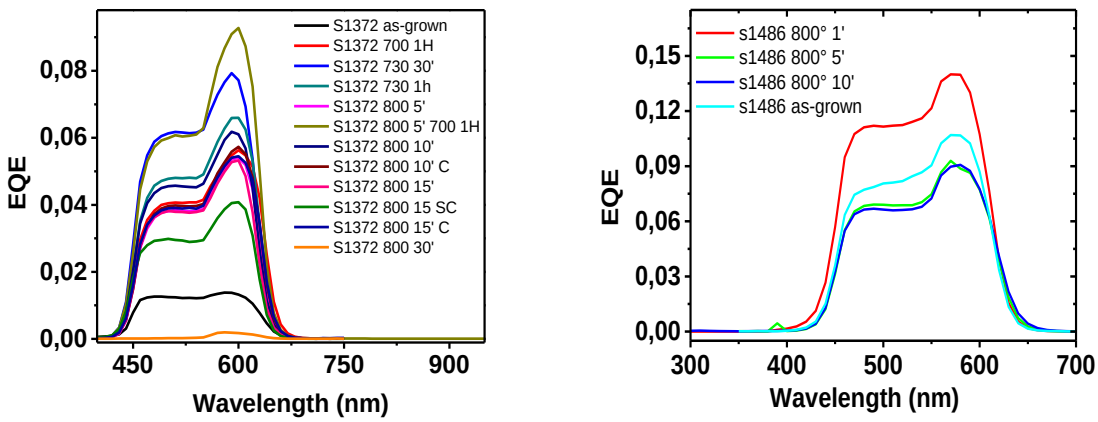

(a) (b)

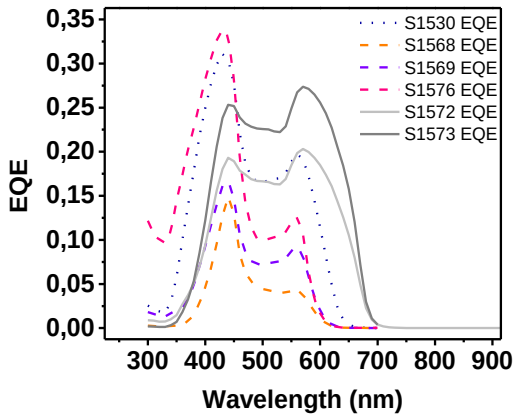

(c)

Figure 3.3.1-1: EQE measurements for (a) s1372 samples, (b) s1486 samples, (c) s1568-s1576 samples.

All the EQE curves show two local maxima, one at around 430nm and the other at around 600nm. This is especially true for the B structure diodes. Those peaks are often related to the two subbands E_+ and E_- presented in the BAC model. We can also notice the large range of EQE performances, even for a same sample.

Figure 3.3.1-1 (a)-(b) present EQE measurements on A type samples (thick GaAsPN), namely S1372 and S1486 for different annealing temperature. One can see that annealing conditions do not change the spectral shape of the EQE. On the contrary, values do change significantly, without any clear trend, even if all the

annealed diodes show an increase of short-circuit current. This is a consequence of the wafer inhomogeneity and will be developed in the discussion.

The type of structure seems to be important. Figure 3.3.1-1(c) displays the EQE of the type B samples. Compare to structure A samples which have a poor carrier collection in the U.V range, structure B samples seem to have a better collection efficiency as expected. This second set of samples is interesting as it presents spectral responses of several alloy compositions, and especially nitrogen contents. Thanks to the EQE(E) curves, we can extract the energy position of the electrical bandgap ranging from 600 to 700nm (2.06 to 1.77eV). As seen in Figure 3.2.4-1, these values are plotted as a function of the N content (dots). It is in good agreement with the calculated values through the BAC theory (lines for E+ and E-). The particular shape of our EQE with peaks might not be a coincidence. This shape has already been reported in literature for GaAsPN alloy, and associated with the two subbands E_+ and E_- [95]. In our case, the high energy peak is centred on the calculated E_+.

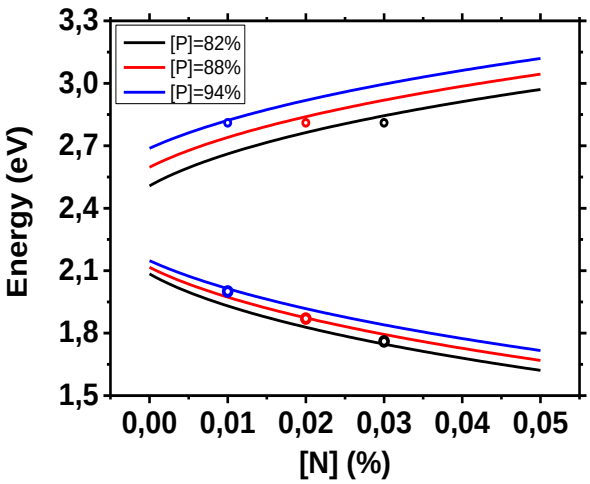

Figure 3.3.1-2: Electrical gap as a function of N content for the three studied compositions (line) and the experiment values extracted from EQE (open circles)

3.3.1.2 J-V curves

After having analysed the EQE measurements, we will focus on the J-V curves in this section.

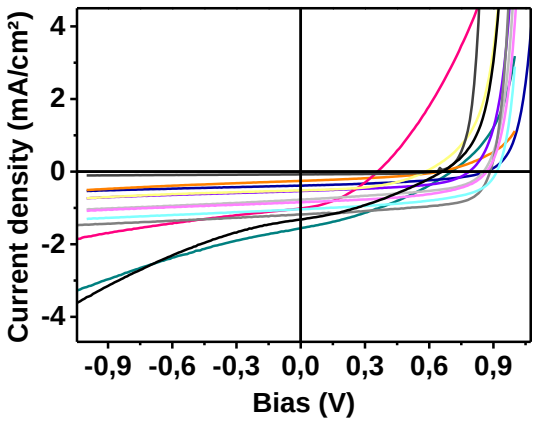

(a)

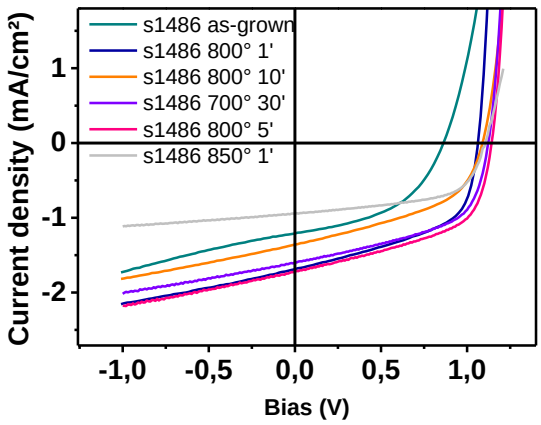

(b)

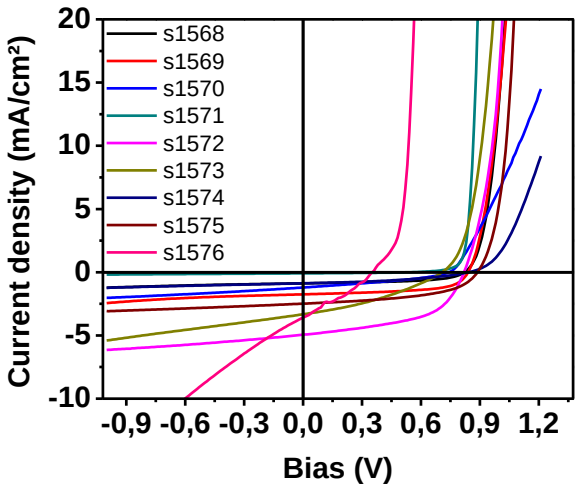

(c)

Figure 3.3.1-3: J-V curves of (a) s1372 sample, (b) s1486 sample, and (c) s1568-s1576 samples

Sample s1372 has poor J_{sc}, with maximum at 1,56 mA.cm^{-2}, and reasonable V_{oc}, around 0,9V for the best cells. Diodes annealed at 730° during 1h and 30 minutes are remarkable: they have higher J_{sc} but lower V_{oc} and especially a higher degradation of the collection efficiency with the forward bias. We can in fact denote the presence of a kink in those J-V curves. Some diodes exhibits a quite stable collection efficiency, but with low J_{sc}, below 1 mA.cm^{-2}. The sample s1486 has globally a higher V_{oc} and J_{sc}. However, the collection efficiency is more affected by the forward voltage. It is notable that our best open-circuit voltage is from this wafer and reach 1,15V. This value has to be put in perspective with the empirical law that determine V_{oc} for good electrical properties material [96] :

$$V_{oc} = \frac{E_g}{q} - 0{,}55 \qquad (3.3\text{-}1.)$$

Here, E_g is around 1,87eV, so a good V_{oc} would be 1,32V. Knowing that in pin diode the V_{oc} is lower [93], the obtained V_{oc} is quite interesting.

Finally, the J-V curves of the rest of the wafers are exhibiting a lot of different behaviours. Those are diodes of structure B. The first thing we can notice is that we could not reach the previous V_{oc} values. However, some diodes have very interesting Jsc values, with a maximum of 4,98mA/cm². Our best efficiency cell was also a B structure cell. The diode from wafer s1576 has an interesting Jsc, but a kink and a collection efficiency rapidly decreasing with the forward bias η(V) makes its efficiency low. Unfortunately, the s1576 diode is shunted. For the rest of the diodes, the electrical behaviours are comparable with the s1372 and s1486 samples.

Here again, the J-V curves have no direct correlation between growth, annealing conditions and electrical properties.

3.3.1.3 Dark J-V characteristics

Dark J-V curves are a powerful tool to characterise solar cells. It allows to determine the series and shunt resistances, to determine the ratio of radiative and non-radiative recombinations, and estimate the defect density.

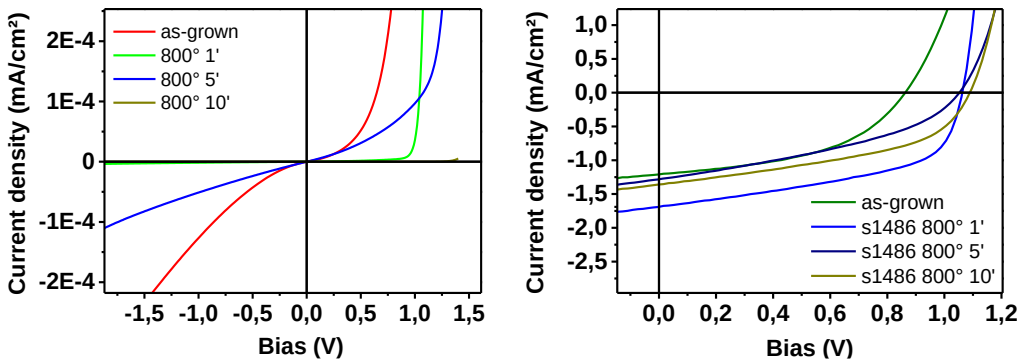

Figure 3.3.1-4: (a) Dark J-V curves for sample s1486 as-grown and annealed at 800° during 1, 5 and 10 minutes. (b) J-V characteristics under one sun illumination

Figure 3.3.1-4 depicts the dark J-V characteristics measured for s1486 diodes. Analysing them, we would expect that at least the as-grown diode and the one annealed during 5' should be shunted. But if we look at the corresponding J-V

curves under AM 1.5, we see that there is no visible effects on the current collection. The as-grown diode suffers however from a low V_{oc}.

The fits attempted on these dark J-V curves have all failed due to an erratic behaviour. The curves cannot be fitted with a two-diode electrical model, and the ideality factor that fits the dark at best are around 4. This kind of behaviour is known to be related to tunneling or hopping.

3.3.2 Optical characterisations

Optical characterisations are useful to probe the material quality, and determine some fundamental quantity as the absorption for instance. In certain cases, luminescence based methods can give insight of the devices properties.

3.3.2.1 Spectrophotometer

We use the spectrophotometer to measure the absorption of the absorbers. Measurements are plotted in Figure 3.3.2-1.

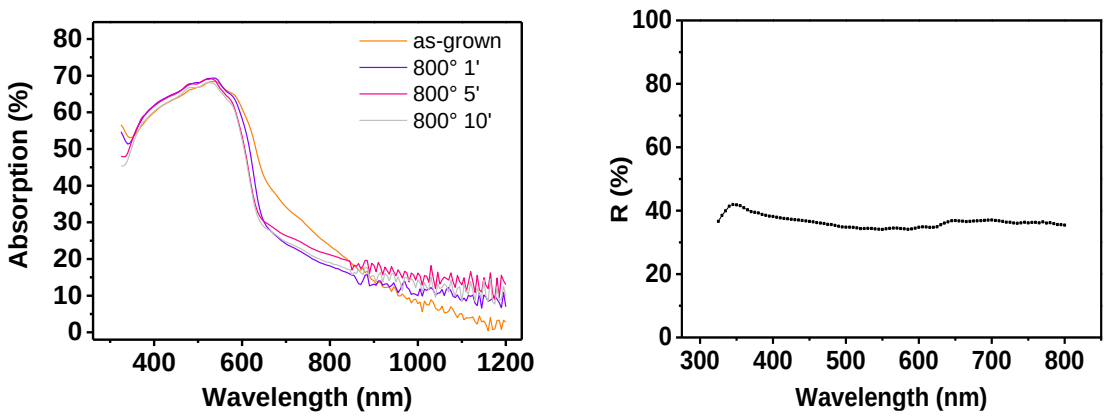

(a) (b)

Figure 3.3.2-1: (a) Absorption of GaAsPN absorber raw and annealed at 800° during 1', 5' and 10'. (b) Reflexion measurement of the GaP window layer.

The annealed absorbers present a clear absorption edge at 645nm (1.92 eV), while the raw one has a soft slope. The absorption measurement exhibits the decrease of the Urbach tail [97], [98] by annealing the material and the crystalline quality

improves with such treatment. As the annealed absorbers have all the same absorption shape can conclude that the variation of the annealing time in our time range has a poor incidence on the Urbach tail decrease.

From these measurements we have also been able to extract the absorption coefficient in those samples. This value is a critical parameter. Indeed, it governs the absorber thickness needed to absorb the sun energy. Therefore, it is a necessary value in numerical simulation and solar cell structure design. The spectrophotometer gives access to reflected, transmitted and absorbed light intensity. Figure 2.1.2-1 describes the spectrophotometer principle.

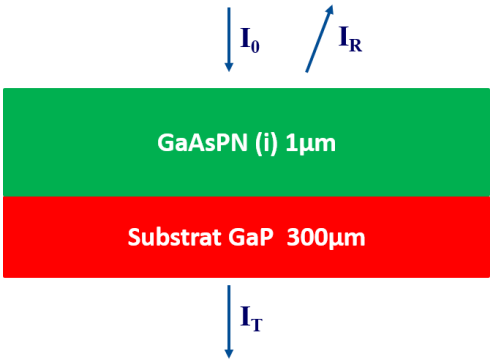

Figure 3.3.2-2: GaAsPN sample used with the spectrophotometre.

I_0 is the incident light intensity, I_R the reflected light intensity and I_T the transmitted one. Neglecting the multiple reflections inside the structure, we can deduce from Beer-Lambert law the absorption coefficient of GaAsPN:

$$I_T = (I_0 - I_R)e^{-\alpha e} = I_0(1 - R)e^{-\alpha e} \qquad (3.3\text{-}2.)$$

Where α is the absorption coefficient of GaAsPN, R the reflection at the front interface, and e the absorber thickness. This formula is only valid between the bandgap energy of the GaAsPN and the GaP, i.e up to 548nm. The hypothesis of weak reflexion at the GaAsPN/GaP interface could seem rough. Literature on dilute nitride indicates that nitrogen incorporation has various effects on refractive

index. For $GaSb_{1-x}N_x$ for example, theoretical study shows that addition a few percent of nitrogen increases the refractive index significantly ($n_{x=0}$=3.5 and $n_{x=0.05}$=4.7). Same effect has been evidenced in GaInAs [99]. Opposite effect has been exhibited for GaAsN [100] and expected for GaPN alloys [101]. In the case of GaPN, very close to GaAsPN, refractive index is constant for the N content up until 5%. The GaAsPN alloys studied in this thesis have low As content (12% maximum) and we expect therefore that nitrogen incorporation does not change refractive indices, making the reflexion coefficient very low at GaAsPN/GaP interface. At the end, we obtain an absorption coefficient very interesting, reaching $2{,}5.10^6$ cm^{-1} at 550nm. Figure 3.3.2-3 displays it with the one measured by Geisz et al, [78].

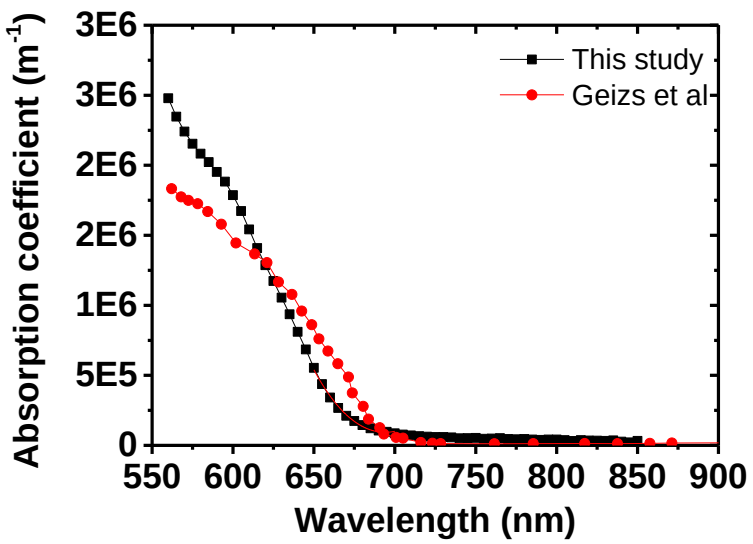

Figure 3.3.2-3: Absorption coefficient measured by spectrophotometre.

With such an absorption coefficient, the total thickness needed to absorb 95% of the accessible sun energy is around 3.9µm, and the potential current density for a 1µm-thick absorber is 10mA/cm², and 6,5mA/cm² for a 300nm-thick absorber, taking into account the reflexion at the front layer.

3.3.2.2 Photoluminescence study

By recording the PL spectra, we want to establish correlations between the luminescence properties and the electrical ones. This correlation would lead to a better understanding of the physical mechanisms occurring in this dilute nitride alloy.

A 532nm laser excitation of 3525 suns (3525 kW/m²) is applied on each diode and absorber at room temperature (RT), and the PL spectra are recorded by a Si CCD.

3.3.2.2.1 Absorber

The photoluminescence spectra are used to understand the carrier population of those absorbers. Results are plotted in Figure 3.3.2-4.

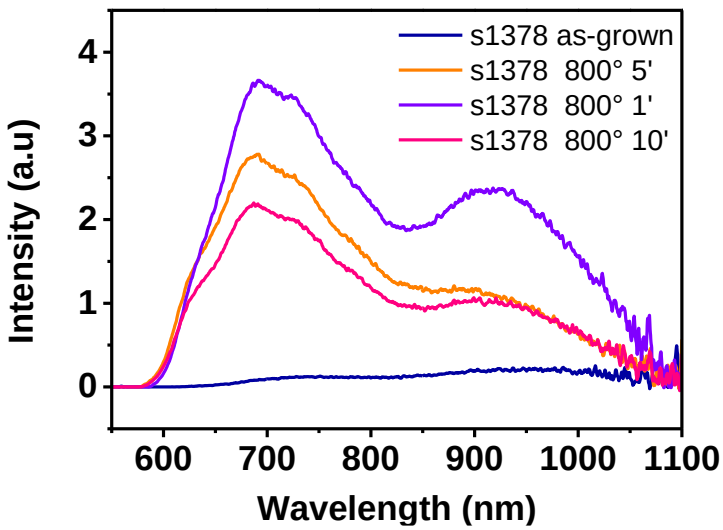

Figure 3.3.2-4: PL spectra of a GaAsPN absorber raw and annealed at 800° during 1, 5 and 10 minutes.

Looking at the spectral variations, we denote two broad peaks, one around 700nm and one around 925nm. The expected bandgap energy being around 700nm, the luminescence spectra is composed in a large part of sub-bandgap luminescence, likely from defects. This kind of broad peak has been noticed in the literature in

GaPN absorber luminescence [102] and more generally in dilute nitride III-V alloys and are related to deep-levels defects and N-induced defects (N-N, N-N_3,…)

The PL spectra show a spectacular PL increase after annealing of about x400. Following the generalized Planck's law, the PL intensity is an exponential function of the quasi Fermi level splitting Δμ, itself a decreasing function of the defect density, we can deduce that annealing reduce the defect density and improve the GaAsPN quality. This would indicate an additional increase of Δμ (maximum achievable voltage) of about 150meV. Although this is valid for most of the PV absorbers, we will see in the discussion, that this conclusion is not necessary true when applied to dilute nitride alloys.

3.3.2.2.2 Diodes

Figure 3.3.2-5 (a) shows PL spectra for sample s1372 under different annealing conditions. We distinct here again the presence of at least two PL peaks: a narrow one at 670 nm and a broad one around 800-850nm. PL spectra of the diodes have therefore some similitude with PL spectra of the absorbers with a slight blue shift. One can also notice that the as-gown sample (yellow curve) does not have the high-energy peak emission, neither has the sample annealed at 800° during 30 minutes. This samples has been damaged during the annealing, resulting in a higher non-radiative recombination rate in the sub-band gap states. The appearance of the high energy peak emission also arises when increasing the excitation power (see Figure 3.3.2-5 (b)).

As the absorption edge of the EQE is around 645nm, we can already notice that most of the radiative transitions are occurring at energy below the electrical gap. This is a proof of a high defect density below the conduction band.

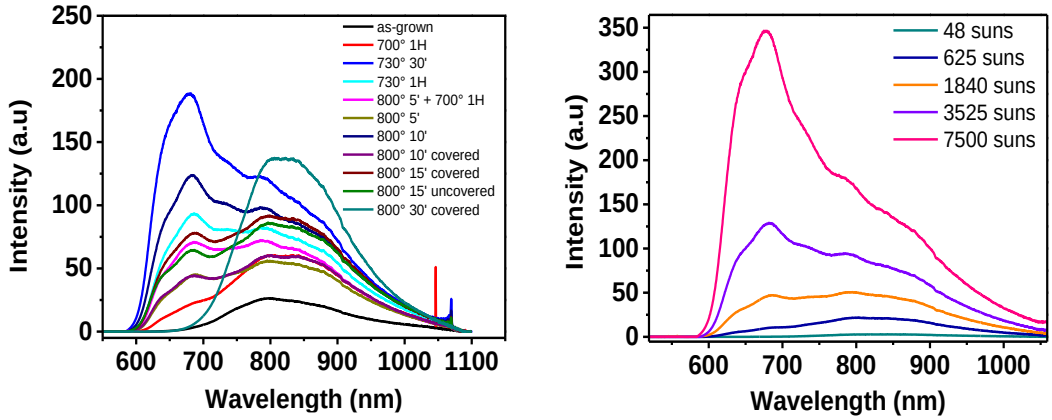

(a) (b)

Figure 3.3.2-5: (a) PL spectra of p-i-n diode s1372 with different annealing under a 3525 suns irradiance. (b) PL spectra of s1372 800° 5' for a 48-7500 suns irradiance range.

The same behaviour is found for the s1486 diodes displayed on Figure 3.3.2-6. Although this sample follows also the A structure (with thick GaAsPN layer), the two PL spectral peak positions seem to be closer and the peaks corresponding to the EQE collection edge is raising at lower irradiance (with an irradiance equivalent of 7 suns).

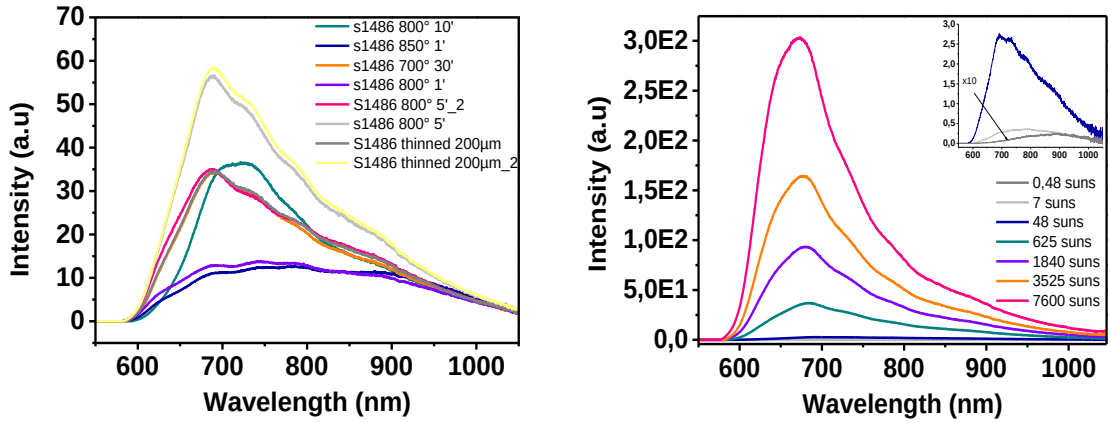

(a) (b)

Figure 3.3.2-6: (a) PL spectra of p-i-n diode s1486 with different annealing under a 3525 suns irradiance. (b) PL spectra of s1486 800° 5' for a 0.48-7500 suns irradiance range. A zoom is displayed for low irradiance in the inset for clarity

At last we present in Figure 3.3.2-7 the PL spectra of the B structure diodes for

different annealing conditions. For all the samples, the subband gap defects luminesce around 850 nm and the electric gap emission vary from 630 to 690nm. Those peaks have however different spectral shape, especially concerning the high energy decay. Unfortunately once again, no direct correlation between PL and electrical properties are found.

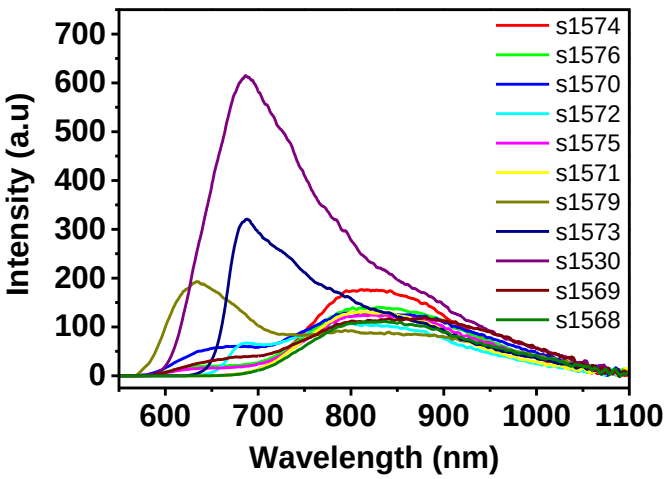

Figure 3.3.2-7: PL spectra of p-i-n B structure diode under a 3525 suns irradiance.

3.3.2.3 Time Resolved Photoluminescence study

Time Resolved Photoluminescence (TRPL) is often used as solar cell compatibility measurement. Indeed, it is commonly assumed in the PV community that a longer lifetime gives higher PV performances. At same excitation levels, a stronger PL signal means indeed a higher radiative efficiency. Nevertheless this assumption is valid for ideal standards bulks, where no localisation of carrier nor shallow defects are present. Shallow defects and localised states are acting as a retention room for electrons: they are captured in the defects and released after a time t, before to recombine, introducing a delay and increasing artificially the radiative time τ_{rad}. The carriers can also recombine radiatively from the defects or states, but in both cases the radiative time is significantly higher than in the CB. Therefore, we will

consider a multi-exponential fit for TRPL measurements on GaAsPN, even if in disordered material, a stretched exponential decay can be observed [77], [103] :

$$I_{PL}(t) = I_{PL,0}\exp\left(\left(-\frac{t}{\tau}\right)^{\beta}\right) \quad (3.3\text{-}3.)$$

β being a dispersion factor. Its meaning has been correlated with the dispersive diffusion of the photogenerated carriers [104], [105]. This diffusion can be caused by hopping between localised states or trapping/detrapping from the localised states to the extended states [103], [106], [107]. However, as the exact physical interpretation of this law is complex, we will here fit the PL decay with a biexponential decay, which is a particular case of the stretched exponential law. Indeed, as we will see above, most of our decays are well fitted with this simpler law.

3.3.2.3.1 Absorber

Time-resolved photoluminescence measurements are performed on all the absorbers. Previous studies on dilute nitride alloy allowed identifying the radiative transition mechanisms [108]–[110]. Here, we used a pulsed laser at 5MHz and the decay time is measured by a TCSPC system. The single photon counting device is a τ-spad with a time resolution of 300ps (See chapter 2).

Results are shown in Figure 3.3.2-8 for the as-grown absorber and for different annealing conditions. The decays we measured are not characteristic of an exponential behaviour, therefore it was difficult to extract characteristic lifetimes. Qualitatively, one can see that the annealing extends the luminescence lifetime.

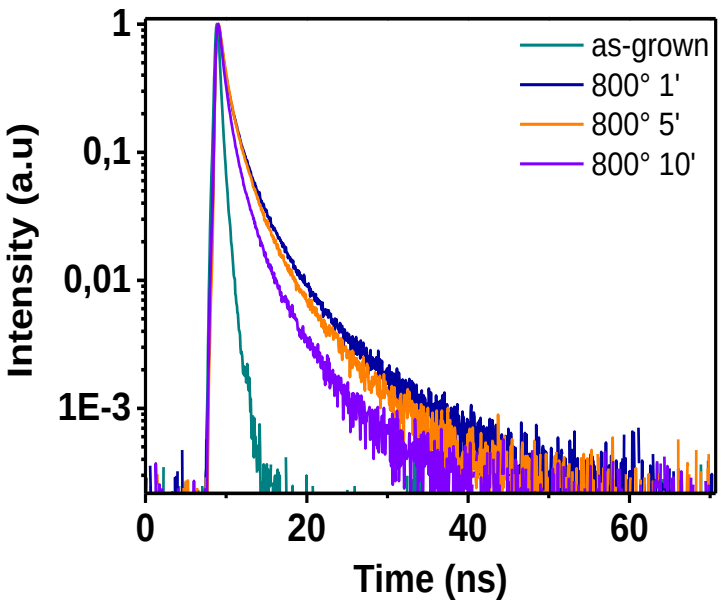

Figure 3.3.2-8: (a) PL decay of s1378 annealed under different conditions.

3.3.2.3.2 Diodes

Same TRPL experiments have been carried out on p-i-n diodes. Results are displayed Figure 3.3.2-9(a) for the sample S1372 with different annealing conditions. For each cases, we fitted the curves with the lower exponential decays as possible.

The as-grown diode is fitted with only one exponential decay, meaning that one mechanism dominates the others. Taking into account the short time extracted, the low-luminescence intensity and a J_{sc} of 0,26mA/cm², the most probable scenario is that the trapping/detrapping in localised states is dominating the radiative recombinations, explaining the low J_{sc}. Besides, the non-radiative recombinations are important, explaining the global short decay and the V_{oc} of 0.6V.

Most of the diodes can be fitted with two exponential decays that would correspond to both radiative time and trapping/detrapping mechanism in the localised states.

Finally, the diode annealed at 730° during 30 minutes need three exponential to be fitted. That reflects a high degree of disorder. Surprisingly, this diode is the one exhibiting the higher J_{sc} with 1.56mA/cm².

Correlations between decays and electrical properties are quite complex. Figure 3.3.2-9(b) shows for example the absence of simple correlations between the J_{sc} and the fitted characteristic decay times. A statistical analysis of the annealing effect on TRPL decay is required to see whether the duration or the temperature play the important role. No trends are observed for the correlation of the decay with any electrical parameter (Voc, Jsc, FF, η).

Samples	Jsc	V oc	A1	tau1	A2	tau2	A3	tau3
730°30'	1,56	0,7	7,20172E6	0,438	47806,24697	1,53195	2011,1883	5,27662
700°1H	0,78	0,85	6,27574E9	0,19395	--	--	--	--
730°1H	1,33	0,66	5,45025E7	0,32469	16791,42154	1,4318	--	--
800°15'	1,02	0,36	1,07395E8	0,29982	22326,54003	1,32004	--	--
800°10'	1,17	0,89	6,2236E7	0,32109	30912,37262	1,41081	--	--
800°5'	1,04	0,92	1,77476E9	0,22082	7744,22909	1,07829	--	--
800°30'couvred	0,08	0,62	8,44537E8	0,23887	29527,99287	0,81685	--	--
800°15' uncovered	0,39	0,87	1,41414E8	0,29044	10919,88776	1,38687	--	--
800°15'couvered	0,53	0,79	7,06356E8	0,2422	27932,07923	0,98688	--	--

800°5'+700°1 H	0,84	0,87	2,53699E 8	0,2708 7	63874,606 26	0,8809 3	--	--
800° 10' couvert	0,52	0,58	1,246E9	0,2298 9	19953,109 06	0,8525 6	--	--
As-grown	0,26	0,65	7,97758E 9	0,1870 3	--	--	--	--

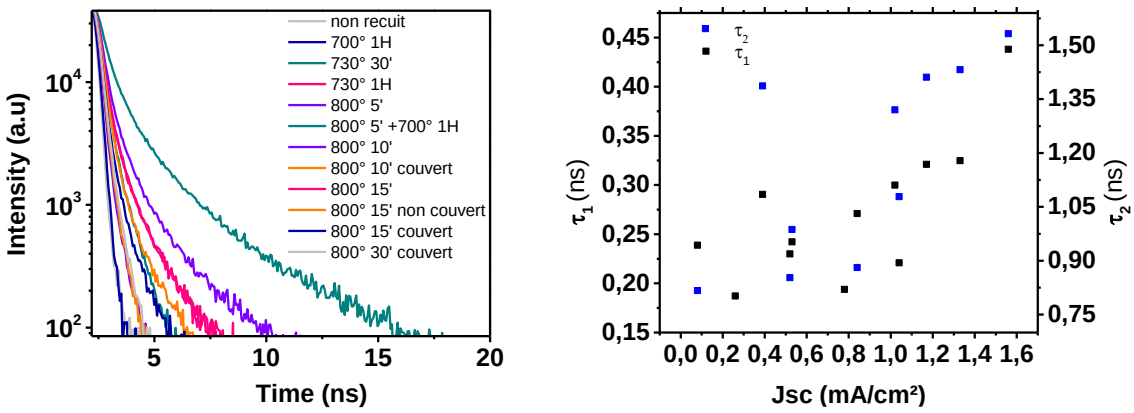

(a) (b)

Figure 3.3.2-9: (a) PL decay measured for several annealing conditions. (b) Values of characteristic time for the peak @ 670nm and 780nm reported as a function of the open-circuit voltage

3.4 Discussions

The objective of this fourth section is to find a correlation between the different input parameters (growth conditions, annealing conditions), the opto-electrical properties measured (PL, TRPL) and the electrical performances we have just presented. We will here discuss the spatial heterogeneity, the carrier collection issues, the annealing effects and the luminescence properties in order to correlate all these parameters to the PV performances.

3.4.1 Spatial heterogeneity

In the previous section, no direct links with the PV performances could be established. The fundamental reason could be that we did not take into account the original location of the samples on the wafers. Indeed, we have observed spatial heterogeneities in the optical properties at various scales on the wafer. Samples from the same wafer and annealed at the same conditions was found to have very different electrical behaviour (Figure 3.4.1-1(a)). Besides at a millimetre scale, EQE from different part of a same diode can have different values (Figure 3.4.1-1(b)). And finally even at a micrometre scale, PL measurement is heterogeneous. This observation was also made on InGaAsN by Miguel-Sanchez et al for the PL measurement [111].

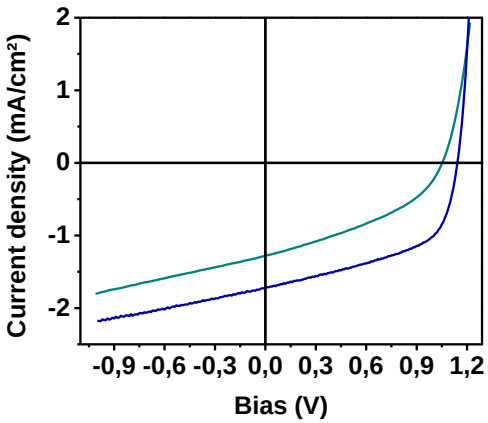

(a)

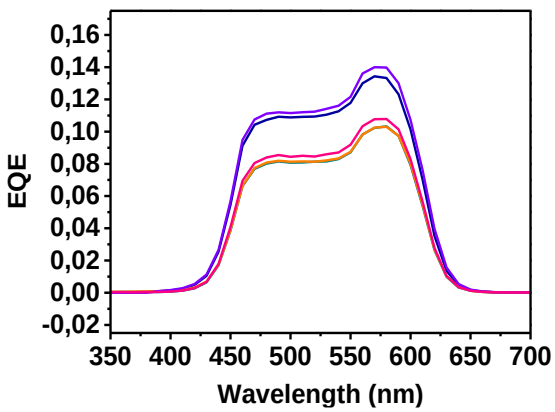

(b)

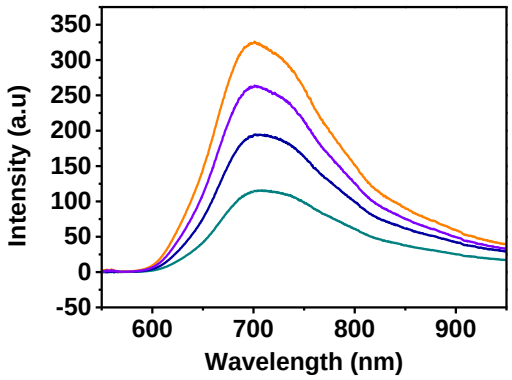

(c)

Figure 3.4.1-1: (a) J-V curves for two s1486 diodes for the same annealing conditions. (b) EQE measurement with a 3mm diameter spot on a 0,630cm² s1486 diode (c) PL measurements on 4 different locations of a 0.625 cm² sample

In order to obtain reliable conclusions about the growth and annealing conditions, it is therefore necessary to work in a statistical way. It is needed to analyse a set of 5 to 10 diodes always taken from the same wafer area. This process is crucial but demands a lot of wafer to be grown. Such a study could not be done during my thesis. In addition to make conclusions about growth and annealing conditions difficult, this kind of heterogeneity can have incidence on the electrical performances. This will be discussed in the open-circuit voltage section (cf. Sect. 3.4.5).

3.4.2 Low collection efficiency

When looking at the I-V characteristics one can identify a slope around the short circuit condition. As this slope is not related to the dark J-V characteristic, it cannot be related to shunt behaviour. It is actually due to carrier collection problems.

As we will see in the following, in pin diode even more than in pn junction, this collection function is electrical bias dependant.

One can also consider the lateral collection efficiency and the impact of the top layer doping (sheet resistance effect). Light beam induced current has been carried out (not shown here) and no lateral drop of current with the distance to the electrical contact were seen.

Three possibilities could explain the weak collection efficiency. The first one and most expected for dilute nitride alloy is a poor minority-carrier drift length. In a pn junction, the minority carrier diffusion length is a highly critical property for classical solar cells and their design. Indeed it rules the total length the minority carriers can travel through before they recombine. It is related to both carrier mobility and carrier lifetime by:

$$L_{n,p} = \sqrt{\frac{kT\mu_{n,p}\tau_{n,p}}{q}} \tag{3.4-1.}$$

In a pin junction on the other hand, the key property is the drift length. This physical value gives the length a minority carrier can drift before to recombine, and can be related to the diffusion length:

$$L_{drift_{n,p}} = \mu_{n,p}\tau_{n,p}E = \frac{q}{kT}{L_{n,p}}^2 E \tag{3.4-2.}$$

In both cases, the μτ product is a key property. Minority carrier diffusion length is very difficult to measure directly. Most of the time it is measured by EBIC [112]–[114], or fitted on EQE measurement thanks to Gartner model [115]. However, in our case, EBIC measurement was not applicable since the electron beam interaction region was as thick as the absorber thickness. The Gartner model, which already suffers from a significant uncertainty for low-quality semiconductor, is for dilute nitride highly uncertain because diffusion length is lower than the depletion region [78]. Paget et al have also proposed a model to determine the diffusion

length by imaging the spatial luminescence decay [116]. Unfortunately, after having at least some luminescent enough GaAsPN absorber, we were unable to measure their luminescence decay. Indeed, our minority carrier diffusion lengths are likely to be below 1µm, and the spatial resolution of the optical microscope we used of 2µm was not enough. The easiest way to get it would have been to determine both minority-carrier mobility and lifetime. But here again, because of its too weak value, the carrier mobility has not been determined successfully. Concerning carrier lifetime, taking into account the complexity of the spectra, the density and diversity of defects, and the different mechanisms involved, it is very difficult to conclude about it.

Regarding the electric field, in the hypothesis where it is constant through the absorber layer, we can calculate it knowing the built-in voltage. If we know the background doping, we even can determine its decreasing as a function of the depth. But in reality, the interface recombination, and the various defects inside the absorber makes impossible accurate determination.

The drift length is expected to be small in our system, impacting many optoelectrical characteristics. Whatsoever its true value, conclusions can be drawn. The comparison between EQE from structure A and B for the same growth and annealing conditions (Figure 3.4.2-1 (a)) allow us to identify limiting carriers in our structure. Indeed by reducing the absorber layer thickness in the B structure, we have increased the collection efficiency of short-wavelength photon induced carriers. Those photons are absorbed near the surface and the induced electrons have to get through the entire device thickness before to be collected. In the A structure, this thickness was too high and most of the electrons were lost. This observation emphasises that electrons are limiting the total current in the structure. This conclusion was foreseeable, as Nitrogen atoms interact mainly with the conduction band and create shallow localized states. Those states are acting as traps for electrons in the conduction band, and therefore strongly reduce their mobility.

This hypothesis is confirmed by EQE measurement of the doped absorber sample displayed in Figure 3.4.2-1(b). The samples, specifically designed in this purpose, follow structure A with a doping of the absorber layer of 1.10^{17} cm^{-3}. The p-doped absorber structure has the same spectral response EQE(E) shape as the non-doped samples. Since the p-doping improves the holes diffusion length, we can deduce that holes was not the limiting carrier. The n-doped absorber structure on the other hand exhibits a better collection in the UV range, but a lower one near the band gap. In addition, it is worth noting that this conclusion tends to prove that the absorber was non-intentionally p-doped. This was in fact a debate since III-V dilute nitride semiconductors have been predicted p-doped as-grown by Zhang [117], even if annealing could change this nature.

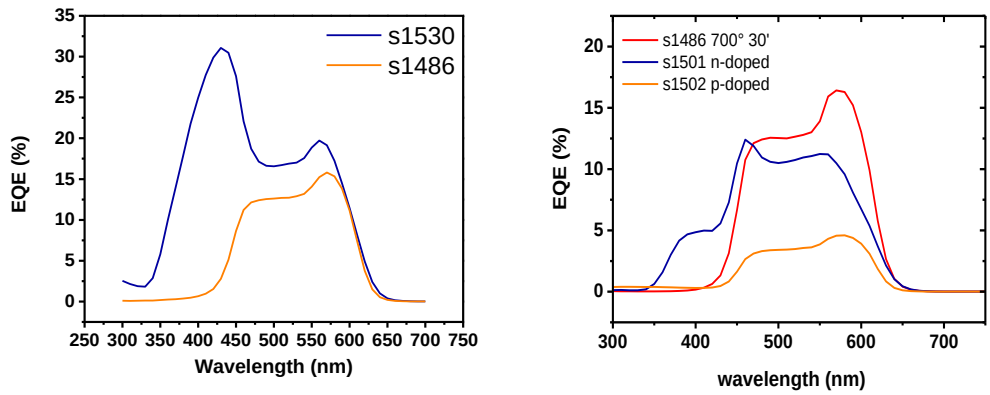

(a) (b)

Figure 3.4.2-1: (a) EQE of s1486 and s1530 samples and (b) EQE of s1486, s1501 and s1502

With the electrons being the limiting carriers, a simple way to increase the J_{sc} would be to inverse the structure to obtain a nip diode.

Another origin of a poor collection efficiency is a presence of a barrier for photocurrent. These barriers emerges from energy discontinuities at interfaces. Such a barrier was shown on numerical simulations (cf. Figure 3.2.2-1(a)), where the i/n interface exhibits a positive ΔE_c. Indeed, due to a positive conduction band

offset, electrons are accumulating at the interface and recombine either at the interface or in the absorber after having been pushed back due to the inversion of dEf_n sign. These barriers can be considered as an electronic element in serial connection with the main diode. Therefore, the total current of the device will be limited by their current, which can be described by the thermionic emission. The thermionic current saturation has been modelled by Richardson [118]:

$$J_{TE} \cong \frac{1}{4} N_c q v_c exp\left(-\frac{\Delta E_c}{kT}\right) \qquad (3.4\text{-}3.)$$

The current across the barrier is calculated as the current from GaAsPN to n-GaP layer minus the current from n-GaP layer to GaAsPN absorber:

$$J_{barrier} = J_{TE,GaAsPN \rightarrow n-GaP} - J_{TE,n-GaP \rightarrow GaAsPN} \qquad (3.4\text{-}4.)$$

$$J_{barrier} = \frac{1}{4} q v_{n,p} \left[\frac{N_{GaAsPN}}{N_{GaP}}\left(-\frac{E_{n,GaAsPN\ z=0}}{kT}\right)\left(\frac{exp(\Delta E_{F_n})}{kT} - 1\right)\right] \qquad (3.4\text{-}5.)$$

where $E_{n,GaAsPN\ z=0} = E_{c,GaAsPN} - E_{F_n}$ for the GaAsPN a the interface, and ΔEf_n is the difference of the QFL between the GaAsPN and the GaP-n layer.

As the electron concentration decreases with the forward bias, the current across the barrier decreases, so does the total current of the diode. For some cases those barriers give birth to kinks, phenomenon that is present for few diodes (s1576 for example). A possible stigma of such a barrier is a better collection in low concentration working conditions. This is the case for some of our diodes, for which the current calculated from EQE measurement is higher than the one from J-V curve (for instance s1573). We have seen in Sec.3.2 that in order to avoid this photocurrent barrier, we can work on the n-GaP layer doping value, or on the electron affinity of either the absorber or the n-doped layer. This can be done by

replacing the n-GaP layer by an n-AlGaP layer which has an electron affinity of 3.98eV. Furthermore, the higher band gap energy of AlGaP (2.38eV for $Al_{0.5}GaP$) would result in a better passivation of the interface. This will be tested in the next few months.

The last possibility is a high recombination rate at an interface. In fact, interfaces between the absorber and the doped region may exhibit a large amount of interface states. This is especially the case when the interface bandgap is smaller than the bandgap of any material involved in the interface. The interface bandgap is defined as $E_{g,IF} = E_{c,min} - E_{v,max}$. With our modelisation of the band offset, this case is present at the p/i interface. This loss mechanism is very sensitive with the electric field. Indeed, the higher the electric field is the lower the recombination at interface will be.

3.4.3 Annealing effect

Thermal annealing has been extensively investigated as a necessary step to improve the crystalline quality of dilute nitride alloys. This annealing process allows migration of atoms and eliminates some of the various defects which appear in the material during the growth. For instance, intrinsic point defects have been identified in GaInNAs and GaPN as As_{Ga} antisites, N interstitials, and Ga vacancies. In consequences, annealing of dilute nitride has shown several effects on the opto-electrical properties. In most cases, annealing of dilute nitride samples leads to a strong enhancement of the luminescence intensity, a narrowing of the FWHM, as well as an increase of minority carrier mobility and lifetime [111], [119], [120]. It also leads to shift of the PL spectrum, which can be explained by a defect-assisted interdiffusion process such as nitrogen migration from interstitial to substitutional site, enabling an electronic bandstructure modification. The magnitude of these effects depends largely on annealing parameters (time, temperature and atmosphere), and on the alloy composition [7]–[10]. In this section we will study the impact of such process on the GaAsPN absorbers and pin diode on the opto-electrical properties. All the annealing

experiments in this study have been performed under a forming gas atmosphere using a JIPELEC JetFirst rapid thermal annealer (RTA).

As annealing is known to heal defects, we were expecting that its main effect would be to increase open-circuit voltage. Nonetheless the experimental results show that it is the short-circuit current that is more affected: every annealed diodes see their J_{sc} significantly increase after annealing treatment. As the absorption was not increased (cf. Figure 3.3.2-1), the carrier collection increases. Since the carrier collection was poor mainly because of the localization of nitrogen-induced states, annealing seems to reduce the influence of localized states. This was also been found in literature [123].

3.4.4 Luminescence properties and statistical study

Although it is trivial in silicon or well-handled III-V, the luminescence physics is subject to certain hypothesis in thin films, and we will see that it is very difficult in dilute nitride to satisfy them.

PL spectra of dilute nitride are very complex. We denote in our diodes a lot of small peaks. Pl spectra of diodes from s1372 wafer are illustrating this fact well. Although no deep PL study has been realised on GaAsPN samples, in the best of my knowledge, some exist for other III-V dilute nitride compounds, GaAsN, InGaAsN and GaPN especially. N-related bound states and N clusters are identified as responsible for sub-bandgap narrow peaks emission [108], [124]–[128] (see Figure 3.4.1-1(b)). Luminescence contribution from these states are well separated at low-temperature PL, but by increasing the temperature the peaks become broader and are all merged together. This is probably what we see in our spectra (cf. Figure 3.3.2-5(a)). Taking this into account, we can conclude that only the highest energy peak is taking part in the current collection. From this analysis we can predict that in order to have a good solar cell, the low-energy peak should be

low and the peak corresponding to the electrical peak should be high. This is confirmed in Figure 3.4.4-1(b), where the current density is featured as a function of θ, the ratio of the PL signal at 670nm and at 780nm: the current density is linear with this ratio.

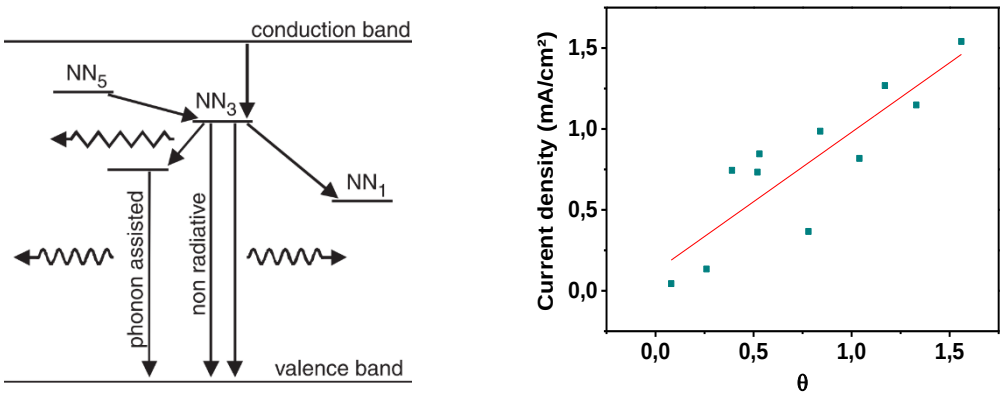

(a) (b)

Figure 3.4.4-1 : (a) Illustration of the N-induced localised states in dilute Nitride (here GaPN). From [128] (b) Current density as a function of θ.

In order to understand the behaviour of those two peaks, the irradiance study offers an interesting insight. Figure 3.4.4-2 shows the evolution of the normalised spectra when increasing the irradiance. It is found that at low irradiance, the PL emission is dominated by low-energy peak. With the increase of the irradiance, this peak emission is significantly blue-shifted, evidencing a localized-state saturation, as it has already been seen on other dilute nitride [110], [129]. When the excitation power further increases, the high-energy peak comes into sight and becomes dominant. The high energy peak is lightly blueshifted with the power-excitation, but its intensity increases fast. This is a typical behaviour of delocalised states, in opposition of the localised states from lower-energy peak which saturates.

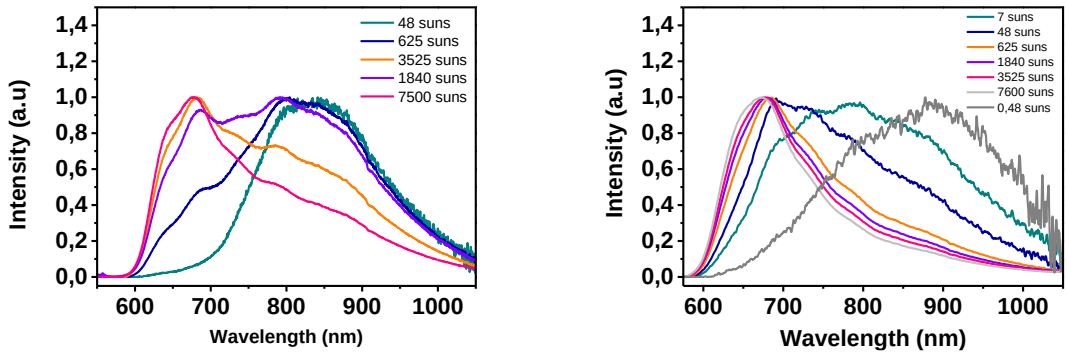

(a) (b)

Figure 3.4.4-2: (a),(b) normalized PL spectra of s1372 and s1486 for several irradiances

Evolution of θ with the increase of the excitation regime is interesting. Figure 3.4.4-3 compares this ratio for s1372 and s1486 diode. For both curves the ratio begins around 0 and increases with the irradiance. Inversion occurs around 2100 suns for the s1372 diode and around 20 suns for the s1486 diode.

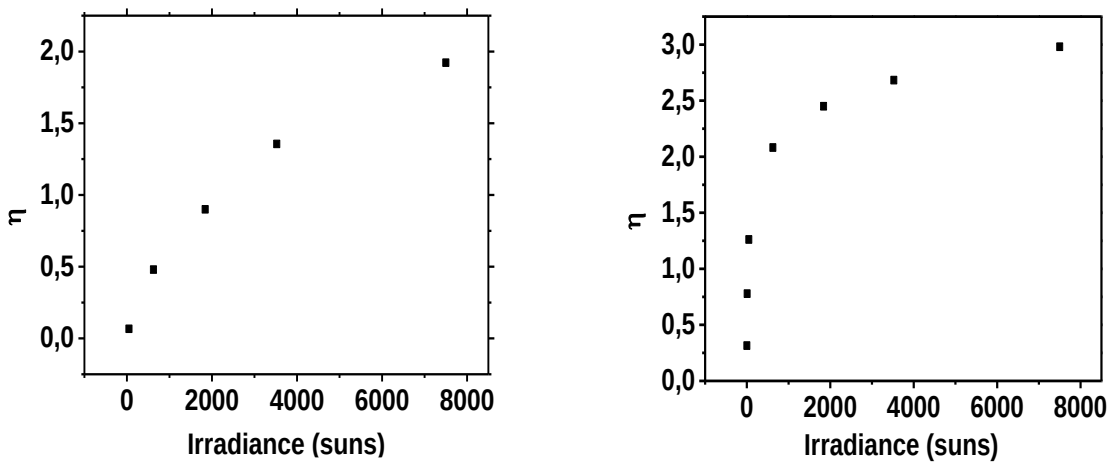

(a) (b)

Figure 3.4.4-3: (a) Irradiance dependence of PL signal for the sample s1372 annealed at 800° during 10'. (b) Evolution of η as a function of irradiance for the S1486 diode.

As the increase of the ratio is the evidence of localised defects saturation, the comparison highlights the much lower localised states density of the s1486 diode.

PL spectra are used to determine the open-circuit voltage [28]. Indeed, as pointed out in Eq. (1.1-7.), the PL intensity is related to the chemical potential which is equal to the voltage across the diode. Therefore in a standard semiconductor, the higher the PL intensity is, the higher V_{oc} will be. Figure 3.4.4-4(b) reports the value of the PL spectra of s1372 samples at 670 and 780nm and the corresponding open-circuit voltages. There is no correlation between those physical values whatever the wavelength considered.

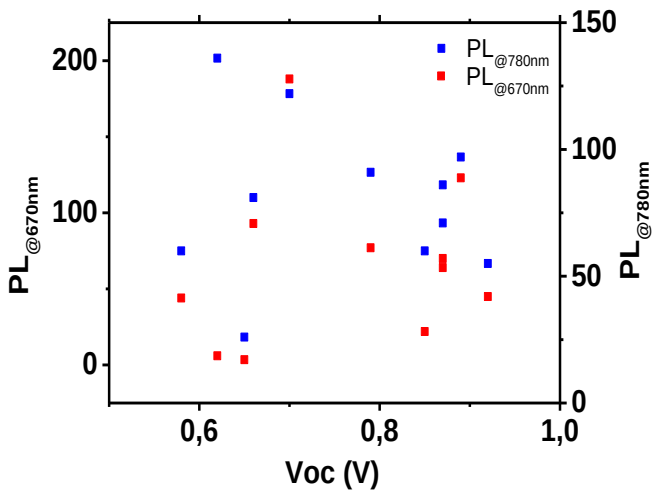

Figure 3.4.4-4: Values of PL for the peak @ 670nm and 780nm reported as a function of the open-circuit voltage.

This unusual behaviour of open-circuit voltage reveals malfunctions in the device. We will analyse them in the next section

3.4.5 Open-circuit voltage

Even if the open-circuit voltages are interesting, from the previous observation, we can identify problems that prevent V_{oc} to be higher. Indeed, we saw that

recombinations at interface are likely present and decrease the voltage. Besides, the spatial inhomogeneity is also a source of voltage loss. A solar cell can be represented as several diodes associated in derivation (cf. Figure 3.4.5-1).

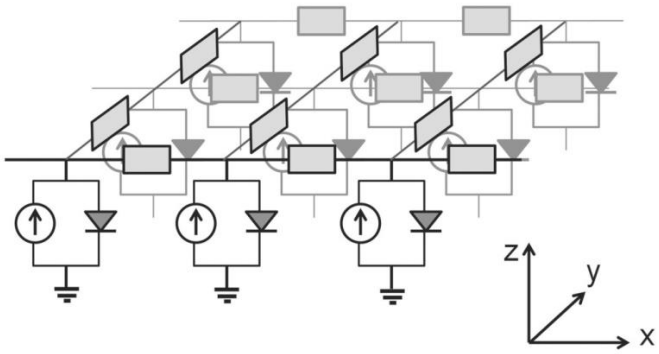

Figure 3.4.5-1: Network model of the solar cell. Each node consists of the parallel combination of a current source and a diode, which is a generic element describing the local dark current-voltage characteristics. The nodes are connected via resistors (gray rectangles). This figure is reproduced from [130]

Therefore, since the material is heterogeneous even at a micrometre scale, the total voltage across the device will be the lowest of the different diodes.

In addition, despite a higher $J_{sc,}$ structure B diodes have lower V_{oc} than structure A ones. This is a sign of a significant recombination rate, either at an interface or at the surface. Indeed, for the same recombination rate of any of those mechanisms, the V_{oc} will be more affected if the absorber is thin. We are currently trying to achieve a surface passivation thank to a polyphospazene like film [131], [132].

3.4.6 Analyse of the best cell

In the light of the previous analysis, revealing the diversity of malfunctions present in our cells, we will here analyse our best cell. Figure 3.4.6-1 depicts the J-V and EQE measurements.

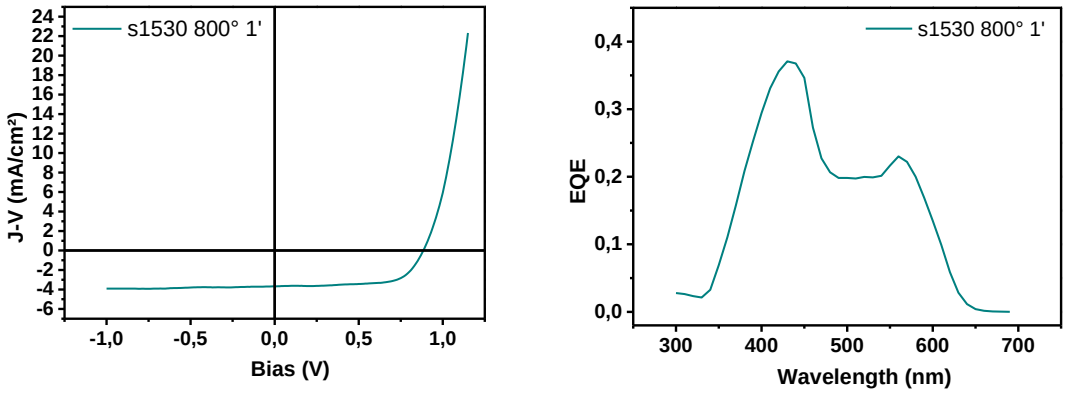

(a) (b)

Figure 3.4.6-1: (a) J-V curve of s1530 sample annealed at 800° during 1'. (B) EQE of the same sample

The J-V characteristic exhibits an efficiency of 2.25%. The J_{sc} of 3.5 mA/cm² and the V_{oc} of 880mV are not the best, but the collection efficiency is not dependent of the bias with a fill factor of 72%. This has to be compared to the theoretical ideal value for a pin junction of 80% [93]. To estimate the collection efficiency, we have plotted in Figure 3.4.6-2 the evolution of the EQE measurement with the increase backward electrical bias. The bias varies between 0V and –1.5V.

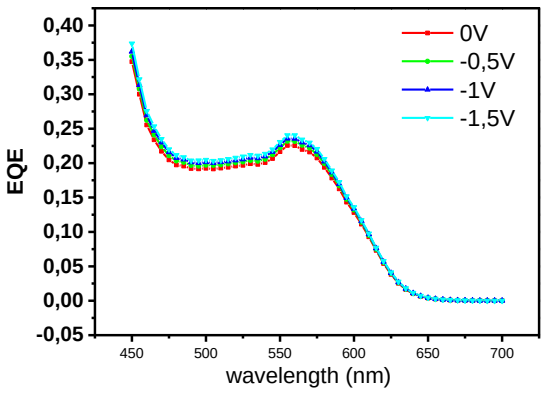

Figure 3.4.6-2: EQE for s1530 800° 1' sample with several inverse electrical biases applied. No improvement is seen with the increased electric field inside the structure.

With a reverse electrical bias all the loss mechanisms should be attenuated. As we saw earlier (Eq.(3.4-2.)), by applying an inverse bias, the electric field increases across the absorber and the drift lengths $L_{n,p}$ are increased proportionally. The reported photocurrent barrier and recombination at interfaces are also affected by the bias. Yet the EQE is not affected by the backward bias. This cell is so limited by absorption for the current density and probably by the surface recombination and non-radiative defects for the open-circuit voltage. A lower bandgap would also had improved the cell performances in view of the tandem solar cell.

3.4.7 Conclusion

In conclusion, lot of potential problems have been identified thanks to the simulations. Among these problems, mainly two have been verified: a low drift length and the existence of a photo-current barrier at the GaAsPN/GaP-n interface. Annealing have shown enhancement of all electrical parameters, allowing for the crystalline disorder and N-induced defects to be healed. Problems of heterogeneities have prevent us to be more conclusive. A systematic statistical study is needed in order to improve our knowledge of this alloy.

Finally, we have demonstrated a GaAsPN solar cell close to the actual efficiency record and a world record is expected.

3.5 GaAsPN for intermediate band solar cells

Besides to be used for its energy gap and lattice constant tunability, dilutes nitride are also widely harvesting in intermediate band solar cell. Indeed, the conduction band splitting creates de facto a three energy band structure: the E_- subband serves as the IB between valence band and conduction band being the E_+ subband.

Dilute nitride are part of the highly mismatch alloy (HMA) for IBSC research, along with dilute oxide for example. As a matter of fact, GaAsPN has even been the first dilute nitride used in such purpose [133], but the first HMA studied as a

potential IBSC candidate was ZnMnTeO [134]. Since, GaAsN has focused most of the attention in this area [135], [136]. The conduction band energy splitting with the addition of Nitrogen E_+ and E_- is described in the band anticrossing model [83]. In comparison of the other candidates, HMA have the benefit of having a large absorption in intermediate levels [136]. Recently, GaPN and GaAsPN have exhibited two-step two-photon absorption [137], [138].

In this section, we will evidence the potential of GaAsPN as a potential candidate for IBSC.

Evidence of two-steps two-photon absorption (TS-TPA)

One of the key process of IBSC is the photo-excitation of electrons from the IB to the CB, in our case from the E_- to the E_+ subband. In order to probe this photo-excitation, we have used the experimental setup described by Okada et al [139] (cf. Figure 3.4.7-1). The goal of this experiment is to quantify this photo-excitation by measuring the EQE with and without an infrared (IR) light bias. Classical EQE spectra are measured at short-circuit conditions with AC monochromatic illumination, before EQE spectra under the same conditions and with continuous illumination of IR light. The AC signals were integrated and averaged over 30 recordings using a standard lock-in technique. Monochromatic and IR illumination are produced by a Xenon lamp with a monochromator and AM1.5 filter respectively.

We are interested in

$$\Delta EQE = EQE_{IR:on} - EQE_{IR:off} \tag{3.5-1.}$$

Figure 3.4.7-2 depicts (a) $EQE_{IR:\ off}$ for selected samples (b) the ΔEQE obtained. We observe three behaviours. For diodes s1530 and s1572 the IR bias induce no effects on the current collection.

For diode s1568, ΔEQE shows a soft onset from the electrical bandgap energy until 440nm. After the effect of IR bias is rapidly decreasing. This diode exhibits the expected behaviour of an IBSC: in the spectral range where the IB is photo-filled by the monochromatic light, the IR bias increase the current collected. This effect starts decreasing exactly at the maximum of the high energy peak of the EQE for this diode.

For diodes s1569 and s1576 ΔEQE curves show three plateaus with three onsets: one at the electrical bandgap, one corresponding to the edge of the second peak on $EQE_{IR:\ off}$, and the last one at 360 nm.

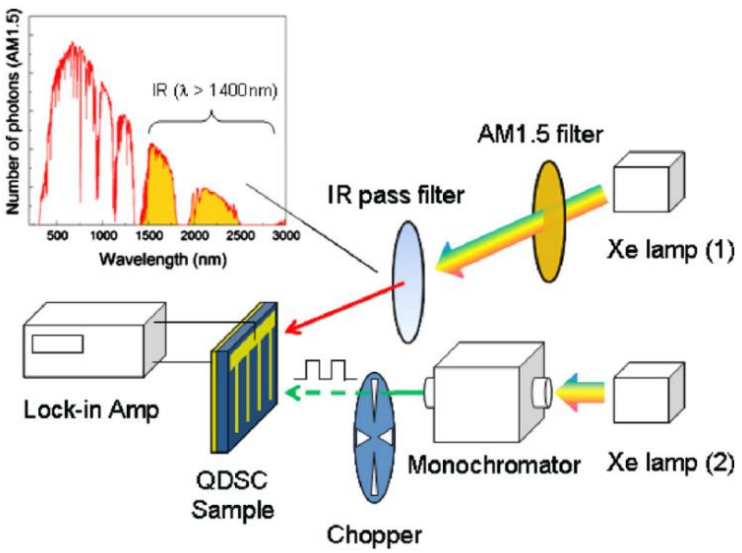

Figure 3.4.7-1: Schematic of the ΔEQE measurement technic. A chopped monochromatic light source serves to measure the current and a broad band IR light is applied to probe the TS-TPA. From [139]

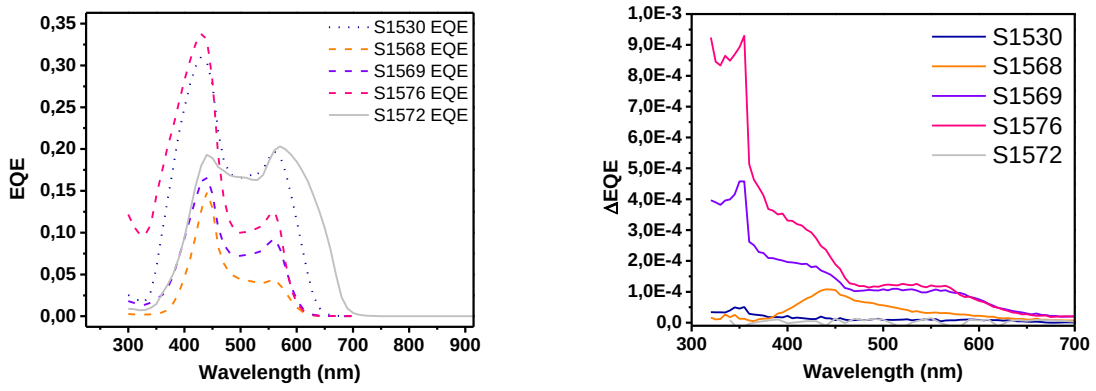

(a) (b)

Figure 3.4.7-2: (a) EQE and (b) ΔEQE measurements for samples with different electrical properties

The difficulty here to analyse those results relies on the correlation of transport properties and optical absorption. We will therefore refer a lot to the $EQE_{IR:\ off}$ spectra to analyse them.

In order to observe a TS-TPA effect, the IB has to be partially filled and those electrons has to remain in the IB. When working with dilute nitride with good collection efficiency in the E_- band, one has hence to block the carrier inside the IB. This is made with a blocking-layer which makes a photocurrent barrier specifically designed for the E_- subband [135], [136], [140]. This layer isolates the IB from the contact, making possible the voltage preservation of the E_+ subband.

In our samples, we noticed two diodes for which the IR bias has no effects. If we look closer to these diodes, one remarks that they have no collection problem for the E_- subband (this is demonstrated section 3.4.6 for the s1530 diode, and if we look at the EQE spectrum s1572 diode, collection at the E_- band is very good). It is therefore natural to obverse no TS-TPA on those diodes.

We expect to have such effects for the diodes with a low collection efficiency for the E_- subband and a good one for the E_+ subband. Diodes s1568, 1569 and 1576

are exhibiting such a behaviour, and for each of those diodes we note a significant TS-TPA.

The ΔEQE of the s1576 and s1569 diodes have the exact same shape. The first plateau was expected since the carrier collection from the E_- subband is very low for those diodes (cf. Figure 3.4.7-2(a)). The electrons are promoted in the E_+ subband and are better collected. On the other hand, the two other plateau are quite curious. They occur in a spectral range where IR bias shouldn't increase the current. Therefore, IR bias is in those cases probably a way for carriers to overcome an electron barrier.

As for the s1568 diode, the increase ΔEQE from the E_- energy to the E_+ one is interesting. The EQE measurement show small EQE values and a narrow spectral shape as well. This is especially true for the high energy maximum. We can suppose that the collection efficiency of this diode is poor even for the E_+ subband. Electrons generated at short wavelengths have to travel a long distance before to be collected. We can suppose that those electron can travel in the E_+ subband only for a part of this distance before to be trapped, and that the IR bias help them to escape and to be collected.

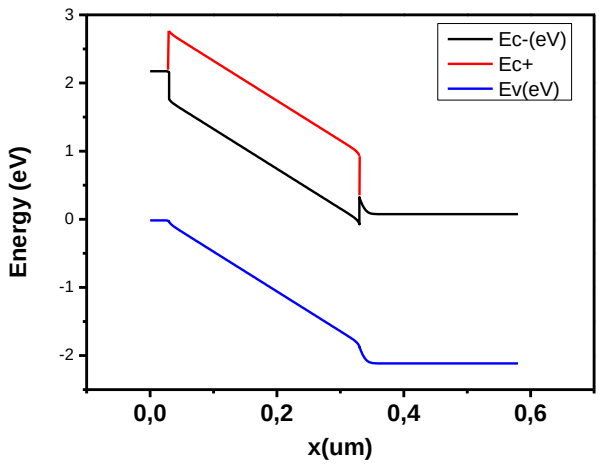

Figure 3.4.7-3: Band diagram for the GaAsPN alloy, exhibiting the E_- and E_+ bands.

3.6 Conclusion

In this chapter, the potential performances of a GaAsPN pin top cell has been simulated. The major reefs has been identified: the drift length, background doping and the energy band alignment. Reduction of the absorber thickness as well as growth and annealing processes are considered to tackle the drift length and background doping problems, whereas higher doping of the n-doped layer or substitution of GaP by AlGaP would be a solution to find a better band alignment.

Absorbers and pin diodes have been grown and studied through optical, opto-electronical and electrical characterisation methods. The absorption coefficient of GaAsPN has been measured by a spectrophotometre. The carrier dynamics has been investigated by steady-state and time-resolved photoluminescence. Steady-state PL spectra are dominated by luminescence from strongly localised subband gap states at low injection regime. With increase irradiance, the luminescence intensity above the mobility gap energy appears and becomes dominant. This analysis is confirmed by the time-resolved photoluminescence, where the localised states induce complex mechanisms such as hopping and trapping-detrapping of the carriers.

We have tried to analyse the electrical performances of the pin diodes through their luminescence properties. The localised states are however making those correlations complex, as the luminescence from localised states are problematic: as the localised states are strongly luminescent but prevents the carriers to be collected, the V_{oc} and the J_{sc} are actually decorrelated of the PL intensity. Furthermore, the spatial heterogeneity makes hard for the growing and annealing processes to be optimised. A large-scale statistical analysis would be required to improve the material quality.

Finally, we have exhibited the IBSC potential of GaAsPN, even for non-optimised band gap energies. A dedicated study, with samples designed on purposes would be interesting.

Chapter 4

Quantum confined heterostructures for multi-transitions photovoltaic systems

In the late years, several groups have developed some characterisation methods adapted to Intermediate band solar cells (IBSC). Most of them have tried to evidence the additional photocurrent gained with the addition of the intermediate level in the middle of the energy gap. Nevertheless, only two of them [135], [141] are able to probe the creation of a voltage difference between the carrier in the intermediate levels and those in the conduction band, which is the true condition for an IBSC behaviour. Indeed, whatever the extra-current we may obtain by the two-step two-photon-absorption (TS-TPA) through the intermediate states, if the voltage is determined by the transition between the valence band and the intermediate band, one cannot overcome the Shockley-Queisser limit.

In this chapter, we firstly detail the existent IBSC characterisation methods and will explain how the characterisation method we developed could be useful for the community. This method, based on luminescence analysis, is dedicated to evidence the two key mechanisms of an IBSC, TS-TPA and voltage preservation, providing a complete and powerful tool to investigate IBSC. Two IBSC candidates, based on quantum heterostructures, are analysed by classical measurements and luminescence based characterisations.

4.1 Experimental evidence of IB effect

4.1.1 Current –voltage measurements

The most direct way to determine the IB behaviour of a solar cell is to record J-V curves and see if it is overcoming the Schockley-Queisser limit. Unfortunately, it has never been the case yet. One can also synthesize two samples, one with IB and the second without, and compare their J-V curve. The cell without IB is called the reference or baseline cell (cf. Figure 4.1.1-1(a)). A simple comparison between the J-V characteristics under one sun illumination will however not be of great interest. Indeed at one sun, if the J_{sc} is expected to increase for the IBSC, the open-circuit voltage will decrease even for an ideal IBSC because of additional radiative transitions form the CB [142]. V_{oc} in the IBSC is actually supposed to converge to the V_{oc} of the reference cell as the concentration factor increase. This convergence, named "voltage recovery", has been electrically observed at low temperatures (see Figure 4.1.1-1(b)) [141] . It is a consequence of the saturation of the IB states. Nonetheless voltage recovery is not, in my opinion, a formal proof of an efficient IBSC. Indeed, saturation of the IB states will be efficient in samples where the IB density of states is low, implying that the TS-TPA will also be low, making the extra current collected through the IB states marginal. The experimental results so far are in agreement with this statement, as the only samples where voltage preservation has been verified are QD IBSC, the IBSC candidates exhibiting the lower TS-TPA. Such a recovery cannot be found in Highly mismatched alloys (HMAs) samples for example. A characterisation method evidencing voltage preservation and working in low concentration would therefore be of highest interest.

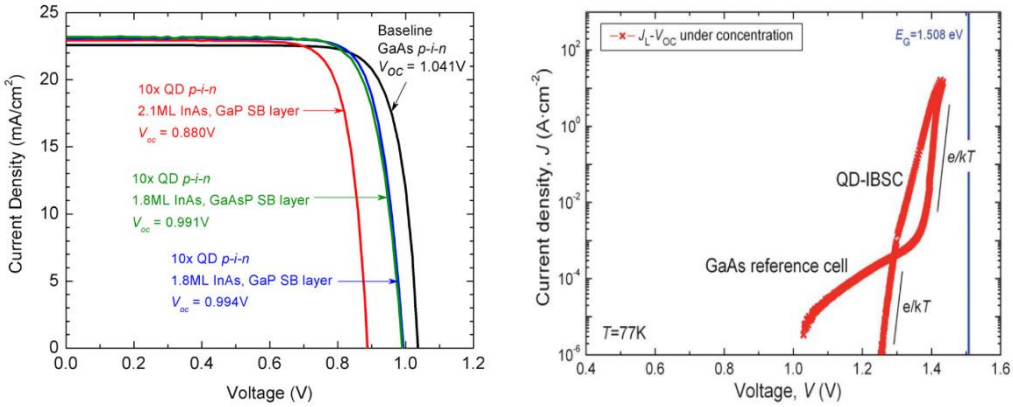

(a) (b)

Figure 4.1.1-1: (a) J-V curves for different QD-based IBSCs and their reference (baseline) call. The voltage loss is below 50mA/cm² [143]. (b) Example of voltage recovery by Linares [141]

4.1.2 Two photon subband gap photocurrent

To test the TS-TPA several methods implying current measurement and subband gap light excitation have been harvesting [140], [142], [144], [145]. These characterisation methods can be discriminated in two families: direct photocurrent measurement and EQE measurement. These methods are quite equivalent, since they focus on the photocurrent generated by a subband gap excitation. In the most basic configuration, in both cases, we illuminate a sample with a wavelength energetic enough to be absorbed by the host material and measure the current. The same operation is repeated after the addition of a second beam that could only promote electrons from the intermediate levels to the conduction band. The extra current is directly connected to the TS-TPA. Several samples have exhibited TS-TPA with this measurement, but only few at room temperature [140], [146], [147]. As an example, Figure 4.1.2-1 shows TS-TPA measurements for a GaAsN based IBSC, a QD based IBSC and a MQW superlattice based IBSC. The TS-TPA exhibited goes up to 1% photocurrent gain with IR bias excitation for the HMA sample. However, until the voltage preservation is verified, the sample cannot be seen as an IBSC.

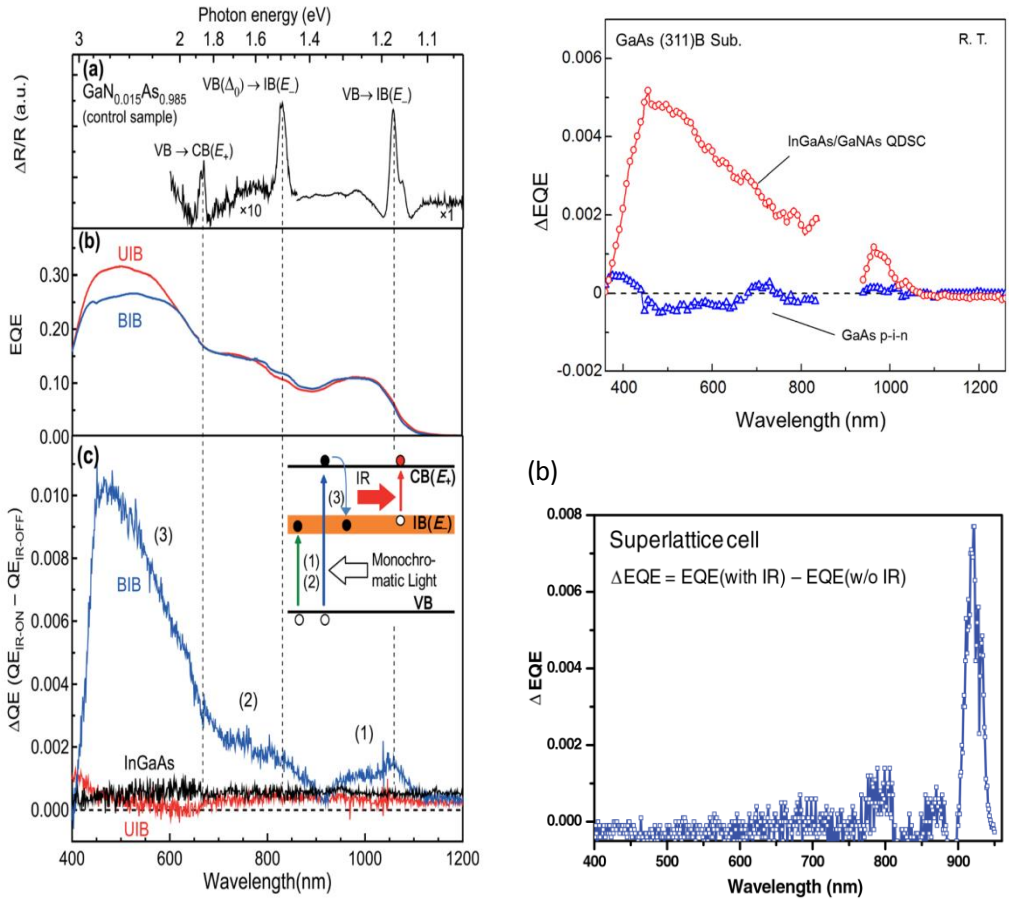

(a) (b) (c)

Figure 4.1.2-1: ΔEQE measured at room temperature for: (a) GaAsN samples [140], (b) InGaAs/GaAsN MSQD sample[147] and (c) A MQW superlattice sample[146].

4.1.3 Luminescence based characterisations

Luminescence based characterisations have already been identified as a powerful tool for the multi-transitions systems, as it allows to probe each transition specifically. It is especially true for IBSCs, where all the transitions occur in the same material. Professor Luque and his team have used electroluminescence (EL), in combination with QE, in order to measure the quasi-Fermi level splitting between CB and IB in dark and under high current injection at room temperature. A quasi-Fermi level splitting above 150 meV was found at an excitation of 5A.cm^{-2} [148]. This result was contested by Abouelsaood et al, [149] who argue that such

an excitation might have induced overheating of the sample, and therefore compromised the results.

Photoluminescence (PL) and EL have been studied in InAs/GaAs QD sample [150]. Authors claim that three "large" QFL splittings are attained, making this device working in the IBSC principles. This conclusion is however only based on the existence of luminescence peaks related to VB ↔CB transition and IB ↔CB transition. Lack of quantitative information and presence of the third transition related peak makes it impossible to be conclusive about the voltage preservation.

EL has also been used on HMAs (GaAsN) IBSCs [151]. In this paper, the authors exhibit an EL spectrum with the three transitions features at low temperature (15K) (cf. Figure 4.1.3-1(a)). This is a solid proof of the voltage preservation in this IB material and is confirmed with the J-V curves measured that denotes a clear change in the photocurrent and open circuit voltage (see Figure 4.1.3-1(b)). To the best of my knowledge, such a proof is only exhibited in this article. Unfortunately, for most of the IBSC studied, the IB ↔CB transition has energy too low to be recorded.

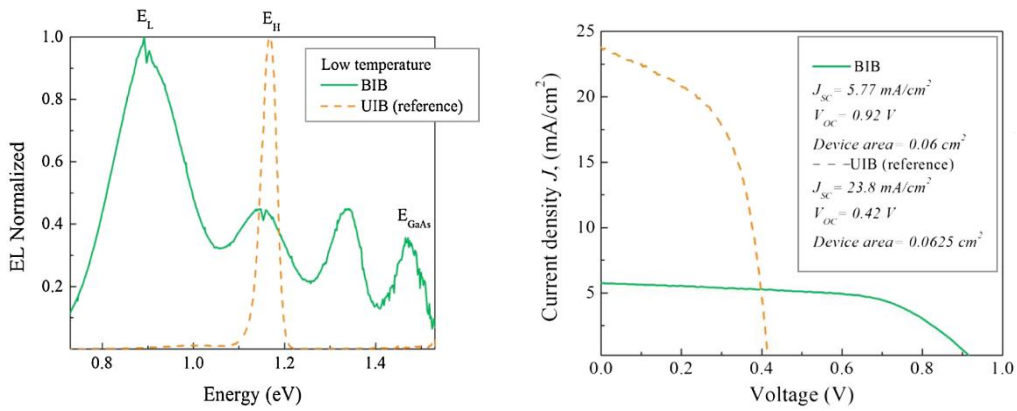

(a) (b)

Figure 4.1.3-1: (a) EL spectra for GaAsN samples with and without blocking layer. With this blocking layer the EL spectrum presents the three transitions luminescence peak. (b) J-V curves corresponding to these samples. The IBSC behaviour, with the blocking layer, exhibits a higher V_{oc} and a lower J_{sc} as expected in the IBSC theory. Figures reproduced from [151].

4.2 Developed Photoluminescence-based method

As seen in Chapter 1, luminescence is a powerful technic to analyse multi-transition concepts. In this section, we introduce a 100% optic technic able to probe the two key processes for IBSC: TS-TPA and voltage preservation.

4.2.1 Two-photons absorption (TS-TPA) with PL

TS-TPA in IBSC has been widely harvested and demonstrated (cf. sec4.1.2). Nonetheless, most of those techniques are complex and time consuming. We introduce here a simple method to quantify this fundamental mechanism based on PL.

The principle is close to the EQE based method, as it consists in a measure of the PL intensity with and without an IR light bias.

We have used the confocal microscope described in Chapter 2 with two CW laser excitations: one at 532nm and one at 1550nm. A multimode fiber optics coupler has been used to merge the two laser excitations in input of the confocal microscope. The luminescence is spectrally resolved by a Princeton spectrometer and recorded by a Si CCD camera. The optical powers used are detailed in the dedicated sections. All the measurements are made at open-circuit voltage.

Measuring the TS-TPA with PL presents several benefits. First of them is the possibility of characterisation at both stage: material absorber and completed solar cell. Furthermore the experimental setup is quite simple in comparison with other techniques. No lock-in setup is required. Concerning the information extracted from such measurement, recording the spectra gives access to the carrier dynamics of the intra-band absorption. Coupled with a variation of the excitation wavelength, we could have a deeper insight of those mechanisms than with the ΔEQE, and a fortiori with the ΔPC measurement.

In the following, we will apply this method on the two studied samples. Note that this method has recently been applied to GaPN alloy [138].

4.2.2 Absolute calibration, Δ μ determination and voltage preservation

The absolute calibration of the hyperspectral imager introduced in Chapter 2 gives access to the absolute value of $\Delta\mu(E)$ in the structure through the generalised Planck's law. Therefore it is possible to measure the exact value of the $\Delta\mu_{VI}$ and $\Delta\mu_{VC}$. If a significant difference between these two values is found (value noted $\Delta(\Delta\mu)$) we can affirm that the total devices voltage will not be limited by the intermediate band. There is then voltage preservation and the device will work as an IBSC. In practice, $\Delta(\Delta\mu)$ value has to be compared with the thermal activation energy kT. We will consider the criteria $\Delta(\Delta\mu) > kT+\varepsilon$, with ε=20meV being the systematic error of our system. At room temperature this leads to $\Delta(\Delta\mu) > 45$eV.

This method would be the first able to test the ability of an IB absorber to verify the voltage preservation at room temperature (RT) and low excitation regime.

In the two next sections, I will present the results obtained by the previously described method on two quantum-confined heterostructures both grown at RCAST laboratory: one multiple-quantum wells (MQW) sample and one multi-stacked quantum dots (MSQD) sample. The most promising structures are based on MSQD, mostly because the larger relaxation time for electrons from the CB to the IB in this case. I will first show the results obtained with the MQW sample, and secondly with the MSQD sample.

4.3 Quantum wells-based heterostructures

4.3.1 Sample description

In this section, for proof of principle purposes, we have used a MQW strain-balanced test device prepared by MOCVD, in epitaxy on GaAs, with 20 wells inserted in a pin structure, described in Figure 4.3.1-1 (a)-(b). This sample is well studied [152] and performs as a standard MQW solar cell as shown on Figure

4.3.1-1 (c)-(d). The EQE measurement, Figure 4.3.1-1(c), shows a carrier collection below the bandgap, from 1000nm, of ~20%. This extra carrier collection implies an increase of the photocurrent (Figure 4.3.1-1(d)) of 2mA/cm². On the other hand, the open-circuit voltage drops of around 50mV.

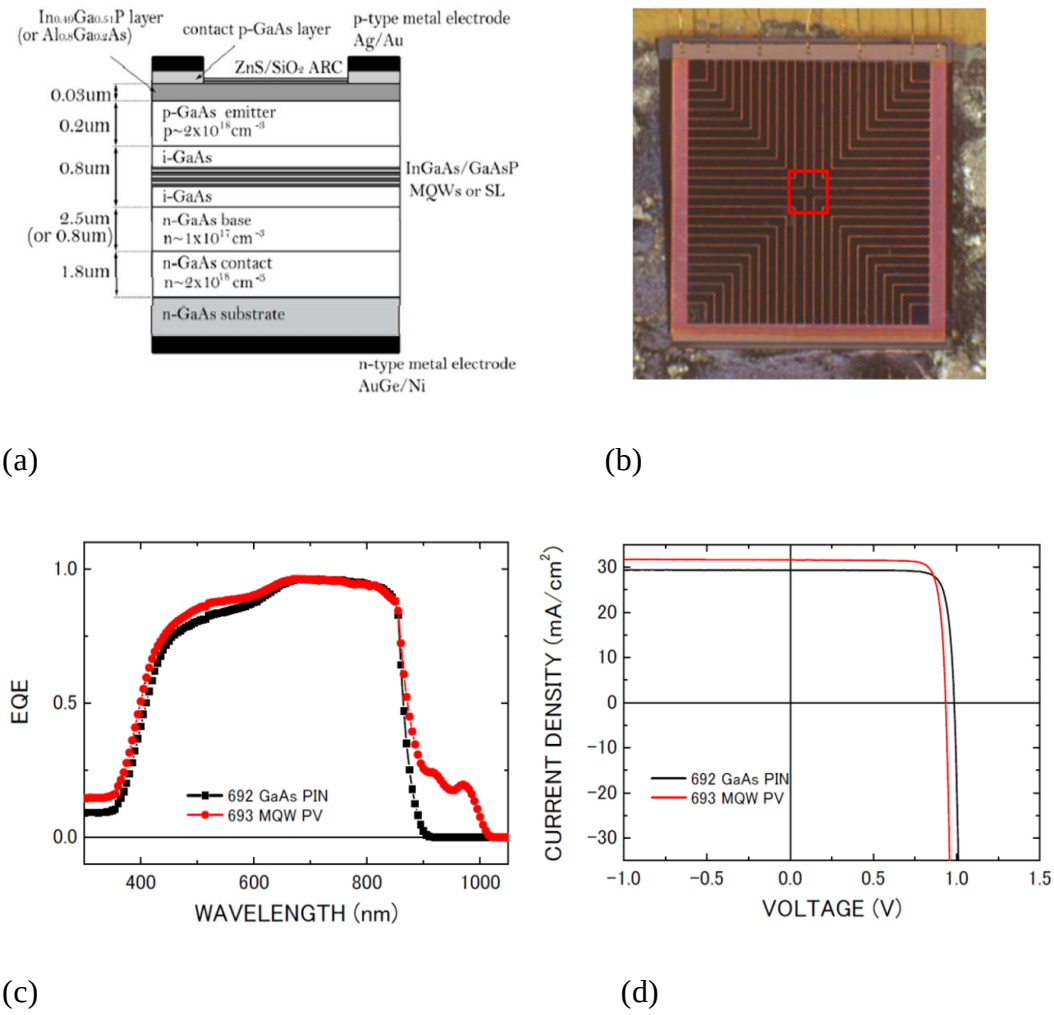

Figure 4.3.1-1 : (a) InGaAs/GaAsP based MQW sample structure. (b) Image of the sample. (c), (d) Comparison of EQE and J-V curves between the MQW sample and its reference cell without QW.

4.3.2 PL measurements

The luminescence spectrum of the IBSC candidate is recorded by a confocal microscope, with a micrometric laser excitation at 532nm. The acquisition is made at open-circuit voltage conditions. Result is plotted Figure 4.3.2-1. The PL spectrum exhibits two features. The MQW are emitting at 990nm, and the barriers at 874nm, the GaAs bandgap. We can notice that carriers recombine in majority in the QWs.

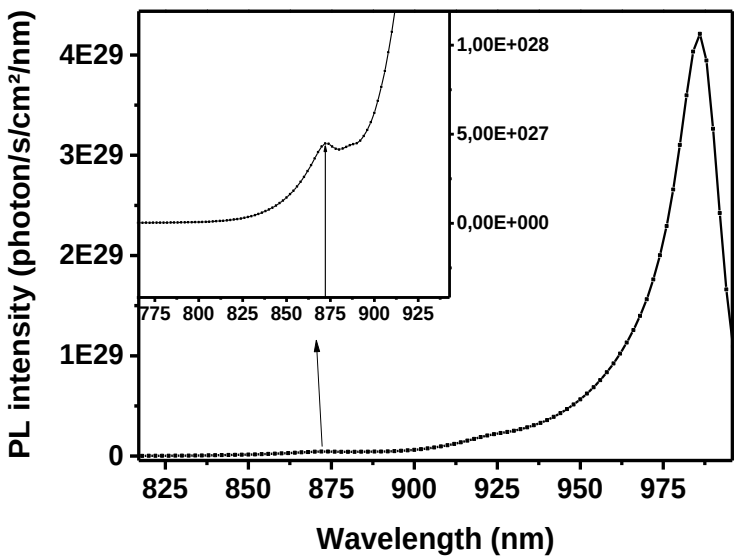

Figure 4.3.2-1: PL emission of the p-i-n GaAs solar cell (blue) and for the MQW sample (red). We denote a strong luminescence from the QW, underlying the fast recombination rate from the CB to the MQWs.

4.3.3 Two-steps two-photons absorption

TS-TPA on similar structure has been evidenced at room temperature with ΔEQE measurements [146]. We apply the experimental setup described in Sect.4.2. on this sample, with 532 nm and 1550nm laser excitation of 5,74mW and 3mW respectively. Figure 4.3.3-1 displays the PL spectrum without IR bias (dotted line) and the ratio:

$$\frac{\Delta PL}{PL} = \frac{PL_{IR:OFF} - PL_{IR:ON}}{PL_{IR:OFF}} \quad (4.3\text{-}1.)$$

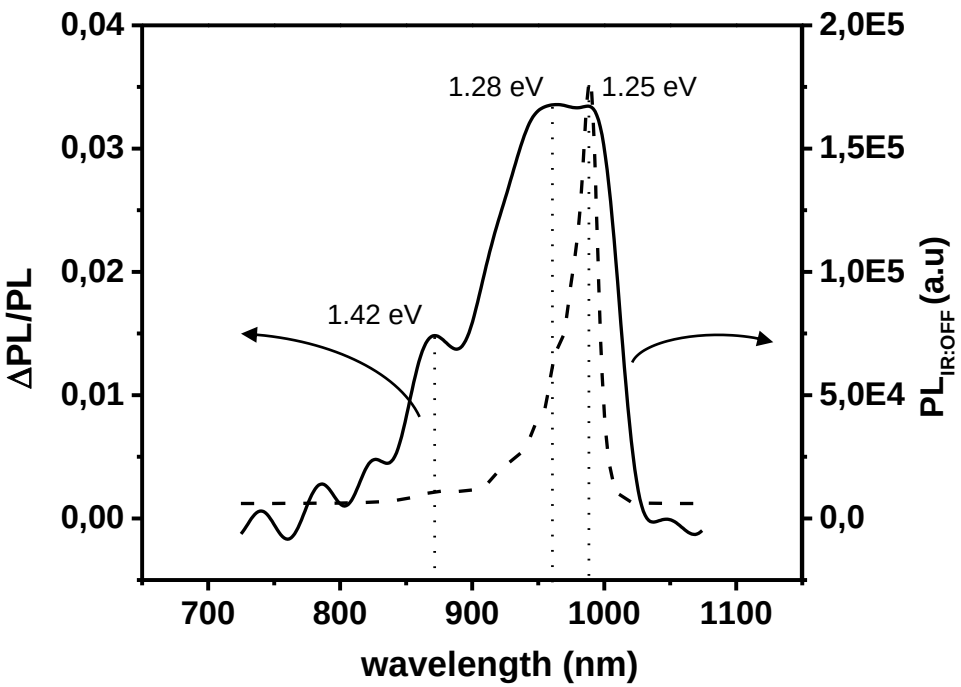

Figure 4.3.3-1: (left) ΔPL/PL. (right) $PL_{IR:OFF}$. The sample exhibits the same TS-TPA efficiency for both the baseground and the excited states.

ΔPL/PL reflects the TS-TPA efficiency. In this case, it is strictly positive with three local maxima corresponding to the three transitions exhibited in the $PL_{IR:OFF}$ spectrum. They correspond to radiative recombinations in the GaAs at 1.42eV, to the baseground and the excited states in the wells at 1.25eV and 1.28 respectively. We denote an equal TS-TPA efficiency for the QW fundamental states and excited states, around 3,5%. The intraband absorption does not decrease with the decrease of $E_{bound\ to\ continuum}$, in contradiction with the literature [153]. TS-TPA is also significant for the CB, around 1,5%, which was not expected. To analyse this result, we consider the three excitations model depicted in Figure 4.3.3-2 (the definitions used are defined in the legend). This model was introduced by Professor

Kita [154], who studied the carrier dynamics in QD based IBSC. In this model, a subband gap laser pumps electron in the conduction band of the barriers material, here GaAs, before recombining in the intermediate levels. At this point, an additional IR laser excites those carriers from the intermediate band to the extended states of the barriers. The IR bias excited electrons are considered being placed in a parallel circuit. This way less carriers are in position to recombine radiatively, and PL intensity decreases. Note that this model relies on experimental studies. This model explain why the global PL signal should decrease with IR bias laser. We can however question the decrease of the PL in the barrier material. For the TS-TPA in the CB, two cases are to be considered: or the same mechanism occurs for the carriers in this band or, as the promotion of the electrons from the IB to the extended states decreases the IB population, τ_{CI} decreases, so does the population in the CB. This case is however unlikely taking into account the carrier density in the CB under high irradiance.

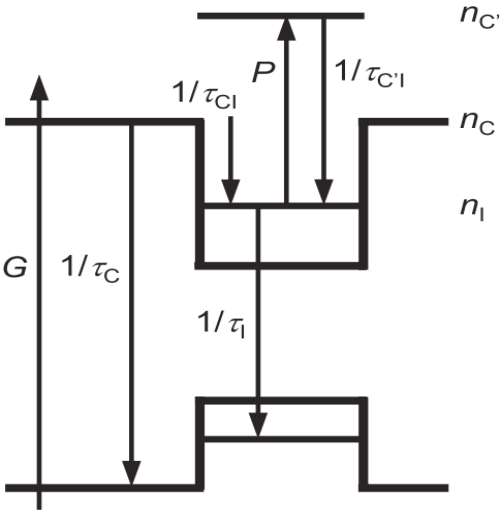

Figure 4.3.3-2: Three levels model excitation and the corresponding relaxation rates. This figure is reproduced from [154]. Electrons are excited by the pump laser in the conduction band at a rate G. From there they can either recombine in the VB (at a rate $1/\tau_C$) or in the IB (at a rate $1/\tau_{CI}$). Once in the IB, a part of the electron will be promoted to the CB extended states at a rate P, when the rest will recombine to the VB (at a rate $1/\tau_I$). Note that the non-radiative recombinations are no considered here.

The MQW-based IBSC has shown significant TS-TPA proving that optical transition between the IB and the CB are efficient. We will now probe the voltage preservation in this sample.

4.3.4 Hyperspectral measurements

We want here to probe the IB behaviour of this sample by the previously described method. The PL emission is recorded by the hyperspectral imager. Application of the procedure described in Chapter 2 on a MQW sample has been questioned in [155], with positive conclusions: the high mobility in the host material allow to consider that the Δμ is uniform within the structure, whereas the electronic density and the carrier dynamic allow to apply the generalised Planck's law directly. A homogeneous illumination from the laser at 532nm is applied to the sample at three different excitation powers excitations. The PL emissions are plotted in Figure 4.3.4-1(a). We can discriminate the emitted photons in two populations: one clearly emanating from the QWs between 990 and 900nm, and one below the GaAs bandgap, 874nm, where the photons can correspond to transitions in the GaAs or in QW material. From those spectra, we extracted the Δμ(E), depicted on Figure 4.3.4-1(b), using the generalised Planck's law once again. Δμ(E) exhibits two distinct domains where its value is constant: a Δμ value for the transition from the barrier to the valence band, and a value for the transition from the wells to the valence band. The QFLs difference between the wells and the barrier, Δ(Δμ), is ~15meV.

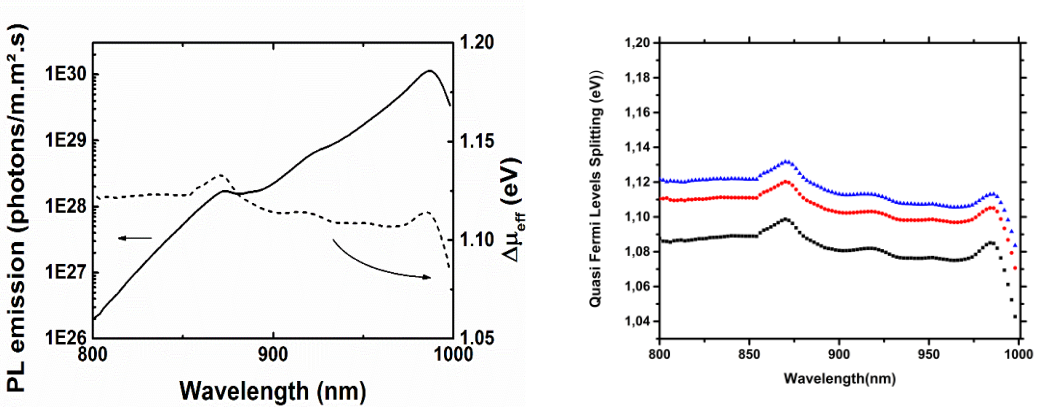

(a) (b)

Figure 4.3.4-1 : (a) PL emission of the p-i-n in absolute values (left) and the extracted Δμ (right). (b) Quasi-Fermi level splittings as a function of the emission energy, for three different powers. A weak difference (~15meV) exists between the QW region and the barrier region

4.3.5 Discussion

The Δ(Δμ) found for the MQW sample is around 15meV and is below 45meV. Hence, it cannot be considered as representative of an optical transition. As a conclusion, we cannot affirm that the voltage of the cell is not limited by the intermediate levels, and so the sample does not exhibit an intermediate band behaviour. Also this 15 meV difference does not change with the increasing excitation power. This further confirms the absence of an intermediate band effect. We notice finally that Δμ(E) spectrum varies with the concentration ratio c as a translation of log(c) for the entire spectrum (see Figure 4.3.4-1(b)). This behaviour confirms that the carriers in the CB and in the QW states can therefore be described by the same chemical potential. This is not particularly surprising as the confinement in the QW is only 1-D, resulting in a very fast relaxation from the CB to the IB and a continuum states energy between the CB and the QW region.

4.3.6 Conclusions

To summarize, we have shown that the MQW sample exhibits TS-TPA with dual-beam PL measurements. This measurement allows to spectrally access the TS-TPA efficiency, which cannot be probed with classical TS-TPA measurement setups.

As it happens, in the MQW sample, TS-TPA efficiency is quite constant in the QW region, and is lower in the GaAs bulk region. We used a three energy level model to identify the carrier dynamics.

On the other hand, HI measurements have not exhibited a sufficient $\Delta(\Delta\mu)$ between the relevant transitions. Therefore, we can state that recombination between those bands are dominated by thermionic recombinations ($1/\tau_{CI} << e_{thIC}$) making impossible an IBSC behaviour.

4.4 Quantum dots based heterostructures

4.4.1 Sample description

In this section we present the results of the method previously described on a 350nm-thick quantum dots solar cell grown at RCAST by molecular beam epitaxy (MBE), in epitaxy on GaAs, consisting of AlGaAs p-i-n diode with 10 InAs/AlGaAs QDs layers in the intrinsic region, described Figure 4.4.1-1. The QDs have been grown in the Stranski-Krastanow growth mode [156]. This method is very interesting for its capacity to grow thin QDs with large density (around 10^{11} QDs.cm^{-2}). The main drawback of this process is the inherent wetting layers that are induced (cf. Figure 4.4.1-2). The wetting layers (WL) are a thin quantum well underneath each QD layer. A quantum well add systematically intermediate and not-confined energy states between the CB and the IB of the IBSC [157]. One can consider that the CB of such QD IBSC is actually the energy baseground of the WL, reducing the IB$\leftrightarrow$CB transition and so the probability of voltage preservation. This will be of great importance when we will analyse the $\Delta\mu$ in the structure. Besides, the density of states is discrete in a QD. As an example, the electronic structure in a GaAs/InAs QD system is presented Figure 4.4.1-2(b). We observe multiple states in the QD.

The most investigated systems for IBSC applications are the InAs/GaAs and InAs/GaAsN QD heterostructures. Our sample has been designed specifically as a

potential IBSC, with the QD baseground placed at 1.24eV, and the host material CB at 1,65eV. In comparison with the most studied QD-based IBSC system, InAS/GaAs, the InAs/AlGaAs system has an energy band diagram more suited to the IB behaviour. The band gap energies are closer to the ideal case - with E_G=1.65V, E_H=1.2eV and E_L=0.45eV - and the higher barrier energy induces a stronger carrier confinement, maximizing the chance of voltage preservation [158].

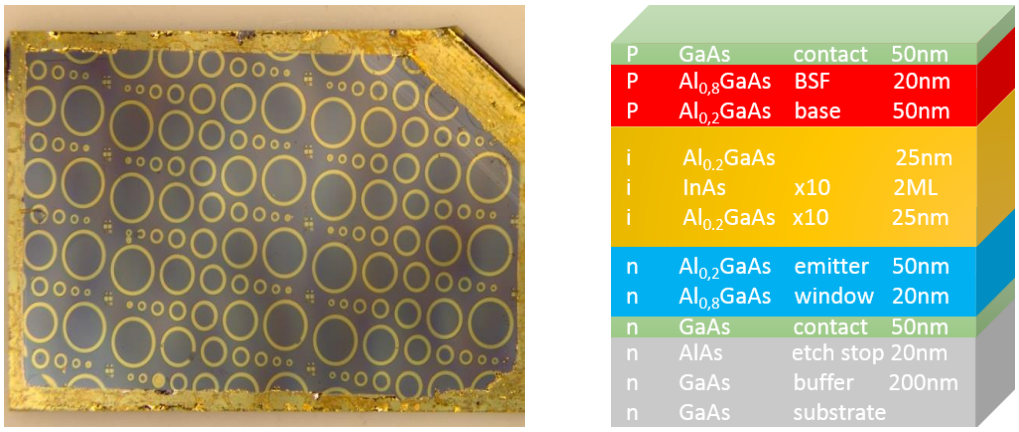

(a) (b)

Figure 4.4.1-1 : (a) picture of the MSQD sample. Each circle is an isolated diode (b) Detailed structure of the MSQD sample

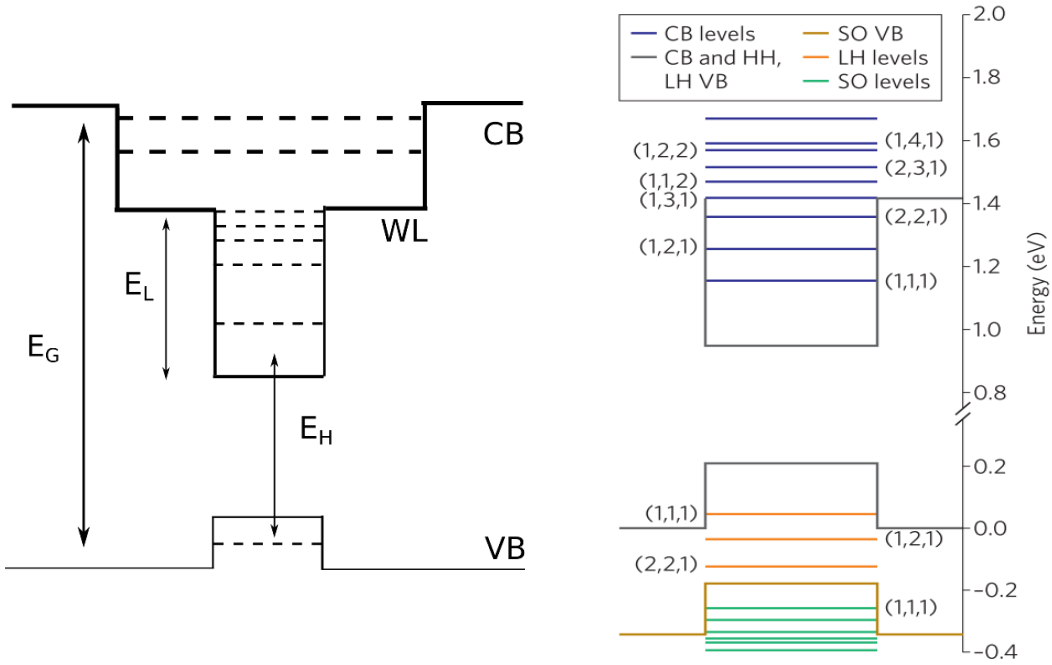

(a) (b)

Figure 4.4.1-2: (a) Modified electronic band structure in the IBSC sample with the presence of the WLs. (b) Calculated electronic band structure in a InAs/GaAs QD system from [159]

4.4.2 Optical management structure

In real illumination conditions, the QD-based IBSC systems suffer from a low absorption rate in the two transitions implying the IB. In order to test the influence of an absorption exaltation in the QD region, an optical engineering is performed. The GaAs substrate has been removed, and the active part of the sample has been transferred on a gold mirror by epitaxial layer process. The structure is shown Figure 4.4.2-1, and the detailed process is reported in [160]. This transfer operation has been carried out by the LPN. The result is a 350nm-thick n-i-p solar cell which forms Fabry-Perot cavity that creates Fabry-Perot resonances. The effects of this transfer are depicted Figure 4.4.2-1 (c), featuring the EQE for the non-transferred sample and the 1-R(λ) for the transferred one. The EQE for the non-transferred cell is representative of the absorption in the cell since the host-material, AlGaAs, has great carrier mobility and therefore has a collect function around 1. This approximation is comforted by Figure 4.4.2-1 (d), where EQE(V) has been plotted,

since the EQE has not increased when we applied an inverse bias. As for 1-R(λ) curve, it can also be considered as the absorption in the transferred sample. For further details, see Sec.4.4.3.2 dedicated to the absorption measurement. Figure 4.4.2-1 exhibits $|E|^2$ in the structure, provided by the LPN. This value is representative of the absorption in the structure. We note that the FB cavity increases the absorption especially for the QD in the centre of the QD layer. This FB resonance occurs at 1046nm near the QD baseground. This resonance will increase both photofilling of the QD and the TS-TPA, two crucial processes in IBSC operation.

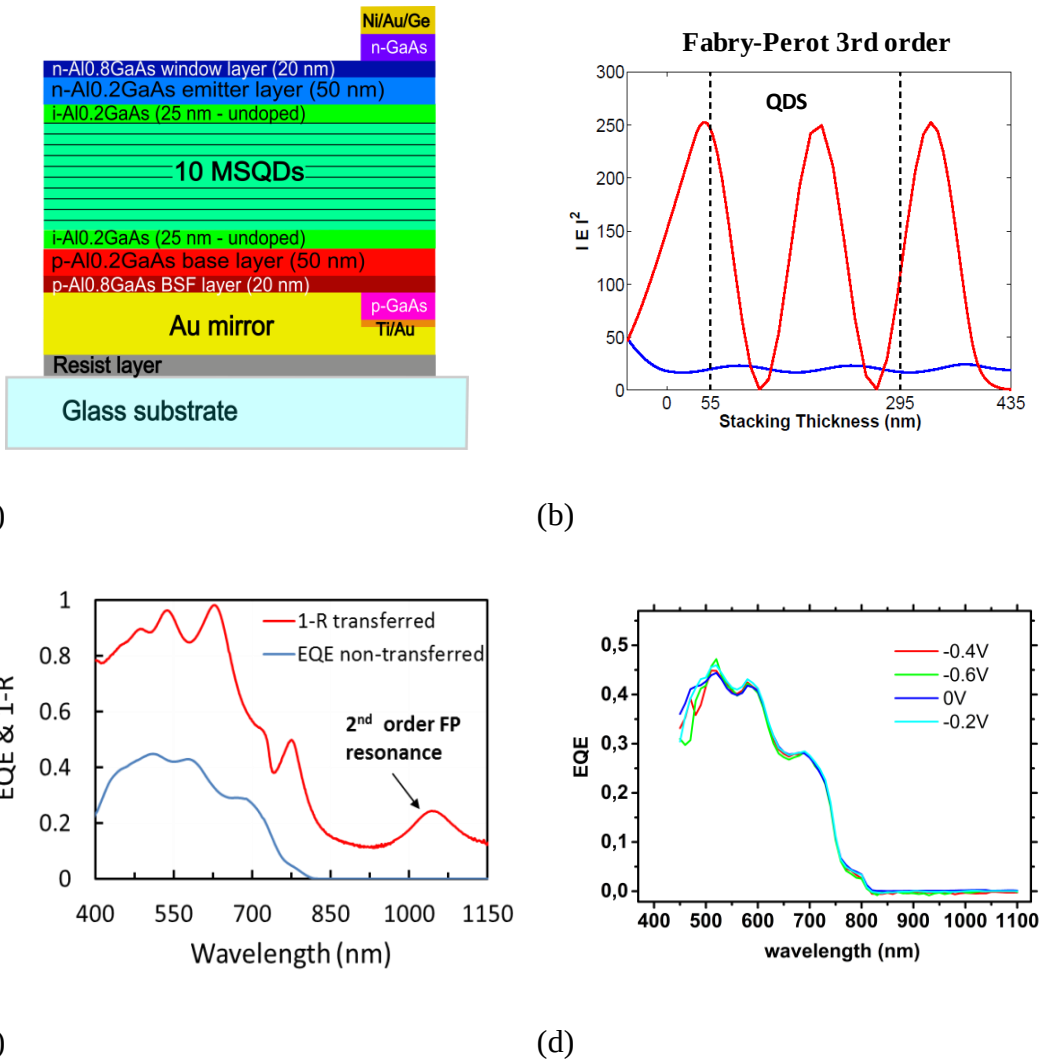

Figure 4.4.2-1 : (a) Description of the transferred structure. (b) $|E|^2$ in the transferred structure. (c) Comparison of EQE for non-transferred sample and 1-R(λ) for the transferred sample. (d) EQE(V). The EQE doesn't change with application of a reverse bias.

Fabry-Perot cavity effect

PL measurements (see Sec.4.4.4) before and after transfer procedure have been performed with a confocal microscope. A green laser emitting at 532nm and an excitation of $2.3.10^6$ W/m² are used. This high irradiance is chosen in order to be sure to saturate the QD ensemble. This way, all the states in the QD ensemble participate at the luminescence and the effect is quantifiable. The results are plotted Figure 4.4.2-2. The comparison of the PL signals for the transferred and the non-

transferred samples gives the exaltation ratio obtained thanks to the Fabry-Perot cavity. This ratio is around 7 for the integrated PL signal. The inset displays the two PL spectra normalised. The cavity has only little effect on the FWHM of the QD peak, and on the spectral position the PL maximum. It has to be noted that spectral comparison between the two samples is tricky, since a significant heterogeneity has been observed, and especially a radial transition energy gradient of the PL.

A TRPL measurement has also been carried out for these two samples. A green pulsed laser has been applied to both samples. Results are displayed in Figure 4.4.2-3. The transferred sample exhibits a faster decay. As the Integrated PL intensity is also higher, this shortening in the PL decay is due to a decrease of the radiative lifetime in the QD. Furthermore, as the

From those experiments, we can deduce that the radiative recombinations dominate in the QDs and that the cavity enhances the absorption and radiative recombination for the VB ↔ IB transition.

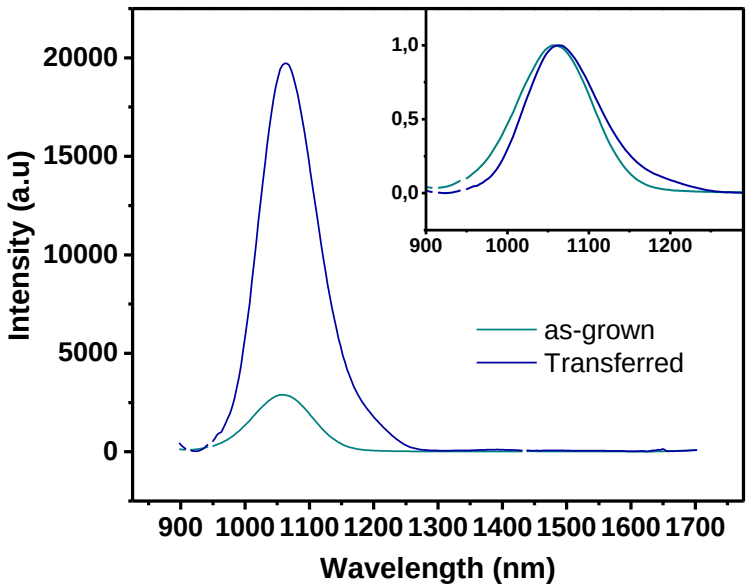

Figure 4.4.2-2: Comparison of the PL spectra for the transferred and the as-grown samples. An exaltation factor of 7 is found for the integrated PL intensity.

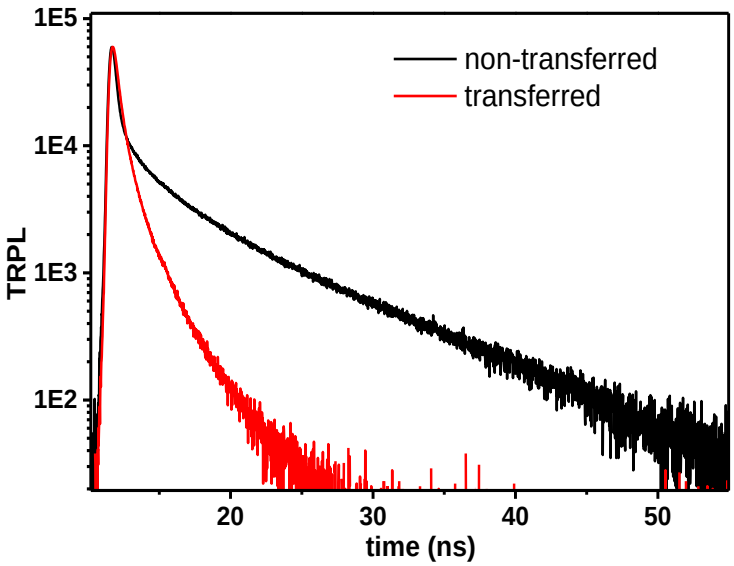

Figure 4.4.2-3: TRPL curves for transferred (red) and non-transferred samples. The transferred sample exhibits a faster decay.

4.4.3 Particularities of QD-based IBSC

MSQD samples have very unique behaviour, making their luminescent properties particular. We will therefore focus first on generalised Planck's law application conditions.

4.4.3.1 Generalised Planck's law and QD ensemble

A direct determination of a μ_{QD} in the QD ensemble implies that a unique μ_{QD} exists in all the QDs and thus we can transpose the generalized Planck's law to a QD ensemble.

As we detailed in chapter 1, the generalised Planck's law is valid only if a chemical and thermal equilibrium is set for all the occupied states in the considered band. This question is especially complex for the QDs. QDs are indeed an ensemble of isolated and confined structures, questioning naturally the condition of chemical equilibrium. Several transport mechanisms can however allow this equilibrium: formation of a miniband [161], thermionic escape to the wetting layer [162],

resonant tunneling and charge hopping (phonon-assisted tunnelling) [163], [164]. Among those mechanisms, we can notice that thermionic escape would above all means loss of $\Delta\mu_{IC}$, and so preclude the IBSC effect. In this first case we expect a constant μ_{QD} over the entire spectral emission range.

In the second case, if no equilibrium exists between the QD, the generalised Planck's law is no more valid for the whole QD spectrum and all studied QD have their own chemical potential. In this case, we expect the μ_{QD} to vary with the considered emission energy.

In all cases, the main difficulty stands in the determination of the absorbance term in the generalised Planck's law. In a QD ensemble this value is very hard to measure. A QD ensemble is an ensemble of similar, but not same, QD size. The direct incidence of this dimensional distribution is an energy transition distribution, as the energy levels in a QD depends on its size. Furthermore, as the density of state in a QD is discrete, the absorption saturates once all the states are filled, and the absorbance of the QD ensemble becomes null [165].

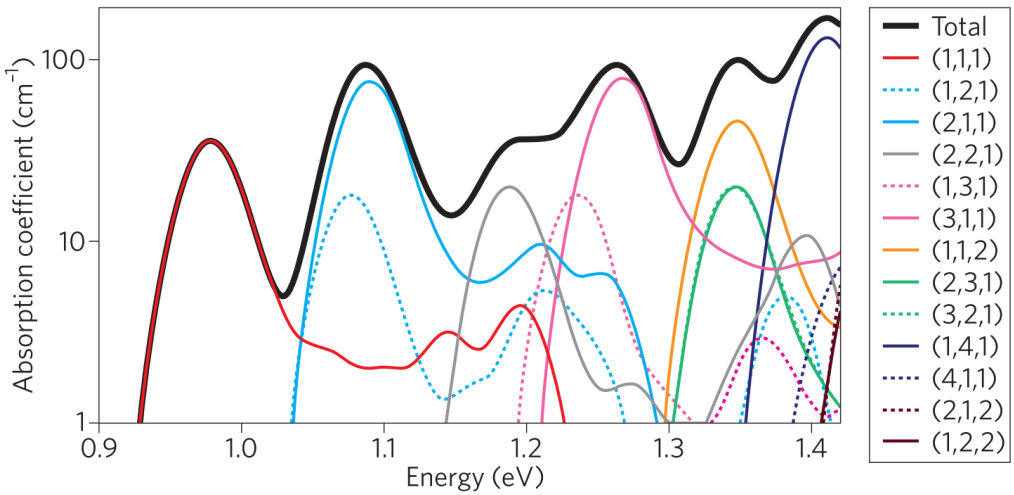

Figure 4.4.3-1: Absorption coefficient of and InAs/GaAs QD ensemble. The existence of discrete energy levels and the size distribution of the QD makes the absorption coefficient. This result is simulated. From [159]

In order to test these hypothesis, we could increase the samples temperature. This way, the thermal escape from the QD would force a chemical equilibrium to be found. An observation of the evolution of Δμ(E) as a function of the cells temperature would have given important information in this regard.

In both cases, it is fundamental to determine this absorption by the cell. Three strategies have been set up and compared in the following:

- **Reflectometry measurement**
- **PLE measurement**
- **Absorption measurement by comparison with a reference sample**

4.4.3.2 Reflectometry measurements

This measurement consists in measuring the ratio of the light reflected by the sample on the incident light:

$$R(\lambda) = \frac{I_{reflected}(\lambda)}{I_{incident}(\lambda)} \qquad (4.4\text{-}1.)$$

The measure is done with the IQE measurement device from Newport. The reflected light is measured by a detector inside an integrating sphere. For the transferred sample, as the layers are deposited on a gold mirror, the reflected light contains both the reflected light at the surface and the light which has not been absorbed by the structure. Therefore (1-R(λ)) gives directly the absorption in the sample from all the structure, including the gold mirror. This is particularly troublesome as the electrical field is enhanced in the QD region, and the absorption in the mirror will also be increased. Simulations have been made to calculate the absorption in the same structure without the QDs. In this simulation the absorbed light in the QD spectral region will only be done by the mirror. This allows us to determine the absorption in the QDs after having subtracted it to the measured data. Figure 4.4.3-2 displays the results.

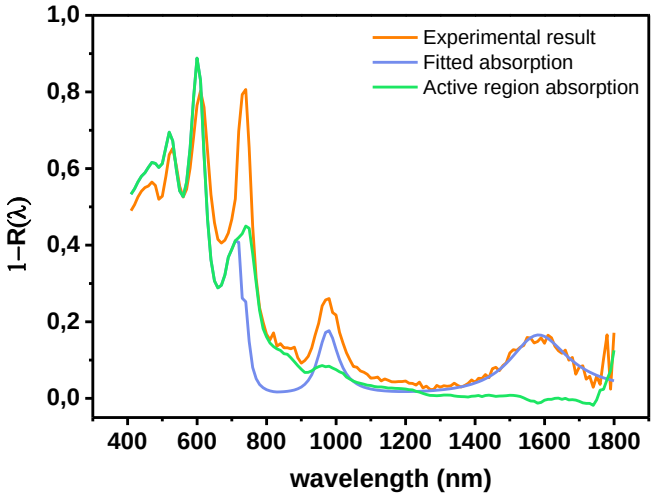

Figure 4.4.3-2 : Absorption obtained from reflectometry measurements

The measured curve exhibit several features. The peaks from 400nm to 750nm are the result of interferences. In this range the light is absorbed by the AlGaAs material. The other peaks are the result of the Fabry-Perot resonance. The one at 1600nm is the first order resonance. In this spectral region, the light is only absorbed by the metal. We used this peak to fit the Fabry-Perot resonance, and the n,k indices of the gold mirror. The peak at 990nm is the 3rd order resonance of the FB cavity. It reflects mostly the absorption in the mirror, but also in the QDs. The green curve, representing the absorption in the active region, gives a quantitative value for the QD ensemble around 10%.

4.4.3.3 Alternative absorption measurement

PL-E

As seen in chapter 2, PL-E measurements can be used to access the absorption in a sample. We used a 532nm laser, wavelength where the absorption is close to 100% (cf. Figure 4.4.3-2), and the power excitation range between 0,5mW and 10,1mW.

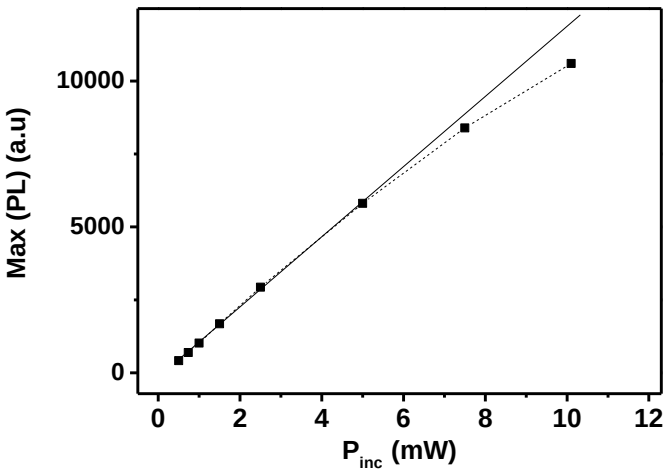

Figure 4.4.3-3: Evolution of the integrated PL intensity as a function of excitation power. A linearity is found up to 5mA/cm², which corresponds to an irradiance of 15000 suns

At low irradiance the linearity law is respected. With high irradiance, the QDs start to saturate and the PL intensity increase slows down. In conclusion, below 5mW/cm², the linearity validates the use of PL-E.

We can calibrate those data with the reflectometry measurements: The data are normalized by the value of the absorption peak at 610nm, where both 1-R(λ) and PLE(λ) reach their maximum, and moreover where the gold is not supposed to absorb any light in this region. The luminescence is recorded at 1070nm, in the QD groundstate region

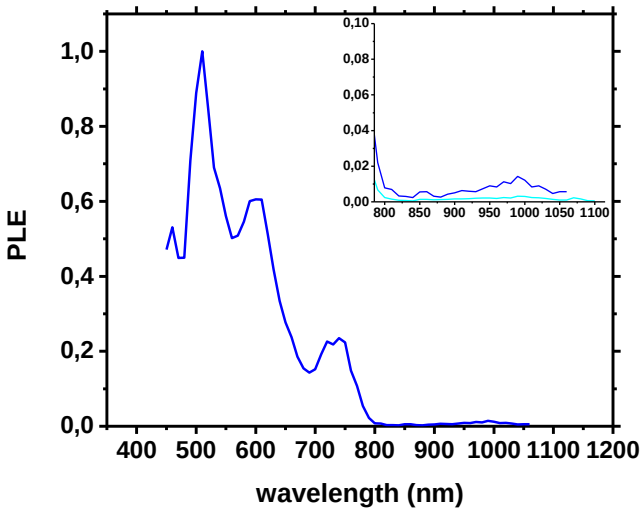

Figure 4.4.3-4 : PLE measurements of the transferred sample. In red the PLE curve for the In the inset is displayed a zoom on the QD area.

The PL-E curve has a similar shape than the 1-R(λ) measurement. The peak at 510 is believed to be an artefact from the second order of the laser excitation, not filtered by the monochromator. The signal in the QD region is smaller than expected. This could be a consequence of the polarisation of the excitation wavelength.

Determination with the non-transferred cell as reference perspectives.

A differential measurement could be interesting. By measuring the absorption in the whole sample with the reflectometry on a reference cell, we could by subtraction get access to the QD absorption. This will be done in a near future.

4.4.4 PL measurements

PL measurements have been done on QD samples. In addition to classical information, PL also gives access to: (i) QD size distribution, (ii) PL spectra shift with increased irradiance, (iii) QD saturation irradiance threshold and (iv) effect of the FB cavity on the PL.

4.4.4.1 Power dependence study

Irradiance dependence of the QD PL spectra is presented in this section. We have used a green laser emitting at 532nm and several irradiance excitation from 0.1W/cm² to 5327 W/cm². Figure 4.4.4-1 displays the normalised PL spectra and the luminescence intensity for all studied irradiances. At low irradiance, spectra are asymmetric and emission is located at low energy (1058nm for 2.2W/cm²). With increased excitation, we note a huge blueshift: the PL maximum shifting from 1114nm to 980nm (150meV) for 5327W/cm². This behaviour is well-known [166]: at low irradiance, carrier are trapped in large QD size. As these QDs fill, electrons and holes are trapped in smaller QDs, causing the mean energy emission to increase. At high irradiance the PL spectrum stabilises, so does the PL intensity. The QDs are then saturated. Mechanisms responsible for this spectral shift can be questioned. Oscillator strength from WL to QD groundstate is proportional to energy transition [153], and hence is higher for the large QD enhancing recombination in those dots. In the case of high QDs density, overlapping of electron wavefunctions allow direct transport from QD to QD, causing the QD ensemble to behave like a mini-band. However, taking into account the spacing between our dots (around 30nm) this is not the most probable mechanism.

Besides PL spectra shapes are not constant. We observe a local maximum at 1058 nm for 0.1, 2.2 and 13 W/cm². We think that this local maximum is a signature of a bimodal QD distribution, phenomenon well-known in InAs based QD systems [167]–[169]. In addition, it seems that PL spectra are deformed on either sides of peaks centred on around 1000nm. This is the FB cavity effect, which is in the middle of this spectral range (cf. Figure 4.4.3-2).

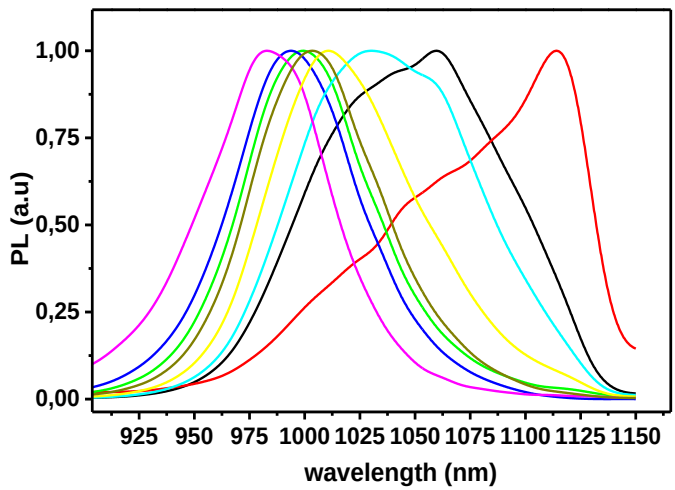

a)

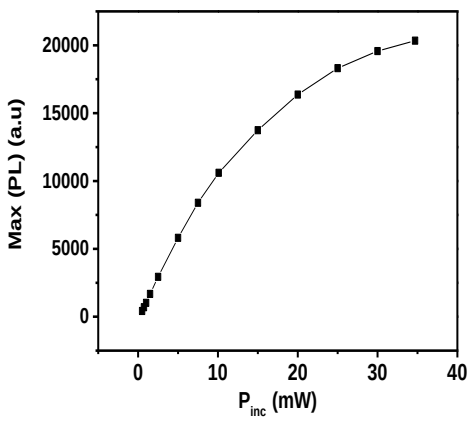

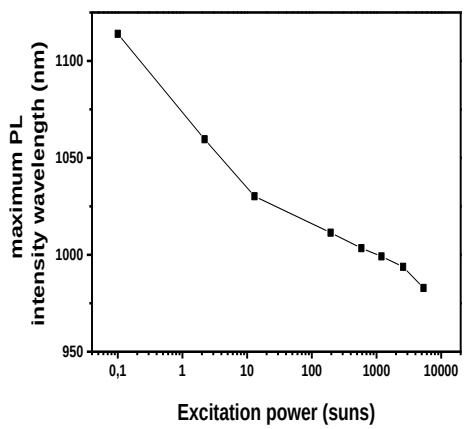

(b) (c)

Figure 4.4.4-1 : (a) PL signal for transferred sample with power excitation increase. (b) Power dependant evolution of the maximum intensity of PL. (c) Evolution of the $\lambda_{PL,max}$ as a function of the incident irradiance

In conclusion, even if the QD emission is strongly power dependent, this is probably because of a higher probability for electrons to recombine in large dots, and not because an equilibrium is established between the dots. This will be important for the following.

4.4.5 Two-steps two-photon absorption

TS-TPA in QD IBSCs samples is the main problem of QD-based IBSC. Indeed, because of the low density of states in the QDs IB, the increase of photocurrent via the IB is limited.

As said before, several QD based IBSCs have shown TS-TPA. Most of them only at low temperature. In those systems, InAs/GaAs QD for example, the IB ↔ CB transitions are dominated by thermionic recombinations at RT. In addition to the TS-TPA effect blinding, this domination also makes IBSCs voltage preservation impossible. Up to now, only few QD-based IBSC systems exhibited TS-TPA at room temperature [140], [147], with an InAs/GaAsN QD/barrier system.

4.4.5.1 Experimental result

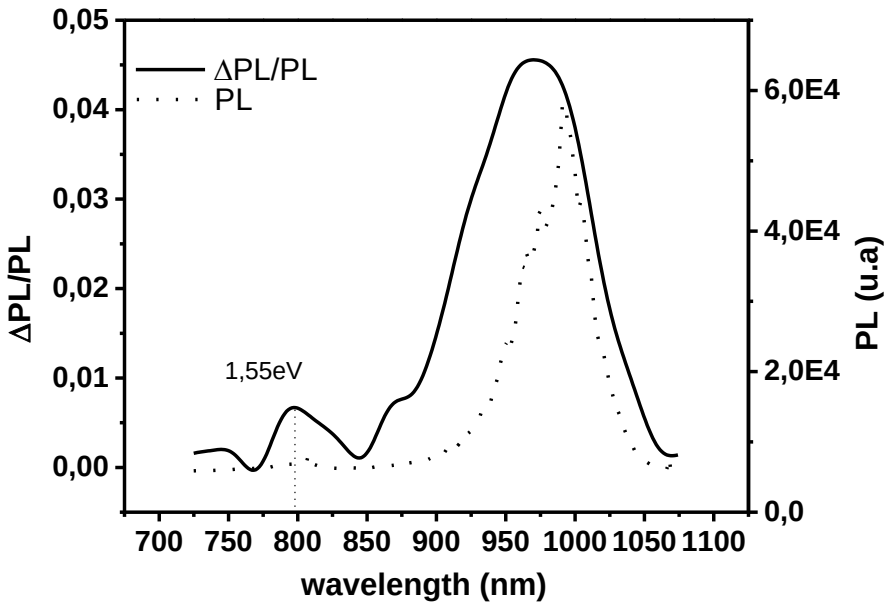

Figure 4.4.5-1: ΔPL/PL (straight line) and PL (dotted line) with P_{pump} =1,04mW and P_{IR}=3mW

The ΔPL/PL curve shows a better TS-TPA efficiency for the high energy part of the QD ensemble, with a maximum at 971nm (1.27eV).

4.4.5.2 Power dependence study

In this section we are interested in the influence of the pump laser power, while maintaining IR laser power constant, at $1.2.10^3$ W.cm^{-2}.

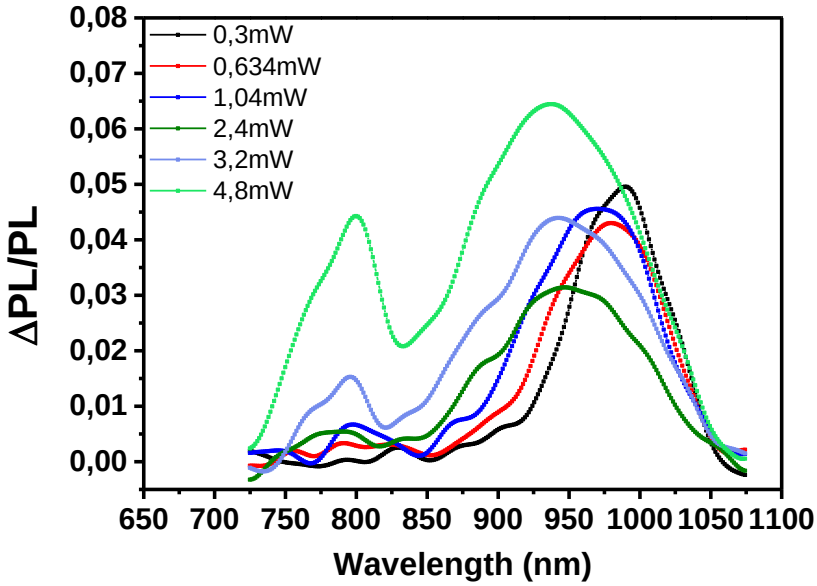

Figure 4.4.5-2 : $PL_{ir:off}$-$PL_{ir:on}$/$PL_{ir:off}$. This result shows a decrease of the PL signal with the IR excitation depending on the green excitation power.

With this study, we find the same results than with the MQW sample, which is the decrease of the global spectrum with the IR bias laser. While increasing the pump power excitation, a broadening of the ΔPL/PL spectrum is observed in the QD region, and positive two-step two-photon absorption appears in the WL and barrier spectral region.

4.4.5.3 Discussion

We first focus on the pump power excitation behaviour. The broadening observed in the QD with the increased pump power excitation can be interpreted as an increased carrier population and especially an excited states filling. Appearance of a TS-TPA in WL and barrier occurs at high pump irradiance, exactly as the luminescence in this region.

The central peaks of ΔPL/PL spectra are all at a higher wavelength than their corresponding PL peak. In other words, the intraband absorption is blueshifted in comparison with the PL spectra. This result was not expected. Indeed, Pr Sauvage and his team showed that bound to continuum absorption in InAs/GaAs QD decreases with $E_{\text{bound to continuum}}$, because of the decrease of the oscillator strength [153]. The oscillator strength in a semiconductor is proportional to the energy of the considered transition. Indeed, in analogy with QW, the bound to continuum transition energy decreases with the increase of the QD baseground, so should the intraband absorption efficiency [170]. On the other hand, it has been predicted that smaller QD would have a better intraband absorption and would increase the confinement of the carrier [171]. The FB cavity could be responsible for this effect: while enhancing the VB↔IB transition, the IB↔CB is decreased in the same time. If that is the case, enhancing the VB↔IB transition would not favour the highlighting of the IBSC effect. The curve also exhibits bound to continuum absorption in the WL, which can be compared to the one measured in the MQW sample.

To understand the spectral information of the intraband absorption efficiency, we consider the model proposed Figure 4.3.3-2.

The PL signal intensity in a QD can be approximated by:

$$I_{PL}(E) = B(E)n_I(E) \qquad (4.4\text{-}2.)$$

Where B is the radiative recombination rate, depending on the oscillator strength and therefore to the considered radiation energy, and n_I the population in the intermediate band. The difference between the PL without and with IR bias is:

$$\frac{\Delta_{I_{PL}(E)}}{I_{PL}(E)} = \frac{\Delta n_I}{n_I} \qquad (4.4\text{-}3.)$$

We consider now the following equations for the steady state population in the intermediate band in both cases:

$$\frac{dn_{I_{IR\,off}}}{dt} = 0 = \frac{n_c}{\tau_{CI}} - \frac{n_{I_{IR\,off}}}{\tau_{IV}} \tag{4.4-4.}$$

$$\frac{dn_{I_{IR\,on}}}{dt} = 0 = \frac{n_c}{\tau_{CI}} - \frac{n_{I_{IR\,on}}}{\tau_{IV}} - P \tag{4.4-5.}$$

The relaxation rates accounts for both radiative and non-radiative recombinations. P is the absorbed photon, proportional to the incident IR laser photons per pulses and to the intraband absorption coefficient:

$$P = \alpha_{IC}\, N_{IR,inc} \tag{4.4-6.}$$

where $N_{IR,inc}$ is the incident IR laser photons per pulses.

The intraband absorption coefficient can be written as a function of the IB occupation [39]:

$$\alpha_{IC} = f_I\, \alpha_{IC}^{max} = \frac{n_I}{D_I}\, \alpha_{IC}^{max} \tag{4.4-7.}$$

with D_I being the total density of states of the IB.

This leads to:

$$n_{I_{IR\,off}} = \frac{\tau_{IV}\, n_C}{\tau_{CI}} \tag{4.4-8.}$$

$$n_{I_{IR\,on}} = \frac{\tau_{IV} n_C}{\tau_{CI}} \left(\frac{D_I}{D_I + \tau_{IV}\, \alpha_{IC}^{max} N_{IR,inc}} \right) \tag{4.4-9.}$$

Finally:

$$\frac{\Delta_{I_{PL}(E)}}{I_{PL}(E)} = \frac{\Delta n_I}{n_I} = 1 - \frac{1}{1 + \frac{\tau_{IV}\, \alpha_{IC}^{max} N_{IR,inc}}{D_I}} \tag{4.4-10.}$$

From this equation, we can therefore isolate the parameter optimising the TS-TPA, in our experimental conditions. It appears that $\frac{\Delta_{I_{PL}(E)}}{I_{PL}(E)}$ is an increasing function of the radiative relaxation time, τ_{IV}, the intraband absorption coefficient, α_{IC}^{max}, and the IR laser excitation power. As the relaxation time is not dominated by non-radiative recombinations (cf. 4.4.2), the optical cavity reduces τ_{PL} and so does not help to evidence the TS-TPA. However, for an ideal IBSC working under AM1.5 spectrum, this cavity will help to fill the IB, which is a key point especially for QD-based IBSC where the VB $\rightarrow$ IB transition is weak.

The amplitude of ΔPL/PL curve is however not reliable. Our experimental setup introduced indeed significant uncertainty about the excitation power. This uncertainty has been reduced by multiple acquisition. The magnitude changed of about 50%, but the spectra had always the same shape and sign. Therefore we believe that the effect is real. In addition if this result was only due to a pump power variation, with such small changes the variation of the PL should be linear with the pump power excitation, resulting in induced variations spectrally constant, which is clearly not the case here.

In conclusion we have demonstrated a TS-TPA effect in our sample by PL measurement. This characterisation method is interesting as it gives a spectral information about this phenomenon, information that is not present in other TS-TPA characterisation methods. Nonetheless our unstable laser coupling was a source of uncertainty, and the setup has to be improved for reliable quantitative measures.

4.4.6 Hyperspectral measurements

We apply the procedure described in Sec4.2.2. We use a 532nm laser excitation up to 12000 suns and a Silicon CCD. Figure 4.4.6-1 shows the extracted Δμ.

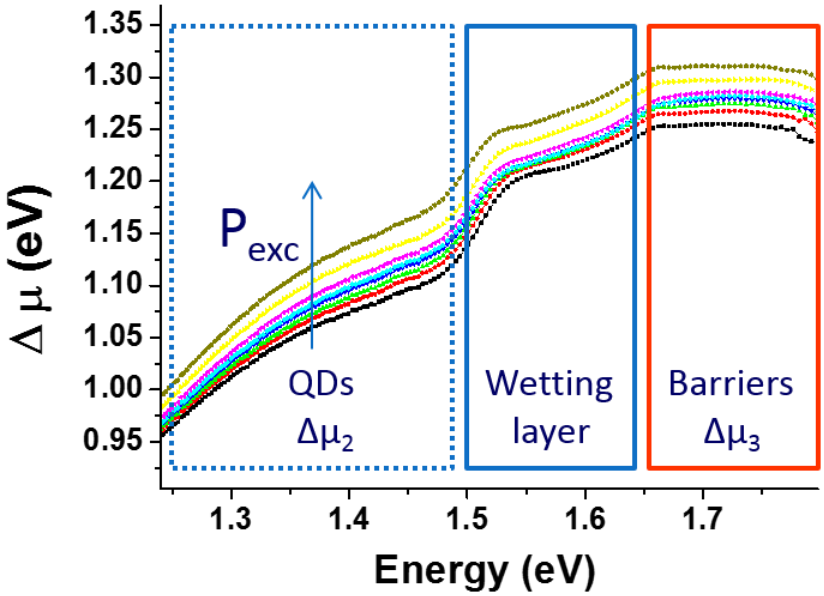

Figure 4.4.6-1: Excitation power study of the Δμ(E) in the structure. The region from where the luminescence is emitted are detailed.

We distinct three regions corresponding to the three transitions recorded implying the barrier, the Wetting Layer (WL) and the QD ensemble.

The barrier spectral region exhibit a constant Δμ as expected, and increasing the excitation power leads to a vertical translation of log(c).

The Δμ in the WL region is not a plateau, contrary to the analysis of the MQW case. This is however due to a spectral recovery between the luminescence of the barrier and of the WL. Here again, the $\Delta\mu_{WL}(P)$ is a linear function of log (c). This confirms the equilibrium between the WL carriers. Finally, the ΔΔμ between the barrier and the WL is around 50meV, close to the IB criteria. As the WL is a very thin well, the confinement is higher than in the wells of the MQW sample. This could reduce the thermal escape from the WL, and therefore lead to a QFL splitting between the WL and the barrier.

About the QD ensemble, we see that no plateau is reached. This could be because of the absorptivity of the QD is not valid. It was measured at very low irradiance whereas the PL measures has been done at high injection levels. From the shape of the different curves, it seems that the high energy part of the QD are in equilibrium: in this region, an increasing irradiance leads to a vertical translation of the $\Delta\mu(E)$. Therefore, even if we can't determine it, it seems that a common μ exists for the excited states of the QDs. Physically, this reflects that those states are less confined, resulting in a dominant thermal escape rate.

Upper limit of the $\Delta\mu$

We will now study the system at high irradiance. This approach is similar to the voltage recovery presented by Professor Luque et al. Indeed by measuring the barriers chemical potential in the case the QD are saturated, the thermionic transition from the CB to the IB becomes marginal, and so a significant $\Delta(\Delta\mu)$ will arise. Nonetheless, in the case where the QDs are saturated, two problems arise in the $\Delta\mu_{QD}$ calculation. First, the Boltzmann approximation is no longer valid, neither is the generalised Planck's law (EQ. (1.1-7.)). The second and most problematic issue, is that the absorption in QD region is null, making this law inappropriate. The barriers $\Delta\mu$ is however still accessible, and we will therefore focus only on the barrier and WL emission with the objective to prove that this $\Delta\mu$ reaches values that cannot be reached by the QDs. A simple upper bound for the $\Delta\mu$ would be the radiative open-circuit voltage, $V_{oc,\ rad}$, introduced in chapter 2, and depending on the EQE of the cell. But the lack of electrical contact made impossible the measurement of EQE. In the worse hypothesis it could be equal to the radiative transition of the WL, 1,55eV. Therefore, we consider here the mean bandgap energy of the QDs as the upper band. This upper band is a stronger proof than the $V_{oc,\ rad}$ value, especially because, in the case where a common $\Delta\mu$ exist in the QD, its value could even be majored by the lowest bandgap energy of the QD ensemble.

Figure 4.4.6-2 features the PL spectra and the results of the IBSC characterization by the Δμ.

The Δμ measured in the barrier is 1.49 eV, which is very close to the WL energy transition.

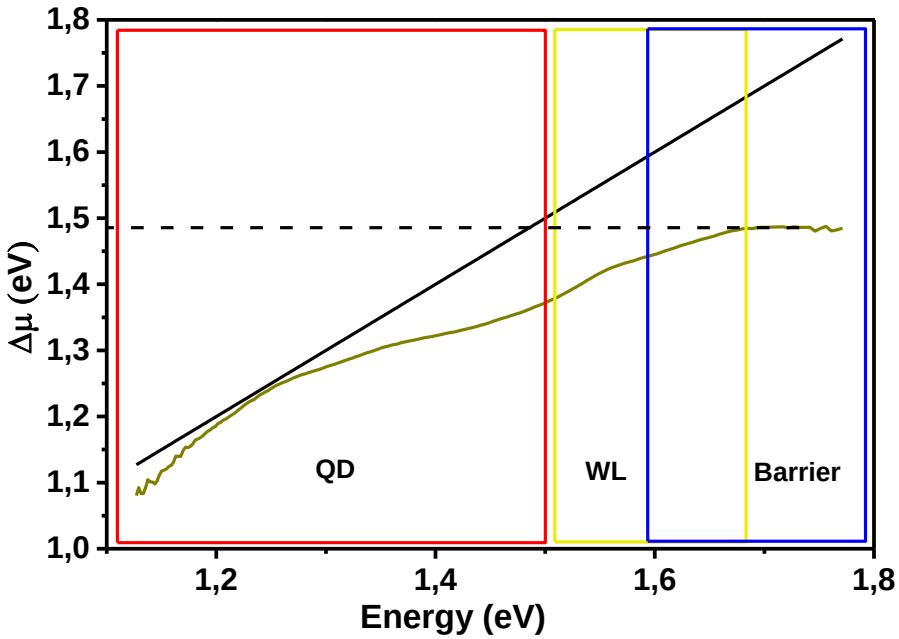

Figure 4.4.6-2 : Spectrally resolved QFLs splittings in the structure. The region from where the luminescence is emitted are detailed. The QFLs splitting between the barrier population and the valence band is almost equal to the WL transition energy. This figure exhibits an optical measure of a voltage recovery obtained with our sample at RT.

Discussion

The results here suggest that the carriers in the QD ensemble meet not chemical and thermal equilibrium, at least for the most confined states. In this case, we have to consider each QD as an isolated system with its own generalised Planck's law. For the excited states, the lower confinement allow for the carriers to be in equilibrium. Besides, a small QFL splitting exists between the WL and the barrier.

The voltage recovery approach give some interesting results: the Δμ exhibited in the barrier is very high, reaching almost the WL band gap energy. If it exists, the common Δμ in the QD should even be lower than the mean transition energy, 1.24eV. The ΔΔμ between the QD and the barrier would then reach the 250meV.

4.5 Conclusions

We have developed an all optical characterisation methods adapted to the two IBSCs key processes: the TS-TPA and the voltage preservation. The TS-TPA has been investigated through PL induced by a dual-beam laser excitation. The originality of this technics relies on the spectral information that is accessed. PL spectra also allow us to probe optically the voltage in the structure and especially to measure, whether or not a voltage gain exists compared to a single transition solar cells made with the IB material. We have then applied this method to a MQW and a MSQD based IBSCs material. Both candidates exhibited TS-TPA at room-temperature. The MQW sample has shown no voltage gain compared to a single transition solar cell based on the QW material. On the other hand the MSQD demonstrated a significant voltage gain at high concentration regime. This optical "voltage recovery" is a very interesting technic that can be applied to absorbers.

IBSCs efficiency depends highly on the fragile equilibrium of the generation and recombination rate in the device. In this sense, light management could help us to control this balance and therefore is a very interesting tool. We have studied the effect of a cavity increasing the VB ↔ IB transition that contribute to achieve TS-TPA efficiency by useful photofilling of the IB (photofilling by absorption from the VB in opposition to parasitic photofilling by non-radiative recombination from the CB). Adding a cavity enhancing the IB → CB would also be of great interest. It would indeed be needed to benefit the increased absorption in the QD region, and would help to achieve voltage preservation by increasing the difference of the QFLs in the QD and in the CB. Grow more confined QD-based systems, blocking the recombination from the CB to the IB (for example by energy band engineering using type-II QDs) are also solid leads towards efficient IBSCs).

Conclusion

This thesis deals with the multi-transition solar cells by studying two subband gap localised states materials: one highly mismatch alloy, GaAsPN, and one multi-stacked quantum dots heterostructure. These subband gap states give the possibility to tune the band gap energy or create two photon transitions inside a single the absorber.

In a first part, a radiance based introduction of the solar cell is presented. Links between radiances and electrical properties are pointed out. From this analysis, the thermodynamic limits of the single and multiple transition solar cells are derived and key mechanisms for multi-transition solar cells are identified. A universal optical characterisation method for probing electrical properties of solar cells is displayed. It mainly relies on a Hyperspectral Imager. This original tool allows for the measured PL intensity to be absolutely calibrated. This method is especially adapted to multi-transition solar cells, as it access the electrical performances of each transition. Finally it allows for the absorbers to be characterised. This is essential for third generation concepts, for which complete devices are not always available.

The first experimental part of my thesis was dedicated to the development of a GaAsPN based pin top cell lattice matched with a Silicon bottom cell. Numerical simulations have been carried out. It appeared that two main obstacles are to be tackle: the $\mu\tau$ product of the GaAsPN and the photocurrent barrier at GaAsPN/Gap-n interface. For the $\mu\tau$ product, we have seen that annealing and growth conditions could change dramatically this quantity. A rigorous statistical study has to be carried out in order to optimise these two processes. Optical

management could also be considered to reduce the absorber thickness. Concerning the photocurrent barrier, high doping value or substitution of GaP with AlGaP for the n-doped layer should suppress this problem. AlGaP would also help to passivate the interface. An optimised design has been found.

Based on this study, FOTON laboratory grew absorbers and pin diode. We have measured materials parameters, such as the absorption coefficient or the carrier lifetime that was not well referenced in the literature. Carrier dynamics has been studied by steady-state and time-resolved photoluminescence, with the conclusion that the GaAsPN we grew still suffer from multiple strongly localised states below the band gap, mainly due to N-clusters. This localisation decreases dramatically the electron mobility and prevents from a good carrier collection. Luminescence properties of the absorber is highly disturbed by those localised states, we have not been able to apply classical analysis. For example, high luminescence intensity and high open circuit voltage are not related, as well as carrier lifetime and short circuit current. We have demonstrated a state of the art GaAsPN top cell, with a conversion efficiency of 2.25%. With the conclusions of this thesis we are expecting a significant increase of this efficiency in the next months.

Finally, we have taken advantages of the strong carrier localisation: it allows for those states to be isolated from the conduction band, and therefore can be put to good use in an intermediate band solar cell. We have demonstrated an interesting behaviour of GaAsPN from this perspective: a two-step two photon absorption of about 0.1% at room temperature without a blocking layer.

In the last part of this work, quantum confined heterostructures for intermediate band solar cells have been studied. A quantitative optical characterisation method was developed and applied to a multiple quantum wells (MQW) and a multi-stacked quantum dots (MSQD) samples. This method gives access to the two key mechanisms of the intermediate band behaviour: the two-step two photon absorption (TS-TPA) and the voltage preservation, which reflect the electronic isolation of carriers in the intermediate band. Both candidates exhibited significant

TS-TPA at room temperature, whereas only the MSQD sample exhibited voltage preservation.

The TS-TPA was probed with a dual-beam excitation PL measurement, method that, compared with the existent technics, gives the spectral information of this mechanism. Effect of a Fabry-Perot cavity enhancing the absorption on QD has also been analysed. Even if this cavity is beneficial for the global TS-TPA, it has been found that using solely this cavity decreases the intraband absorption from the IB to the CB by an emptying effect of the IB. To tackle this effect, this cavity should be associated with one enhancing the IB↔VB transition. This way, the global TS-TPA would be increased. Besides, by increasing the Quasi-Fermi levels splittings between the IB and the CB, that second cavity is a promising lead to achieve voltage preservation.

PL intensity has been used to investigate this voltage preservation thanks to a Hyperspectral Imager. Combined with the generalised Planck's law, it gives access to the absolute value of the chemical potential of the different carrier populations. A discussion about the application modalities of the generalised Planck's law on the QD ensemble has been made. It appeared that, as the most confined carriers in the quantum dots are probably not in equilibrium, this law is unfortunately not applicable for this population. However, the barrier is well suited for this measurement, and an optical voltage recovery-like measurement is demonstrated for the MQSD at room temperature.

Bibliography

[1] MIT, "MIT Future of Solar Energy Study." .

[2] ADEME, "Vers un mix électrique 100% renouvelable en 2050." .

[3] "Neoen breaks ground on 300 MW French solar plant: pv-magazine." [Online]. Available: http://www.pv-magazine.com/news/details/beitrag/neoen-breaks-ground-on-300-mw-french-solar-plant_100017099/#axzz3eIbYRAlQ.

[4] "EDF va construire deux EPR en Angleterre - Le Point." [Online]. Available: http://www.lepoint.fr/economie/edf-devrait-construire-deux-epr-en-angleterre-17-10-2013-1744992_28.php.

[5] Fraunhofer ISE, "Current and future cost of photovoltaics: long-term scenarios for market development, system prices and LCOE of utility-scale pv systems."

[6] "Cheapest Solar Ever: Austin Energy Gets 1.2 Gigawatts of Solar Bids for Less Than 4 Cents : Greentech Media." [Online]. Available: http://www.greentechmedia.com/articles/read/cheapest-solar-ever-austin-energy-gets-1.2-gigawatts-of-solar-bids-for-less.

[7] IRENA, "Renewable Energy Technologies Cost Analysis SOLAR PV." .

[8] IAE, "PVPS report A Snapshot of Global_PV 1992-2013." .

[9] M. A. Green, K. Emery, Y. Hishikawa, W. Warta, and E. D. Dunlop, "Solar cell efficiency tables (Version 45): Solar cell efficiency tables," *Prog. Photovolt. Res. Appl.*, vol. 23, no. 1, pp. 1–9, Jan. 2015.

[10] A. S. Brown and M. A. Green, "Detailed balance limit for the series constrained two terminal tandem solar cell," *Phys. E Low-Dimens. Syst. Nanostructures*, vol. 14, no. 1–2, pp. 96–100, Apr. 2002.

[11] B. Browne, A. Ioannides, J. Connolly, K. Barnham, J. Roberts, R. Airey, G. Hill, G. Smekens, and J. Van Begin, "Tandem quantum well solar cells," presented at the Photovoltaic Specialists Conference, 2008. PVSC'08. 33rd IEEE, 2008, pp. 1–5.

[12] A. Freundlich and A. Alemu, "Multi quantum well multijunction solar cell for space applications," *Phys. Status Solidi C*, vol. 2, no. 8, pp. 2978–2981, May 2005.

[13] A. W. Walker, O. Theriault, J. F. Wheeldon, and K. Hinzer, "The Effects of Absorption and Recombination on Quantum Dot Multijunction Solar Cell Efficiency," *IEEE J. Photovolt.*, vol. 3, no. 3, pp. 1118–1124, Jul. 2013.

[14] M. Wolf, "Limitations and Possibilities for Improvement of Photovoltaic Solar Energy Converters: Part I: Considerations for Earth's Surface Operation," *Proc. IRE*, vol. 48, no. 7, pp. 1246–1263, Jul. 1960.

[15] Jean-François Guillemoles and S.Kettemann, "Limiting efficiencies of LDS intermediate band solar cells," 1995.

[16] A. Luque and A. Martí, "Increasing the Efficiency of Ideal Solar Cells by Photon Induced Transitions at Intermediate Levels," *Phys. Rev. Lett.*, vol. 78, no. 26, pp. 5014–5017, Jun. 1997.

[17] W. Shockley and H. J. Queisser, "Detailed Balance Limit of Efficiency of p-n Junction Solar Cells," *J. Appl. Phys.*, vol. 32, no. 3, p. 510, 1961.

[18] G. L. Araújo and A. Martí, "Absolute limiting efficiencies for photovoltaic energy conversion," *Sol. Energy Mater. Sol. Cells*, vol. 33, no. 2, pp. 213–240, Jun. 1994.

[19] J. Nelson, *The physics of solar cells*. London : River Edge, NJ: Imperial College Press ; Distributed by World Scientific Pub. Co, 2003.

[20] G. Lasher and F. Stern, "Spontaneous and Stimulated Recombination Radiation in Semiconductors," *Phys. Rev.*, vol. 133, no. 2A, pp. A553–A563, Jan. 1964.

[21] P. Wurfel, "The chemical potential of radiation," *J. Phys. C Solid State Phys.*, vol. 15, no. 18, p. 3967, 1982.

[22] W. Van Roosbroeck and W. Shockley, "Photon-radiative recombination of electrons and holes in germanium," *Phys. Rev.*, vol. 94, no. 6, p. 1558, 1954.

[23] P. Würfel, *Physics of solar cells: from basic principles to advanced concepts*, 2nd, updated and expanded ed. Weinheim: Wiley-VCH, 2009.

[24] L. Ferraioli, P. Maddalena, E. Massera, A. Parretta, M. A. Green, A. Wang, and J. Zhao, "Evidence for generalized Kirchhoff's law from angle-resolved electroluminescence of high efficiency silicon solar cells," *Appl. Phys. Lett.*, vol. 85, no. 13, p. 2484, 2004.

[25] K. Schick, E. Daub, S. Finkbeiner, and P. Würfel, "Verification of a generalized Planck law for luminescence radiation from silicon solar cells," *Appl. Phys. Solids Surf.*, vol. 54, no. 2, pp. 109–114, Feb. 1992.

[26] B. Feuerbacher and P. Wurfel, "Verification of a generalised Planck law by investigation of the emission from GaAs luminescent diodes," *J. Phys. Condens. Matter*, vol. 2, no. 16, pp. 3803–3810, Apr. 1990.

[27] A. Delamarre, L. Lombez, and J.-F. Guillemoles, "Contactless mapping of saturation currents of solar cells by photoluminescence," *Appl. Phys. Lett.*, vol. 100, no. 13, p. 131108, 2012.

[28] A. Delamarre, M. Paire, J.-F. Guillemoles, and L. Lombez, "Quantitative luminescence mapping of Cu(In, Ga)Se_2 thin-film solar cells," *Prog. Photovolt. Res. Appl.*, Dec. 2014.

[29] T. Trupke, P. Würfel, I. Uhlendorf, and I. Lauermann, "Electroluminescence of the Dye-Sensitized Solar Cell," *J. Phys. Chem. B*, vol. 103, no. 11, pp. 1905–1910, Mar. 1999.

[30] T. Trupke, R. A. Bardos, M. D. Abbott, and J. E. Cotter, "Suns-photoluminescence: Contactless determination of current-voltage characteristics of silicon wafers," *Appl. Phys. Lett.*, vol. 87, no. 9, p. 093503, 2005.

[31] G. Smestad and H. Ries, "Luminescence and current-voltage characteristics of solar cells and optoelectronic devices," *Sol. Energy Mater. Sol. Cells*, vol. 25, no. 1–2, pp. 51–71, Jan. 1992.

[32] A. Lebris, "Etude de faisablilité de dispositifs photovoltaiques à porteurs chauds: conception, modélisation, caractérisation."

[33] Tibbits, "NEW EFFICIENCY FRONTIERS WITH WAFER-BONDED MULTI-JUNCTION SOLAR CELLS," *29th Eur. PV Sol. Energy Conf. Exhib.*, Sep. 2014.

[34] S. Almosni, “GROWTH, STRUCTURAL AND ELECTRO-OPTICAL PROPERTIES OF GAP/SI AND GAASPN/GAP SINGLE JUNCTIONS FOR LATTICE-MATCHED TANDEM SOLAR CELLS ON SILICON.”

[35] A. D. Vos, “Detailed balance limit of the efficiency of tandem solar cells,” *J. Phys. Appl. Phys.*, vol. 13, no. 5, pp. 839–846, May 1980.

[36] S. P. Bremner, M. Y. Levy, and C. B. Honsberg, “Analysis of tandem solar cell efficiencies under AM1.5G spectrum using a rapid flux calculation method,” *Prog. Photovolt. Res. Appl.*, vol. 16, no. 3, pp. 225–233, May 2008.

[37] C. H. Henry, “Limiting efficiencies of ideal single and multiple energy gap terrestrial solar cells,” *J. Appl. Phys.*, vol. 51, no. 8, p. 4494, 1980.

[38] “http://www.pveducation.org/pvcdrom/solar-cell-operation/tandem-cells.” [Online]. Available: http://www.pveducation.org/pvcdrom/solar-cell-operation/tandem-cells.

[39] Y. Okada, N. J. Ekins-Daukes, T. Kita, R. Tamaki, M. Yoshida, A. Pusch, O. Hess, C. C. Phillips, D. J. Farrell, K. Yoshida, N. Ahsan, Y. Shoji, T. Sogabe, and J.-F. Guillemoles, “Intermediate band solar cells: Recent progress and future directions,” *Appl. Phys. Rev.*, vol. 2, no. 2, p. 021302, Jun. 2015.

[40] S. P. Bremner, M. Y. Levy, and C. B. Honsberg, “Limiting efficiency of an intermediate band solar cell under a terrestrial spectrum,” *Appl. Phys. Lett.*, vol. 92, no. 17, p. 171110, 2008.

[41] A. S. Brown, M. A. Green, and R. P. Corkish, “Limiting efficiency for a multi-band solar cell containing three and four bands,” *Phys. E Low-Dimens. Syst. Nanostructures*, vol. 14, no. 1–2, pp. 121–125, Apr. 2002.

[42] J. Lee and C. B. Honsberg, “The thermodynamic limits of tandem photovoltaic devices with intermediate band,” 2012, p. 82560Q–82560Q–12.

[43] A. Lin and J. Phillips, “Resolving spectral overlap issue of intermediate band solar cells using non-uniform sub-bandgap state filling,” *Prog. Photovolt. Res. Appl.*, p. n/a–n/a, Jan. 2013.

[44] A. Martí, E. Antolín, P. García Linares, I. Ramiro, I. Artacho, E. López, E. Hernández, M. J. Mendes, A. Mellor, I. Tobías, D. Fuertes Marrón, C. Tablero, A. B. Cristóbal, C. G. Bailey, M. Gonzalez, M. Yakes, M. P. Lumb, R. Walters, and A. Luque, “Six not-so-easy pieces in intermediate band solar cell research,” *J. Photonics Energy*, vol. 3, no. 1, p. 031299, Sep. 2013.

[45] L. Lombez, D. Ory, M. Paire, A. Delamarre, G. El Hajje, and J. F. Guillemoles, “Micrometric investigation of external quantum efficiency in microcrystalline CuInGa(S,Se)2 solar cells,” *Thin Solid Films*, vol. 565, pp. 32–36, Aug. 2014.

[46] U. Rau, “Reciprocity relation between photovoltaic quantum efficiency and electroluminescent emission of solar cells,” *Phys. Rev. B*, vol. 76, no. 8, Aug. 2007.

[47] Z. Földes-Papp, U. Demel, and G. P. Tilz, “Laser scanning confocal fluorescence microscopy: an overview,” *Int. Immunopharmacol.*, vol. 3, no. 13–14, pp. 1715–1729, Dec. 2003.

[48] J. B. Pawley, Ed., *Handbook of biological confocal microscopy*, 3rd ed. New York, NY: Springer, 2006.

[49] C. L. Smith, “Basic Confocal Microscopy,” in *Current Protocols in Molecular Biology*, F. M. Ausubel, R. Brent, R. E. Kingston, D. D. Moore, J. G. Seidman, J. A. Smith, and K. Struhl, Eds. Hoboken, NJ, USA: John Wiley & Sons, Inc., 2008.

[50] J. W. Lichtman and J.-A. Conchello, “Fluorescence microscopy,” *Nat. Methods*, vol. 2, no. 12, pp. 910–919, Dec. 2005.

[51] “Duke University Light Microscopy Core Facility - Basic introduction to microscopy: confocal microscopes.” [Online]. Available: http://microscopy.duke.edu/learn/introtomicroscopy/confocals.html.

[52] E. Kuokstis, C. Q. Chen, M. E. Gaevski, W. H. Sun, J. W. Yang, G. Simin, M. Asif Khan, H. P. Maruska, D. W. Hill, M. C. Chou, J. J. Gallagher, and B. Chai, “Polarization effects in photoluminescence of C- and M-plane GaN/AlGaN multiple quantum wells,” *Appl. Phys. Lett.*, vol. 81, no. 22, p. 4130, 2002.

[53] W. J. Salcedo, F. J. Ramirez Fernandez, and J. C. Rubim, “Polarization effects on the Raman and photoluminescence spectra of porous silicon layers,” *J. Raman Spectrosc.*, vol. 30, no. 1, pp. 29–36, Jan. 1999.

[54] S. Ostapenko, I. Tarasov, J. P. Kalejs, C. Haessler, and E.-U. Reisner, “Defect monitoring using scanning photoluminescence spectroscopy in multicrystalline silicon wafers,” *Semicond. Sci. Technol.*, vol. 15, no. 8, pp. 840–848, Aug. 2000.

[55] “Princeton Instruments - Acton Series - Spectrographs / Monochromators.” [Online]. Available: http://www.princetoninstruments.com/products/spec/actonseries/dsheet.aspx.

[56] P. Y. Yu and M. Cardona, *Fundamentals of semiconductors: physics and materials properties ; with 52 tables and 116 problems*, 3., rev. and enl. ed., 3., corr. print. Berlin: Springer, 2005.

[57] R. Heitz, I. Mukhametzhanov, A. Madhukar, A. Hoffmann, and D. Bimberg, “Temperature dependent optical properties of self-organized InAs/GaAs quantum dots,” *J. Electron. Mater.*, vol. 28, no. 5, pp. 520–527, May 1999.

[58] L. Wang and N. C. Giles, “Temperature dependence of the free-exciton transition energy in zinc oxide by photoluminescence excitation spectroscopy,” *J. Appl. Phys.*, vol. 94, no. 2, p. 973, 2003.

[59] R. A. Schultz, T. Nielsen, J. R. Zavaleta, R. Ruch, R. Wyatt, and H. R. Garner, “Hyperspectral imaging: A novel approach for microscopic analysis,” *Cytometry*, vol. 43, no. 4, pp. 239–247, Apr. 2001.

[60] P. R. Edwards, R. W. Martin, K. P. O’Donnell, and I. M. Watson, “Simultaneous composition mapping and hyperspectral cathodoluminescence imaging of InGaN epilayers,” *Phys. Status Solidi C*, vol. 0, no. 7, pp. 2474–2477, Dec. 2003.

[61] M. P. Peloso, J. Sern Lew, T. Trupke, M. Peters, R. Utama, and A. G. Aberle, “Evaluating the electrical properties of silicon wafer solar cells using hyperspectral imaging of luminescence,” *Appl. Phys. Lett.*, vol. 99, no. 22, p. 221915, 2011.

[62] E. Olsen and A. S. Flø, "Spectral and spatially resolved imaging of photoluminescence in multicrystalline silicon wafers," *Appl. Phys. Lett.*, vol. 99, no. 1, p. 011903, 2011.

[63] Q. Li, W. Wang, C. Ma, and Z. Zhu, "Detection of physical defects in solar cells by hyperspectral imaging technology," *Opt. Laser Technol.*, vol. 42, no. 6, pp. 1010–1013, Sep. 2010.

[64] A. Delamarre, "Development of luminescence based characterisation methods for solar cells," UPMC.

[65] A. Delamarre, "Characterization of solar cells using electroluminescence and photoluminescence hyperspectral images," *J. Photonics Energy*, vol. 2, no. 1, p. 027004, Jul. 2012.

[66] G. Jaschke, R. Averbeck, L. Geelhaar, and H. Riechert, "Low threshold InGaAsN/GaAs lasers beyond 1500nm," *J. Cryst. Growth*, vol. 278, no. 1–4, pp. 224–228, May 2005.

[67] N. Tansu, N. J. Kirsch, and L. J. Mawst, "Low-threshold-current-density 1300-nm dilute-nitride quantum well lasers," *Appl. Phys. Lett.*, vol. 81, no. 14, p. 2523, 2002.

[68] O. Okhotnikov, A. Grudinin, and M. Pessa, "Ultra-fast fibre laser systems based on SESAM technology: new horizons and applications," *New J. Phys.*, vol. 6, pp. 177–177, Nov. 2004.

[69] S. Tomic, E. P. O'Reilly, R. Fehse, S. J. Sweeney, A. R. Adams, A. D. Andreev, S. A. Choulis, T. J. C. Hosea, and H. Riechert, "Theoretical and experimental analysis of 1.3-µm InGaAsN/GaAs lasers," *IEEE J. Sel. Top. Quantum Electron.*, vol. 9, no. 5, pp. 1228–1238, Sep. 2003.

[70] S. R. Bank, H. Bae, L. L. Goddard, H. B. Yuen, M. A. Wistey, R. Kudrawiec, and J. S. Harris, "Recent Progress on 1.55- $\mu{\hbox {m}}$ Dilute-Nitride Lasers," *IEEE J. Quantum Electron.*, vol. 43, no. 9, pp. 773–785, Sep. 2007.

[71] S. Calvez, J.-M. Hopkins, S. A. Smith, A. H. Clark, R. Macaluso, H. D. Sun, M. D. Dawson, T. Jouhti, M. Pessa, K. Gundogdu, K. C. Hall, and T. F. Boggess, "GaInNAs/GaAs Bragg-mirror-based structures for novel 1.3µm device applications," *J. Cryst. Growth*, vol. 268, no. 3–4, pp. 457–465, Aug. 2004.

[72] M. Wiemer, V. Sabnis, and H. Yuen, "43.5% efficient lattice matched solar cells," 2011, pp. 810804–810804–5.

[73] V. Sabnis, H. Yuen, and M. Wiemer, "High-efficiency multijunction solar cells employing dilute nitrides," 2012, pp. 14–19.

[74] D. B. Jackrel, S. R. Bank, H. B. Yuen, M. A. Wistey, J. S. Harris, A. J. Ptak, S. W. Johnston, D. J. Friedman, and S. R. Kurtz, "Dilute nitride GaInNAs and GaInNAsSb solar cells by molecular beam epitaxy," *J. Appl. Phys.*, vol. 101, no. 11, p. 114916, 2007.

[75] J. Chamings, S. Ahmed, A. R. Adams, S. J. Sweeney, V. A. Odnoblyudov, C. W. Tu, B. Kunert, and W. Stolz, "Band anti-crossing and carrier recombination in dilute nitride phosphide based lasers and light emitting diodes," *Phys. Status Solidi B*, vol. 246, no. 3, pp. 527–531, Mar. 2009.

[76] M. Henini, Ed., *Dilute nitride semiconductors*, 1. ed. Amsterdam [u.a]: Elsevier, 2005.

[77] A. Erol, Ed., *Dilute III-V nitride semiconductors and material systems: physics and technology*. Berlin: Springer, 2008.

[78] Geisz J F and Friedman D J, "III-N-V sc for solar application." [Online]. Available: http://iopscience.iop.org.accesdistant.upmc.fr/0268-1242/17/8/305/pdf/0268-1242_17_8_305.pdf. [Accessed: 08-Jun-2012].

[79] A. Martí and G. L. Araújo, "Limiting efficiencies for photovoltaic energy conversion in multigap systems," *Sol. Energy Mater. Sol. Cells*, vol. 43, no. 2, pp. 203–222, Sep. 1996.

[80] S. R. Kurtz, P. Faine, and J. M. Olson, "Modeling of two-junction, series-connected tandem solar cells using top-cell thickness as an adjustable parameter," *J. Appl. Phys.*, vol. 68, no. 4, p. 1890, 1990.

[81] P. Kent and A. Zunger, "Evolution of III-V Nitride Alloy Electronic Structure: The Localized to Delocalized Transition," *Phys. Rev. Lett.*, vol. 86, no. 12, pp. 2613–2616, Mar. 2001.

[82] P. R. C. Kent and A. Zunger, "Theory of electronic structure evolution in GaAsN and GaPN alloys," *Phys. Rev. B*, vol. 64, no. 11, Aug. 2001.

[83] W. Shan, W. Walukiewicz, J. W. Ager, E. E. Haller, J. F. Geisz, D. J. Friedman, J. M. Olson, and S. R. Kurtz, "Band Anticrossing in GaInNAs Alloys," *Phys. Rev. Lett.*, vol. 82, no. 6, pp. 1221–1224, Feb. 1999.

[84] W. Shan, W. Walukiewicz, K. M. Yu, J. Wu, J. W. Ager, E. E. Haller, H. P. Xin, and C. W. Tu, "Nature of the fundamental band gap in GaN[sub x]P[sub 1−x] alloys," *Appl. Phys. Lett.*, vol. 76, no. 22, p. 3251, 2000.

[85] J. Perkins, A. Mascarenhas, J. Geisz, and D. Friedman, "Conduction-band-resonant nitrogen-induced levels in GaAs 1− x N x with x< 0.03," *Phys. Rev. B*, vol. 64, no. 12, p. 121301, 2001.

[86] A. Mascarenhas, M. Seong, S. Yoon, J. Verley, J. Geisz, and M. Hanna, "Evolution of electronic states in GaAs 1− x N x probed by resonant Raman spectroscopy," *Phys. Rev. B*, vol. 68, no. 23, p. 233201, 2003.

[87] J. Wu, W. Walukiewicz, K. M. Yu, J. W. Ager III, E. E. Haller, Y. G. Hong, H. P. Xin, and C. W. Tu, "Band Anticrossing in GaP N x Alloys."

[88] S. Adachi, *Properties of semiconductor alloys: group-IV, III-V and II-VI semiconductors*. Chichester, U.K: Wiley, 2009.

[89] K. Yamane, N. Urakami, H. Sekiguchi, and A. Wakahara, "III–V-N compounds for multi-junction solar cells on Si," 2014, pp. 2792–2796.

[90] Y. J. Kuang, K. M. Yu, R. Kudrawiec, A. V. Luce, M. Ting, W. Walukiewicz, and C. W. Tu, "GaNAsP: An intermediate band semiconductor grown by gas-source molecular beam epitaxy," *Appl. Phys. Lett.*, vol. 102, no. 11, p. 112105, 2013.

[91] D. B. Jackrel, S. R. Bank, H. B. Yuen, M. A. Wistey, J. S. Harris, A. J. Ptak, S. W. Johnston, D. J. Friedman, and S. R. Kurtz, "Dilute nitride GaInNAs and GaInNAsSb solar cells by molecular beam epitaxy," *J. Appl. Phys.*, vol. 101, no. 11, p. 114916, 2007.

[92] A. V. Shah and C. Ballif, Eds., *Thin-film silicon solar cells*. Lausanne: EPFL Press, 2010.

[93] F. Meillaud, A. Shah, C. Droz, E. Vallat-Sauvain, and C. Miazza, "Efficiency limits for single-junction and tandem solar cells," *Sol. Energy Mater. Sol. Cells*, vol. 90, no. 18–19, pp. 2952–2959, Nov. 2006.

[94] Ioffe, "Physical properties of semiconductors." [Online]. Available: http://www.ioffe.ru/SVA/NSM/Semicond/index.html.

[95] A. I. Baranov, A. S. Gudovskikh, E. V. Nikitina, and A. Y. Egorov, "Photoelectric properties of solar cells based on GaPNAs/GaP heterostructures," *Tech. Phys. Lett.*, vol. 39, no. 12, pp. 1117–1120, Dec. 2013.

[96] A. Aho, A. Tukiainen, V. Polojärvi, J. Salmi, and M. Guina, "High current generation in dilute nitride solar cells grown by molecular beam epitaxy," 2013, p. 86201I.

[97] F. Urbach, "The Long-Wavelength Edge of Photographic Sensitivity and of the Electronic Absorption of Solids," *Phys. Rev.*, vol. 92, no. 5, pp. 1324–1324, Dec. 1953.

[98] H. Tang, F. Lévy, H. Berger, and P. E. Schmid, "Urbach tail of anatase TiO 2," *Phys. Rev. B*, vol. 52, no. 11, pp. 7771–7774, Sep. 1995.

[99] R. J. Potter, S. Mazzucato, N. Balkan, M. J. Adams, P. R. Chalker, T. B. Joyce, and T. J. Bullough, "Optical characterization of GaInNAs," 2001, pp. 638–644.

[100] A. Biswas, B. S. Yadav, D. Bhattacharyya, N. K. Sahoo, S. S. Major, and R. S. Srinivasa, "Spectroscopic ellipsometry studies of reactively sputtered nitrogen-rich GaAsN films," *J. Non-Cryst. Solids*, vol. 357, no. 18, pp. 3293–3300, Sep. 2011.

[101] F. Benkabou, J. P. Becker, M. Certier, and H. Aourag, "Calculation of electronic and optical properties of zinc blende GaP1−xNx," *Superlattices Microstruct.*, vol. 23, no. 2, pp. 453–465, Feb. 1998.

[102] S. Mitsuyoshi, K. Umeno, Y. Furukawa, N. Urakami, A. Wakahara, and H. Yonezu, "Electrical and luminescence properties of Mg-doped p-type GaPN grown by molecular beam epitaxy," *Phys. Status Solidi C*, vol. 7, no. 10, pp. 2498–2501, Oct. 2010.

[103] L. Pavesi and M. Ceschini, "Stretched-exponential decay of the luminescence in porous silicon," *Phys. Rev. B*, vol. 48, no. 23, pp. 17625–17628, Dec. 1993.

[104] G. Pfister and H. Scher, "Dispersive (non-Gaussian) transient transport in disordered solids," *Adv. Phys.*, vol. 27, no. 5, pp. 747–798, 1978.

[105] H. Scher, M. F. Shlesinger, and J. T. Bendler, "Time-scale invariance in transport and relaxation," *Phys Today*, vol. 44, no. 1, pp. 26–34, 1991.

[106] R. K. Ahrenkiel, S. W. Johnston, B. M. Keyes, D. J. Friedman, and S. M. Vernon, "Transport properties of GaAs[sub 1−x]N[sub x] thin films grown by metalorganic chemical vapor deposition," *Appl. Phys. Lett.*, vol. 77, no. 23, p. 3794, 2000.

[107] Y. A. Makhnovskii, A. M. Berezhkovskii, D.-Y. Yang, S.-Y. Sheu, and S. H. Lin, "Trapping by clusters of traps," *Phys. Rev. E*, vol. 61, no. 6, p. 6302, 2000.

[108] X. D. Luo, J. S. Huang, Z. Y. Xu, C. L. Yang, J. Liu, W. K. Ge, Y. Zhang, A. Mascarenhas, H. P. Xin, and C. W. Tu, "Alloy states in dilute GaAs[sub 1−x]N[sub x] alloys (x<1%)," *Appl. Phys. Lett.*, vol. 82, no. 11, p. 1697, 2003.

[109] B. Q. Sun, M. Gal, Q. Gao, H. H. Tan, and C. Jagadish, "On the nature of radiative recombination in GaAsN," *Appl. Phys. Lett.*, vol. 81, no. 23, p. 4368, 2002.

[110] X. D. Luo, Z. Y. Xu, W. K. Ge, Z. Pan, L. H. Li, and Y. W. Lin, "Photoluminescence properties of a GaN[sub 0.015]As[sub 0.985]/GaAs single quantum well under short pulse excitation," *Appl. Phys. Lett.*, vol. 79, no. 7, p. 958, 2001.

[111] J. Miguel-Sánchez, A. Guzmán, J. M. Ulloa, A. Hierro, and E. Muñoz, "Effect of nitrogen on the optical properties of InGaAsN p-i-n structures grown on misoriented (111)B GaAs substrates," *Appl. Phys. Lett.*, vol. 84, no. 14, p. 2524, 2004.

[112] D. S. H. Chan, V. K. S. Ong, and J. C. H. Phang, "A direct method for the extraction of diffusion length and surface recombination velocity from an EBIC line scan: planar junction configuration," *IEEE Trans. Electron Devices*, vol. 42, no. 5, pp. 963–968, May 1995.

[113] Z. Z. Bandić, P. M. Bridger, E. C. Piquette, and T. C. McGill, "Minority carrier diffusion length and lifetime in GaN," *Appl. Phys. Lett.*, vol. 72, no. 24, p. 3166, 1998.

[114] C. Donolato, "Evaluation of diffusion lengths and surface recombination velocities from electron beam induced current scans," *Appl. Phys. Lett.*, vol. 43, no. 1, p. 120, 1983.

[115] W. Gärtner, "Depletion-Layer Photoeffects in Semiconductors," *Phys. Rev.*, vol. 116, no. 1, pp. 84–87, Oct. 1959.

[116] D. Paget, F. Cadiz, A. C. H. Rowe, F. Moreau, S. Arscott, and E. Peytavit, "Imaging ambipolar diffusion of photocarriers in GaAs thin films," *J. Appl. Phys.*, vol. 111, no. 12, p. 123720, 2012.

[117] S. B. Zhang and S.-H. Wei, "Nitrogen Solubility and Induced Defect Complexes in Epitaxial GaAs:N," *Phys. Rev. Lett.*, vol. 86, no. 9, pp. 1789–1792, Feb. 2001.

[118] R. Scheer and H.-W. Schock, *Chalcogenide photovoltaics: physics, technologies, and thin film devices*. Weinheim: Wiley-VCH, 2011.

[119] K. Volz, D. Lackner, I. Németh, B. Kunert, W. Stolz, C. Baur, F. Dimroth, and A. W. Bett, "Optimization of annealing conditions of (GaIn)(NAs) for solar cell applications," *J. Cryst. Growth*, vol. 310, no. 7–9, pp. 2222–2228, Apr. 2008.

[120] A. Utsumi, H. Yonezu, Y. Furukawa, K. Momose, and K. Kuroki, "Increase in luminescence efficiency of GaPN layers by thermal annealing," *Phys. Status Solidi C*, vol. 0, no. 7, pp. 2741–2744, Dec. 2003.

[121] R. Mouillet, L.-A. de Vaulchier, E. Deleporte, Y. Guldner, L. Travers, and J.-C. Harmand, "Role of nitrogen in the mobility drop of electrons in modulation-doped GaAsN/AlGaAs heterostructures," *Solid State Commun.*, vol. 126, no. 6, pp. 333–337, May 2003.

[122] Y. Jin, R. M. Jock, H. Cheng, Y. He, A. M. Mintarov, Y. Wang, C. Kurdak, J. L. Merz, and R. S. Goldman, "Influence of N interstitials on the electronic properties of GaAsN alloys," *Appl. Phys. Lett.*, vol. 95, no. 6, p. 062109, 2009.

[123] D. Kwon, R. J. Kaplar, S. A. Ringel, A. A. Allerman, S. R. Kurtz, and E. D. Jones, "Deep levels in p-type InGaAsN lattice matched to GaAs," *Appl. Phys. Lett.*, vol. 74, no. 19, p. 2830, 1999.

[124] Y. Zhang, A. Mascarenhas, J. F. Geisz, H. P. Xin, and C. W. Tu, "Discrete and continuous spectrum of nitrogen-induced bound states in heavily doped GaAs 1 − x N x," *Phys. Rev. B*, vol. 63, no. 8, Feb. 2001.

[125] H. Grüning, L. Chen, T. Hartmann, P. J. Klar, W. Heimbrodt, F. Höhnsdorf, J. Koch, and W. Stolz, "Optical Spectroscopic Studies of N-Related Bands in Ga(N,As)," *Phys. Status Solidi B*, vol. 215, no. 1, pp. 39–45, Sep. 1999.

[126] S. Francoeur, S. A. Nikishin, C. Jin, Y. Qiu, and H. Temkin, "Excitons bound to nitrogen clusters in GaAsN," *Appl. Phys. Lett.*, vol. 75, no. 11, p. 1538, 1999.

[127] H. Jussila, K. M. Yu, J. Kujala, F. Tuomisto, S. Nagarajan, J. Lemettinen, T. Huhtio, T. O. Tuomi, H. Lipsanen, and M. Sopanen, "Substitutionality of nitrogen atoms and formation of nitrogen complexes and point defects in GaPN alloys," *J. Phys. Appl. Phys.*, vol. 47, no. 7, p. 075106, Feb. 2014.

[128] T. Niebling, T. Lapp, J. Kampmann, P. J. Klar, W. Heimbrodt, B. Kunert, K. Volz, and W. Stolz, "Excitation transfer between extended band states and N-related localized states in with x up to 1%," *Phys. E Low-Dimens. Syst. Nanostructures*, vol. 32, no. 1–2, pp. 222–225, May 2006.

[129] I. A. Buyanova, W. M. Chen, G. Pozina, J. P. Bergman, B. Monemar, H. P. Xin, and C. W. Tu, "Mechanism for low-temperature photoluminescence in GaNAs/GaAs structures grown by molecular-beam epitaxy," *Appl. Phys. Lett.*, vol. 75, no. 4, p. 501, 1999.

[130] J. Wong and M. Green, "From junction to terminal: Extended reciprocity relations in solar cell operation," *Phys. Rev. B*, vol. 85, no. 23, Jun. 2012.

[131] A.-M. Gonçalves, M. Bouttemy, O. El Ali, A. Eb, C. Mathieu, J. Vigneron, A. Etcheberry, R. White, and P. Mack, "An ARXPS study of the passivating layer formed on III-V surface by an innovative anodic treatment in liquid ammonia," *Surf. Interface Anal.*, vol. 42, no. 6–7, pp. 775–778, May 2010.

[132] A.-M. Gonçalves, C. Mathieu, and A. Etcheberry, "Electrochemical Comparisons between GaAs and InP in Liquid Ammonia regarding the Anodic Passivation Process," *J. Electrochem. Soc.*, vol. 159, no. 2, p. C97, 2012.

[133] K. M. Yu, W. Walukiewicz, J. W. Ager, D. Bour, R. Farshchi, O. D. Dubon, S. X. Li, I. D. Sharp, and E. E. Haller, "Multiband GaNAsP quaternary alloys," *Appl. Phys. Lett.*, vol. 88, no. 9, p. 092110, 2006.

[134] K. M. Yu, W. Walukiewicz, J. Wu, W. Shan, J. W. Beeman, M. A. Scarpulla, O. D. Dubon, and P. Becla, "Diluted II-VI Oxide Semiconductors with Multiple Band Gaps," *Phys. Rev. Lett.*, vol. 91, no. 24, Dec. 2003.

[135] N. López, L. A. Reichertz, K. M. Yu, K. Campman, and W. Walukiewicz, "Engineering the Electronic Band Structure for Multiband Solar Cells," *Phys. Rev. Lett.*, vol. 106, no. 2, Jan. 2011.

[136] N. Ahsan, N. Miyashita, M. M. Islam, K. M. Yu, W. Walukiewicz, and Y. Okada, "Effect of Sb on GaNAs Intermediate Band Solar Cells," *IEEE J. Photovolt.*, vol. 3, no. 2, pp. 730–736, Apr. 2013.

[137] H. Jussila, P. Kivisaari, J. Lemettinen, T. Tanaka, and M. Sopanen, "Two-Photon Absorption in GaAs 1 − x − y P y N x Intermediate-Band Solar Cells," *Phys. Rev. Appl.*, vol. 3, no. 5, May 2015.

[138] A. Z. M. T. Islam, T. Hanaoka, K. Onabe, S. Yagi, N. Kamata, and H. Yaguchi, "Direct Evidence of Carrier Excitation from Intermediate Band States in GaPN by Two-Wavelength Excited Photoluminescence," *Appl. Phys. Express*, vol. 6, no. 9, p. 092401, Sep. 2013.

[139] Y. Okada, T. Morioka, K. Yoshida, R. Oshima, Y. Shoji, T. Inoue, and T. Kita, "Increase in photocurrent by optical transitions via intermediate quantum states in direct-doped InAs/GaNAs strain-compensated quantum dot solar cell," *J. Appl. Phys.*, vol. 109, no. 2, p. 024301, 2011.

[140] N. Ahsan, N. Miyashita, M. Monirul Islam, K. Man Yu, W. Walukiewicz, and Y. Okada, "Two-photon excitation in an intermediate band solar cell structure," *Appl. Phys. Lett.*, vol. 100, no. 17, p. 172111, 2012.

[141] P. G. Linares, A. Martí, E. Antolín, C. D. Farmer, Í. Ramiro, C. R. Stanley, and A. Luque, "Voltage recovery in intermediate band solar cells," *Sol. Energy Mater. Sol. Cells*, vol. 98, pp. 240–244, Mar. 2012.

[142] A. Martí, E. Antolín, P. G. Linares, and A. Luque, "Understanding experimental characterization of intermediate band solar cells," *J. Mater. Chem.*, vol. 22, no. 43, p. 22832, 2012.

[143] C. G. Bailey, D. V. Forbes, R. P. Raffaelle, and S. M. Hubbard, "Near 1 V open circuit voltage InAs/GaAs quantum dot solar cells," *Appl. Phys. Lett.*, vol. 98, no. 16, p. 163105, 2011.

[144] I. Ramiro, A. Marti, E. Antolin, and A. Luque, "Review of Experimental Results Related to the Operation of Intermediate Band Solar Cells," *IEEE J. Photovolt.*, vol. 4, no. 2, pp. 736–748, Mar. 2014.

[145] A. Martí, E. Antolín, C. Stanley, C. Farmer, N. López, P. Díaz, E. Cánovas, P. Linares, and A. Luque, "Production of Photocurrent due to Intermediate-to-Conduction-Band Transitions: A Demonstration of a Key Operating Principle of the Intermediate-Band Solar Cell," *Phys. Rev. Lett.*, vol. 97, no. 24, Dec. 2006.

[146] M. Sugiyama, Y. Wang, K. Watanabe, T. Morioka, Y. Okada, and Y. Nakano, "Photocurrent Generation by Two-Step Photon Absorption With Quantum-Well Superlattice Cell," *IEEE J. Photovolt.*, vol. 2, no. 3, pp. 298–302, Jul. 2012.

[147] Y. Shoji, K. Akimoto, and Y. Okada, "Optical properties of multi-stacked InGaAs/GaNAs quantum dot solar cell fabricated on GaAs (311)B substrate," *J. Appl. Phys.*, vol. 112, no. 6, p. 064314, 2012.

[148] A. Luque, A. Martí, N. López, E. Antolín, E. Cánovas, C. Stanley, C. Farmer, L. J. Caballero, L. Cuadra, and J. L. Balenzategui, "Experimental analysis of the quasi-Fermi level split in quantum dot intermediate-band solar cells," *Appl. Phys. Lett.*, vol. 87, no. 8, p. 083505, 2005.

[149] A. A. Abouelsaood, M. Y. Ghannam, and J. Poortmans, "On the reported experimental evidence for the quasi-Fermi level split in quantum-dot intermediate-band solar cells: Quasi-Fermi level split in quantum-dot IBSCs," *Prog. Photovolt. Res. Appl.*, vol. 21, no. 2, pp. 209–216, Mar. 2013.

[150] I. Ramiro, E. Antolín, P. G. Linares, E. Hernández, A. Martí, A. Luque, C. D. Farmer, and C. R. Stanley, "Application of photoluminescence and electroluminescence techniques to the characterization of intermediate band solar cells," *Energy Procedia*, vol. 10, pp. 117–121, 2011.

[151] N. López, L. A. Reichertz, K. M. Yu, K. Campman, and W. Walukiewicz, "Engineering the Electronic Band Structure for Multiband Solar Cells," *Phys. Rev. Lett.*, vol. 106, no. 2, Jan. 2011.

[152] H. Fujii, Y. Wang, K. Watanabe, M. Sugiyama, and Y. Nakano, "Suppressed lattice relaxation during InGaAs/GaAsP MQW growth with InGaAs and GaAs ultra-thin interlayers," *J. Cryst. Growth*, vol. 352, no. 1, pp. 239–244, Aug. 2012.

[153] S. Sauvage, P. Boucaud, F. H. Julien, J.-M. Gérard, and J.-Y. Marzin, "Infrared spectroscopy of intraband transitions in self-organized InAs/GaAs quantum dots," *J. Appl. Phys.*, vol. 82, no. 7, p. 3396, 1997.

[154] T. Kita, T. Maeda, and Y. Harada, "Carrier dynamics of the intermediate state in InAs/GaAs quantum dots coupled in a photonic cavity under two-photon excitation," *Phys. Rev. B*, vol. 86, no. 3, Jul. 2012.

[155] P. Rale, A. Delamarre, G. El-Hajje, R. Tamaki, K. Watanabe, Y. Shoji, Y. Okada, M. Sugiyama, L. Lombez, and J.-F. Guillemoles, "Quantitative optical measurement of chemical potentials in intermediate band solar cells," *J. Photonics Energy*, vol. 5, no. 1, p. 053092, Jun. 2015.

[156] I. N. Stranski and L. Von Krastanow, "Abhandlungen der Mathematisch-Naturwissenschaftlichen Klasse," *Akad. Wiss. Lit. Mainz*, vol. 146, p. 797, 1939.

[157] C. Weisbuch and B. Vinter, *Quantum semiconductor structures: fundamentals and applications*. Boston: Academic Press, 1991.

[158] I. Ramiro, E. Antolin, M. J. Steer, P. G. Linares, E. Hernandez, I. Artacho, E. Lopez, T. Ben, J. M. Ripalda, S. I. Molina, F. Briones, C. R. Stanley, A. Marti, and A. Luque, "InAs/AlGaAs quantum dot intermediate band solar cells with enlarged sub-bandgaps," 2012, pp. 000652–000656.

[159] A. Luque, A. Marti, E. Antolín, P. Linares, I. Tobías, I. Ramiro, and E. Hernandez, "New Hamiltonian for a better understanding of the quantum dot intermediate band solar cells," *Sol. Energy Mater. Sol. Cells*, vol. 95, no. 8, pp. 2095–2101, 2011.

[160] B. Behaghel, R. Tamaki, N. Vandamme, K. Watanabe, C. Dupuis, N. Bardou, H. Sodabanlu, A. Cattoni, Y. Okada, M. Sugiyama, S. Collin, and J.-F. Guillemoles, "Four-fold MQWs absorption enhancement in a 430 nm thick InGaAs/GaAsP MQWs solar cell," 2014, pp. 0099–0101.

[161] A. Takahashi, T. Ueda, Y. Bessho, Y. Harada, T. Kita, E. Taguchi, and H. Yasuda, "One-dimensional miniband formation in closely stacked InAs/GaAs quantum dots," *Phys. Rev. B*, vol. 87, no. 23, Jun. 2013.

[162] M. Henini, Ed., *Handbook of self assembled semiconductor nanostructures for novel devices in photonics and electronics*, 1. ed. Amsterdam: Elsevier, 2008.

[163] H. Z. Song, K. Akahane, S. Lan, H. Z. Xu, Y. Okada, and M. Kawabe, "In-plane photocurrent of self-assembled In x Ga 1 − x A s / G a A s (311) B quantum dot arrays," *Phys. Rev. B*, vol. 64, no. 8, Jul. 2001.

[164] B. Kochman, S. Ghosh, J. Singh, and P. Bhattacharya, "Lateral hopping conductivity and large negative magnetoresistance in InAs/AlGaAs self-organized quantum dots," *J. Phys. Appl. Phys.*, vol. 35, no. 15, pp. L65–L68, Aug. 2002.

[165] J. Inoue, T. Isu, K. Akahane, and M. Tsuchiya, "Saturable absorption of highly stacked InAs quantum dot layer in 1.5 μm band," *Appl. Phys. Lett.*, vol. 89, no. 15, p. 151117, 2006.

[166] E. Alphandéry, R. J. Nicholas, N. J. Mason, S. G. Lyapin, and P. C. Klipstein, "Photoluminescence of self-assembled InSb quantum dots grown on GaSb as a function of excitation power, temperature, and magnetic field," *Phys. Rev. B*, vol. 65, no. 11, Mar. 2002.

[167] Y.-J. Yu, I.-T. Jeong, J.-C. Woo, and W. Jhe, "Near-field spectroscopy of bimodal size distribution of InAs/AlGaAs single quantum dots," *Appl. Phys. Lett.*, vol. 87, no. 14, pp. 143108–143108, 2005.

[168] O. F. Kolomys, V. V. Strelchuk, T. S. Shamirzaev, A. S. Romanyuk, and P. Tronc, "Submicron Raman and photoluminescence topography of InAs/Al(Ga)As quantum dots structures," *Appl. Surf. Sci.*, vol. 260, pp. 47–50, Nov. 2012.

[169] H. . Wang, D. Ning, and S. . Feng, "Temperature dependence of the optical properties of InAs/GaAs self-organized quantum dots with bimodal size distribution," *J. Cryst. Growth*, vol. 209, no. 4, pp. 630–636, Feb. 2000.

[170] E. Rosencher, B. Vinter, B. Levine, and North Atlantic Treaty Organization, Eds., *Intersubband transitions in quantum wells*. New York: Plenum Press, 1992.

[171] A. Mellor, A. Luque, I. Tobías, and A. Martí, "The influence of quantum dot size on the sub-bandgap intraband photocurrent in intermediate band solar cells," *Appl. Phys. Lett.*, vol. 101, no. 13, p. 133909, 2012.